REPORT DOCUMENTATION PAGE

Public reporting burden for this collection of information is estimated to average 1 hour per response, including the time for reviewing instructions, searching existing data sources, gathering and maintaining the data needed, and completing and reviewing the collection of information. Send comments regarding this burden estimate or any other aspect of this collection of information, including suggestions for reducing this burden, to Washington Headquarters Services, Directorate for Information Operations and Reports, 1215 Jefferson Davis Highway, Suite 1204, Arlington, VA 22202-4302, and to the Office of Management and Budget, Paperwork Reduction Project (0704-0188), Washington, DC 20503.

1. AGENCY USE ONLY (Leave blank)	2. REPORT DATE	3. REPORT TYPE AND DATES COVERED
	June 1995	Final, 5/15/91 – 5/15/95

4. TITLE AND SUBTITLE

Interfaces in Inorganic Matrix Composites:
Atomistic Simulation and Experiment

5. FUNDING NUMBERS

AFOSR-91-0285

6. AUTHOR(S)

J. Megusar, S. Yip, J.A. Cornie, B.V. Chambers,
A. Isik, M. Tang, and C.S. Yoon

7. PERFORMING ORGANIZATION NAME(S) AND ADDRESS(ES)

Materials Processing Center
Massachusetts Institute of Technology
Cambridge, MA 02139

AFOSR-TR-95

0663

9. SPONSORING/MONITORING AGENCY NAME(S) AND ADDRESS(ES) NA

Air Force Office of Scientific Research
Directorate of Aerospace and Materials Sciences
110 Duncan Ave, Suite B115
Bolling AFB, DC 20332-0001
AFOSR/NA   Attn: Dr. A. Pechenik 202-767-4987

10. SPONSORING/MONITORING AGENCY REPORT NUMBER

AFOSR-91-0285

11. SUPPLEMENTARY NOTES

12a. DISTRIBUTION/AVAILABILITY STATEMENT

Approved for public release; distribution
is unlimited.

12b. DISTRIBUTION CODE

DTIC QUALITY INSPECTED 8

19951018 014

13. ABSTRACT (Maximum 200 words)

The objective of this research was to contribute to the design or structure and mechanical properties of ceramic and carbon materials, by applying atomistic simulation and experiment.
In the research on carbon, a methodology has been developed to construct amorphous carbon/graphite and graphite/graphite (twin) interfaces by using empirical potential function. Simulation observations have been validated by HRTEM and mechanical testing.
In the research on silicon carbide, the extent to which beta-SiC can be treated by a classical many-body potential function has been established. It has been also shown how stability analysis can be combined with MD simulation to achieve quantitative interpretation of the lattice deformation under an applied load. In the experimental study of interface strength, a method has been developed by using laser induced shock waves. It has been applied to model couples consisting of SiC and saphire, with or without carbon interlayers.

14. SUBJECT TERMS

Interfaces, carbon, silicon carbide,
atomistic simulation, experiment

15. NUMBER OF PAGES

108

16. PRICE CODE

17. SECURITY CLASSIFICATION OF REPORT	18. SECURITY CLASSIFICATION OF THIS PAGE	19. SECURITY CLASSIFICATION OF ABSTRACT	20. LIMITATION OF ABSTRACT
Unclassified	Unclassified	Unclassified	TTT

INTERFACES IN INORGANIC MATRIX COMPOSITES: ATOMISTIC SIMULATION AND EXPERIMENT

J. Megusar, S. Yip, J. A. Cornie

B. V. Chambers, A. Isik, M. Tang, and C. S. Yoon

MATERIALS PROCESSING CENTER

MASSACHUSETTS INSTITUTE OF TECHNOLOGY

CAMBRIDGE, MA 02139

JUNE 1995

FINAL REPORT FOR MAY 1991 - MAY 1995

EXECUTIVE SUMMARY

The objective of this research was to contribute to the atomic scale design of the structure and mechanical properties of ceramic (SiC) and carbon materials. Understanding of the microstructural features that control the deformation and fracture behavior would contribute toward optimization of the respective monolithic and composite materials. To achieve this goal, atomistic simulation, experimental structure and mechanical property characterization, and materials processing are integrated in an interdisciplinary research effort.

In the following, major results are highlighted as they pertain to the research performed on: (i) carbon, (ii) silicon carbide, and (iii) experimental study of interface strength.

1. Research on Carbon

In this research, the possibility and limitations of using atomistic simulation in studying structure and properties of carbon/carbon interfaces have been explored, and its integration with appropriate experimental techniques. This represents the first attempt to study carbon/carbon interfaces by means of atomistic simulation.

Three different empirical potential functions, namely, Tersoff, Brenner, and Takai potential functions have been evaluated for their suitability for the application. After careful evaluation the Brenner potential function has been chosen with appropriate modification for the interplanar interaction in graphite.

Using the selected potential function, the amorphous carbon/graphite interface was constructed by compressing the two phases, which represents a new way of generating such interface. The amorphous carbon structure was prepared in a separate atomistic simulation experiment, by melting and quenching the diamond structure. The simulation experiment indicated that the generated interface mostly consisted of nearly sp^2 hybridized bonding connecting the two sides. To accommodate the bonding, graphitic layers are considerably distorted at the interface. Due to the large interplanar spacing, both the graphite and amorphous carbon sides have a

2

high density of under-coordinated atoms leaving the interface energetically unfavorable with respect to the bulk. The same methodology developed in the present work to construct the amorphous carbon/graphite interface can be readily applied to other carbon/carbon interfaces that may consist of intermediate degree of crystallinity.

In parallel with the simulation effort, experiments were carried out to study the structure and mechanical properties of the amorphous carbon/graphite interface. HRTEM of the interface demonstrated that the basal planes will distort or bend at the interface, which qualitatively agrees with the simulation observation. Furthermore, a method to perform mechanical testing of amorphous carbon/pyrolytic carbon bimaterial was devised. The fracture was shown to occur predominantly through the interface, thus confirming the simulation prediction that the interface is likely to be weak compared to the bulk phases. The mechanical testing also showed that the interface strength is sensitive to surface roughness and chemistry.

An interface comprising of crystalline/crystalline graphite was also considered. In particular, the $\{11\bar{2}1\}$ twin interface in graphite was studied using the analytical model for graphite developed earlier. The atomistic simulation study showed that the $\{11\bar{2}1\}$ twin interface may consist of a special local atomic structure, namely, the 8-4-8 polygons. The boundary composed of such structure has the energy of 0.09 J/m^2 and the activation energy of 3 eV for migration. As in the case of the amorphous carbon/graphite interface, the atomistic simulation method developed to study twin interfaces in graphite can be readily applied to other types of graphite/graphite interfaces.

2. Research on Silicon Carbide

In this part of the project which is focused on β-SiC, our goal is two-fold, first to establish the region of validity of an atomistic description which provides the basis for molecular dynamics simulation, and secondly to investigate the deformation and unstable structural responses under stress through a combination of elastic stability analysis and direct molecular simulations.

A comprehensive study of the thermomechanical properties of β-SiC using a modified

classical many-atom potential model, based on the concept of bond order, has been completed. The calculated equation of state, thermal expansion coefficient, and elastic constants provide a significant database of results characteristic of this particular approach to the description of SiC. Their comparison with experimental data demonstrates that the physical properties of β-SiC near its equilibrium conditions indeed can be reliably determined by atomistic simulations. For conditions at finite stress and elevated temperatures, further validation, using more accurate but computationally more intensive methods which treat the electronic structure explicitly, may be necessary.

Our work on the structural and mechanical behavior of β-SiC under volumetric deformation, both tension and compression, constitutes the first systematic study combining quantitative stability analysis with molecular dynamics simulations. We have shown that under hydrostatic tension β-SiC fails in a brittle manner by crack nucleation, the instability being triggered by the vanishing of the bulk modulus. Under compressive loading the failure mode is more subtle. Here elastic stability criteria showed that the shear modulus vanishes at the critical stress, as a result of large internal strain fluctuations. Simulation then revealed that the lattice has become disordered homogeneously. The fact that binary SiC would amorphize under pressure stands in contrast to the behavior of elemental Si which undergoes structural transition under compression. We are able to show that this difference points to the underlying role of chemical ordering in structural stability of covalent solids, specifically the atomic size disparity in SiC is responsible for its tendency to disorder rather than to undergo a polymorphic transition. This conclusion could not have been so clearly demonstrated without the ability to manipulate the potential function model to suppress either the size effect or the chemical preference for mixed bonds.

We summarize our most significant contributions as follows. First, we have established the extent to which β-SiC can be treated by a classical many-body potential model. Our results, which are the most definitive to date, should provide useful guidance for future investigations in which electronic structure effects are treated explicitly. Secondly, we have shown how stability analysis can be combined

4

with molecular dynamics simulation to achieve quantitative interpretation of the lattice deformation under an applied load. In this process we have also demonstrated the value of potential function manipulation as a means of separating competing effects. We believe that the present results constitute a proper starting point for future work on modelling thermomechanical properties of a class of covalent materials, including SiC and SiC/C systems.

3. Experimental Study of Interface Strength

A method to test the strength of the interface between a coating and a substrate by way of laser induced shock waves has been developed. A laser is pulsed onto a thin absorbing layer on the reverse side of the substrate, creating a shock wave which propagates through the substrate, gets reflected from the front surface where it is converted into a tension wave, and, if of sufficient intensity, causes delamination of the film. Knowledge of the threshold stress pulse intensity at which coating delamination occurs allows determination of the bimaterial interface strength.

This technique has been applied to evaluate model couples in inorganic matrix composites. Test couples consisted of silicon carbide and sapphire, with or without carbon interlayers.

In preparing test couples for the laser spallation experiment, processing of silicon carbide by plasma enhanced CVD has been optimized. Coatings with nearly zero residual stress were deposited at 275 °C, 50 µm pressure and 30 watts applied power with the lower electrode self-biased at +3 volts. Uniform deposition was insured through the use of hydrogen as a dilution gas.

Pyrolytic carbon films were deposited by low pressure CVD to be used as interlayers for interface test couples. The LPCVD apparatus was designed and constructed in the present work to attach to the available PECVD reactor. Coatings were deposited between 1100 and 1400 C at 200 mtorr pressure. It has been determined that the degree of preferred orientation in the coating, average crystallite size, and coating density all increased with deposition temperature while the lattice parameter remained constant.

5

Strength of the silicon carbide/sapphire couples (with and without carbon interlayers) was determined by using laser spallation technique. The tensile strength of the silicon carbide/sapphire interface was found to be 14.7 MPa for LPCVD SiC and 10.0 MPa for PECVD SiC. Carbon interlayers reduced the strength of the interface couple by an order of magnitude, to 0.5 to 2.0 MPa.

Comparison of experimentally determined couple tensile strengths and those prescribed by theory allowed the conclusion that all test couples produced have tensile strengths significantly less than those prescribed by the theory to maximize composite transverse strength while maintaining composite toughening through controlled interface delamination.

The following Ph.D. Theses have resulted from this work:

1. B. V. Chambers, "The Synthesis and Characterization of Model Interface Couples for Inorganic Matrix Composite Applications", Ph.D. Thesis, M. I. T., Dept. Mater. Sci. & Eng., April 1994.

2. A. Isik, "Application of Tight-binding Method in Atomistic Simulation of Covalent Materials", Ph. D. Thesis, M. I. T., Dept. Nucl. Eng., May 1994.

3. M. Tang, "Elastic Instabilities and Structural Responses of Beta-SiC Under Stress,", Ph.D. Thesis, M. I. T., Dept. Nucl. Eng., January 1995.

4. C. S. Yoon, "Interfaces in Carbon Materials: Experiment and Atomistic Simulation", Ph.D. Thesis, M. I. T., Dept. Mater. Sci. & Eng., February 1995.

Table of Contents

8

List of Figures

List of Tables

Chapter 1. Research on Carbon

1.1 Summary

In this research work, we have explored the possibility and the limitations of using atomistic simulation in studying structure and properties of carbon/carbon interfaces and its integration with appropriate experimental techniques. In the process, three different empirical potential functions, namely: Tersoff, Brenner, and Takai potential functions, have been evaluated for their suitability for the application. After careful evaluation we have chosen the Brenner potential function with appropriate modification for the interplanar interaction in graphite.

Using the selected potential function, the amorphous carbon/graphite interface was constructed and its structure and energetics were analyzed. The simulation indicates that the generated interface mostly consists of nearly sp^2 hybridized bonding connecting the two sides. The bonds across the interface when formed are likely to maintain their equilibrium configurations. Due to the large interplanar spacing, both the graphite and a-C sides have a high density of under-coordinated atoms (24%) leaving the interface energetically unfavorable with respect to the bulk. These undercoordinated atoms probably weaken the structural rigidity of the interface providing a fracture path under stress.

In parallel with the simulation effort, experiments were carried out to study the microstructure and mechanical properties of the amorphous carbon/graphite interface. HRTEM study of the a-C/pyrolytic carbon interface suggests that the a-C deposition process induces defects in pyrolytic carbon to enhance bonding between two materials. HTREM of the interface demonstrates that the basal planes will distort or bend at the interface, which qualitatively agrees with the simulation observation. To further validate the simulation result, a method to perform mechanical testing of a-C/pyrolytic carbon bimaterial is devised. SEM and XPS study of the fracture surfaces show that fracture occurs predominantly through the interface, thus, confirming the simulation prediction that the interface is likely to be weak compared to the bulk phases in spite of presence of the reactive edge atoms from

graphite at the interface. The mechanical testing also showed that the interface strength is sensitive to the surface roughness and chemistry and the fracture path can be altered depending on the interface conditions.

In extension to the amorphous carbon/graphite interface research, an interface comprising of crystalline/crystalline graphite was considered. In particular, the $\{11\bar{2}1\}$ twin interface in graphite is studied using the analytical model for graphite developed earlier. The simulation study shows that the $\{11\bar{2}1\}$ twin interface may consist of a special local atomic structure, namely, the 8-4-8 polygons. The boundary composed of such structure has the energy of 0.09 J/m^2 and the activation energy of ~3 eV for migration (mostly due to the formation of a kink along the boundary line). The result suggests that existence of 8-4-8 structure at the twin interface is not improbable compared to the widely accepted dislocation model.

1.2 Evaluation of Interatomic Potential Functions

Success in modelling of condensed-matter system depends upon the predictive capability of method used for simulation; especially, for an empirical interatomic potential function which does not possess general predictive capabilities and heavily depends upon the experimental input used, one needs to perform careful evaluation of such potential function. In this work, a considerable amount of time is devoted in choosing an appropriate potential function for the interface construction.

1.2.1 Comparison of Model Functions: covalent bonds in carbon

Although a number of potential functions are available for carbon, three candidate potential functions are selected because they are computationally efficient and sufficiently rigorous for our application. Of three potential functions considered, the Tersoff and Brenner potential functions are based upon the Abell's bond order expression which incorporates the local atomic environment in a very efficient way. Both functions are fitted to various properties of different carbon polytypes. One noticeable difference is that the Tersoff function's fitting includes bulk modulus of diamond while the Brenner function contains no mechanical properties in the fitting; instead, it was to incorporate the barrier energy to convert the rhombohedral graphite

to graphite to ensure that both diamond and graphite will remain as stable ground structures [1],[2]. Consequence of this difference will be later seen when these functions are evaluated.

The other function is due to Takai et al [3]. The function is based upon the two-body and three-body energy expression. Despite the long-range of the potential function (summation needed up to 8th neighbors for convergence), the merit of the Takai function was that it is able to treat the weak interplanar bonding in graphite.

Listed in Table 1.1 are structural properties calculated for each potential functions. Both Brenner and Tersoff functions reproduce the structural properties with reasonable accuracy while the values for the Takai function are considerably less accurate.

Listed in Table 1.2 are elastic constants at 0 K calculated for diamond and graphite using the stress/strain curve. The stresses are calculated using the Virial stress formula [4]. The Tersoff function gives remarkably accurate elastic constants including C_{44} considering that the only mechanical data used in fitting is the bulk modulus for the diamond crystal. C_{11} for the Takai function appeared to be acceptable for our work, but the function substantially underestimates the shear constant, C_{44}. Meanwhile, the Brenner function fails to reproduce all three elastic constants. Its failure can be attributed to omission of mechanical data about carbon in fitting its parameters as mentioned earlier.

Also listed in Table 1.3 are elastic constants for graphite. Elastic constants calculated with the Tersoff function show considerable deviation from the experimental values. C_{11} for graphite is 14% larger than the experimental value and C_{12} is furthermore negative. In fact, the Tersoff function predicts the shear constant, C_{66} to be nearly twice as high as the experimental value. It appears that the Tersoff potential does not treat angular forces for the trigonal bonds as accurately as it does for the tetrahedral bonds. The Takai potential reproduces reasonable C_{11} value for graphite; however, the Takai function's treatment of the angular forces in graphite is questionable. In addition, its long range undermines the Takai function's usefulness for simulating a large system. The Brenner function's values again show large deviation in mechanical

properties.

After further comparison of the potential functions including calculation of universal binding relations and structure and energetics of carbon clusters [5], the Brenner function is chosen to study the in-plane bonding in graphite. Although the Brenner potential function is unable to produce reasonable mechanical properties of both diamond and graphite, the Brenner function gives a better description of different types of carbon compared to the Tersoff function. The use of the Brenner function ensures that the potential function is quite transferable to different carbon polytypes provided that its application is limited to the structure and energetics of carbon.

1.2.2 Interplanar Bonding in Graphite

Modelling carbon poses a difficult problem due to its ability to form different types of covalent bonds. The problem is further complicated in graphite which exhibits great anisotropy in properties stemming from the strong covalent in-plane bonds and the weak interplanar bonding. Although the interplanar bonding is weak, it plays a crucial role by holding the graphitic sheets intact in correct stacking sequence. It is essential in this simulation to include the interplanar interaction because the planes will either collapse on top of each other or drift apart at a finite temperature without the interplanar bonding.

The Brenner and Tersoff function are unable to consider the interplanar interaction in graphite due to their short range (2.1 Å for Teroff and 2.3 Å for Brenner). In spite of its long range, the Takai function also fails to stabilize the graphite structure. When the graphite crystal is heated to 10 K using the Takai function, the individual graphitic planes will shear apart from one other and drift. The reason for the observed excessive shearing is not clear, but it appears to be a result of lack of interplanar shear- resistance in the graphite lattice as evidenced by the negative C_{44} for graphite given by this potential function in Table 3.

To incorporate the weak interplanar bonding, the Brenner function is combined with the pair potential developed by Oh and Johnson [6]. Elastic constants given by the combined potential function are listed in Table 1.3. Shown in Fig.1.1 is the simulation

result of the graphite crystal at 300 K, which attest to the combined potential function's ability to stabilize the graphite structure at a finite temperature.

1.3 Amorphous Carbon/Graphite Interface

1.3.1 Simulation

Initially, to simulate the amorphous carbon (a-C)/ diamond interface, the diamond crystal is melted by heating the crystal above 6000 K and then the melt at 8000 K is placed adjacent to (100) face of the diamond crystal. Since the melt is lager in volume, in order to apply the PBC, the crystal cell has to be expanded to match the cell size of the melt. Fig. 1.2 shows the snapshots of the particle positions while temperature of the liquid carbon is held at 8000 K with the diamond crystal frozen. As can be seen in Fig. 1.2, a stable liquid front could not be maintained. Because the particles in the melt are highly energetic due to the high melting temperature of diamond with the crystal side stretched to match the simulation cell volume, the particles can quickly penetrate the crystal occupying the interstitial sites. In the subsequent simulation experiment, an attempt was made to minimize the diffusion of particles by immediately freezing the liquid carbon/diamond interface at 8000 K. However, several atoms still penetrate deep into the crystal during quenching and become trapped inside the crystal (see Fig. 1.2).

To obtain better control over the construction of a-C/graphite interface, the construction process was carried out at room temperature. First the Tersoff function is used to generate a cell of amorphous carbon containing 540 particles. A network of amorphous carbon was produced by melting the diamond crystal and rapidly quenching the resulting melt. The graphite crystal containing 768 atoms equally distributed among six graphitic layers is oriented parallel to the <10$\bar{1}$0> direction. Then the amorphous carbon cell and the graphitic crystal are slowly compressed to form a stable interface [7],[8].

Shown in Fig. 3 are the time-averaged atomic positions of the a-C/graphite interface formed after appropriate relaxation.The graphite layer is quite flexible in the x-direction to accommodate the bonding at the interface as seen in (b) of Fig. 1.3, which

leads to distortion of the layers up to ~6 Å deep into the crystal. However, the hexagonal net in the x-y plane is well maintained except for the atoms adjacent to the interface as seen in Fig. 1.3 (c).

Shown in Fig. 1.4 (a) is the potential energy profile across the interface, which shows a flat profile in the graphite side and sudden rise in the potential energy at the interface. The peak is due to presence of the under-coordinated atoms in both graphite and a-C sides as also shown in Fig. 1.4 (b). Because of the large interplanar spacing of 3.5 Å between two planes in graphite compared to the first neighbor distance of 1.4 Å in a-C, the atoms available for bonding in the graphite side are not uniformly distributed on the $(11\bar{2}0)$ surface; they are spatially confined along the edges of the graphene layers, which prevents uniform formation of bonds across the interface and leaves unsatisfied bonds at both sides. In fact we still found that 24% of the atoms in the interfacial region in both a-C and graphite remained unbonded to each other after the relaxation. Consequently, the large mismatch in the structure unique to the graphite results in weak coupling of the a-C with graphite. One would expect such interface to have a high susceptibility to chemical attack and a low strength with respect to the bulk and the fracture is most likely to occur along the interface under stresses normal to the interface because of the comparatively large population of the dangling bonds at the interface.

For close examination of the interface structure, the a-C atoms at the interface bonded to graphite are classified according to their coordination number and binding energy in Table 1.4. Fig. 1.5 shows typical atomic configurations found in Table 1.4. As seen, most of the connected atoms at the interface are 3-coordinated and their binding energies fall within a narrow range. They have nearly planar structure (sum of 3 angles shown is ~360°) with interatomic angle close to 120°. There are less stable 3-coordinated configurations which retain the planar structure but one of the interatomic angles is substantially larger than120°, which leads to the lower binding energy. There are also atoms that are located between the graphitic planes and bridge two graphitic planes. Although small amount of this type of bonding is present at the interface, such bonding will probably take an important part in determining the mechanical response of the interface since they mechanically link

21

two layers with strong sp^2 bonding. In addition, several 4-coordinated atoms are present with nearly tetrahedral structure. It appears that in the a-C/graphite interface formed, the equilibrium configuration is closely maintained in contrast to the crystalline/crystalline interface where often new structure is found so as to accommodate the mismatch in structure.

1.3.2 Experiment

In parallel with the atomistic modelling of the amorphous carbon/graphite interface, attempts are made to experimentally validate the observations made in the simulated interface. In the process, a method is devised to directly estimate the debonding strength of the amorphous/crystalline interface of carbon. In addition, HRTEM is carried out to study the microstructure of such interface.

1.3.2.1 Bimaterial Synthesis

For the HRTEM and the mechanical testing of the interface, a bimaterial consisting of amorphous and crystalline carbon is prepared by rf-sputtering a film of amorphous carbon on the turbostratic carbon/HOPG substrates. The sputtering is carried out in a vacuum with base pressure of 9 x 10^{-7} Torr. A 6-in-diameter turbostratic carbon target is sputtered at 300 W at an Ar pressure of 5 mm Hg. The voltage between the target and the substrate is maintained at 2.4 kV. The sputtering process is used to obtain up to 1.5 μm thick film of fully amorphous carbon.

1.3.2.2 Mechanical Testing

Fig. 1.6 describes preparation procedure for the test specimen. First the pyrolytic carbon substrates are cut and are embedded in LR white epoxy (hard grade). Then the embedded pyrolytic carbon substrates are machined down to ~3 mm in diameter rod. The pyrolytic specimen is metallographically polished after which the specimen is cleaned ultrasonically in distilled water. When needed, the surface structure of polished pyrolytic carbon is altered by oxygen plasma etching before the amorphous carbon deposition. Oxygen plasma preferentially etches the surface of pyrolytic carbon to alter the surface roughness. Two identically prepared specimens are joined

using Epoxy-Patch™. Once the epoxy is fully cured, excessive epoxy is removed and the couple is tested with Instron mechanical testing machine.

The mechanical testing was done for three specimen conditions consisting of different pyrolytic carbon orientation and surface modification conditions. Specimen conditions and corresponding Interface Debonding Strength (IDS) are listed in Table 1.5.

For the case where the interface is oriented parallel to the basal plane (condition 3 in Table 1.5), fracture occurs through the pyrolytic carbon rupturing the weak bonds between basal planes. The interplanar strength of 2.58 MPa is consistent with the experimentally found value for the corresponding pyrolytic carbon orientation.

When the interface is normal to the basal planes of the pyrolytic carbon, and surface modifications included 15 min. etching in oxygen plasma (condition 1 in Table 1.5), the average IDS is 11.8 MPa. It appears that fracture occurred along the interface (with a possible deflection of crack into the a-C) as the measured IDS is significantly lower than the tensile strength of the of the pyrolytic carbon in this orientation[*].

Finally, when the polished surface was not ultrasonically cleaned and not plasma etched after fine-polishing (condition 2 in Table 1.5), IDS drops markedly. It appears that complex chemical group is left behind from the polishing compound, Mastermet™ which alters the chemical characteristics of surface and leads to the sharp decrease in IDS. The effects of surface chemistry on interface strength in addition to surface topology, have been also demonstrated for graphite fibers [10].

Figs. 1.7 (a) and (b) show fracture surfaces of the carbon bimaterial corresponding to the surface preparation condition 1 in Table 1.5. Fig. 1.8 shows the Scanning Tunneling Microscope (STM) image of polished and etched (15 min.) surface of pyrolytic carbon prior to the a-C deposition. It can be observed by comparing Fig. 1.7 with the STM image of the polished and etched surface in Fig. 1.8 that the fracture surface is much rougher than the corresponding surface of pyrolytic carbon. This suggests that the fracture did not occur entirely through interfacial debonding, but in many places the fracture path may have been re-directed through the a-C coating due

---

*. The tensile strength of CVD pyrolytic carbon can range from 100 MPa to 500 MPa depending on the deposition conditions [9].

to the increased interface strength and existence of structural inhomogeneity in the a-C coating. The degree of roughness also precluded the use of scanning tunneling microscopy to evaluate the fracture surface topology and, furthermore, to directly image atomic structure of the respective fracture surfaces.

X-ray photoelectron spectroscopy (XPS) is used to provide further information on the nature of the fracture process as observed in Fig. 1.7. Physical Electronics Model 5100 is used for XPS measurement with MgKα X-ray source in a vacuum of ~10^{-8} torr. The reference peak is the C1s peak of carbon assumed to be at 284.6 eV. All specimens are in-situ cleaned by sputtering the surface at low energy for 1 minute. Polished pyrolytic carbon and a-C film deposited on Si wafer are included for comparison. Table 1.6 lists the peak positions and full-width-at-half-maximum (FWHM) of the examined specimens. The XPS data suggest that over the area of XPS measurement (typically 1 mm^2) structure of the fracture surface 1 resembles that of a-C, while structure of the matching fracture surface 2 consists predominantly of pyrolytic carbon.

1.3.2.3 HRTEM

A EM-002B from TOPCON at 200 kV is used for the high-resolution transmission microscopy. A cross-sectional specimen is made such that (002) lattice fringes at the interface can be imaged.

Figs. 1.9 (a) and (b) are the low magnification bright field images of the a-C/pyrolytic carbon interface. In Fig. 1.9 (a), the basal planes are oriented normal to the interface whereas Fig. 1.9 (b) is the case where the basal planes are parallel to the interface. When the interface is oriented parallel to the basal planes, the fracture during tensile testing occurs in the bulk pyrolytic carbon rather than along the a-C/graphite interface. This has been discussed in the previous section. The same fracture process can be also observed on a microscopic level in Fig. 1.9 (b). These observations imply that the interfacial bonding between a-C and pyrolytic carbon is stronger than the interplanar strength of pyrolytic carbon.

Carbon atoms arriving at the surface of the substrates during a-C deposition appear

to be energetic enough to cause extensive damage to the top layers of pyrolytic carbon. As can be seen in Fig. 1.10, the planar graphite structure characteristic of HOPG becomes disordered near the interface as a result of a-C deposition. As a result of the deposition process, the reduced graphite crystallites size and increased misorientation between graphite crystallites impart higher interface strength to pyrolytic carbon.

When the basal planes are oriented normal to the interface, the interface appears to be morphologically rough both at the low and high magnifications. The roughness seen at the low magnification in Fig. 1.9 (a) is probably induced by cutting and polishing the pyrolytic carbon substrate. Strong in-plane, σ bonds and much weaker π bonds between basal planes make the material very difficult to be polished flat in the edge orientation, but the specimen preparation process alone could not have caused the rough features at an atomic scale seen in Fig. 1.11. Raman spectroscopic study of the graphite edge planes after fine-polishing showed that polishing does not lead to extensive disorder in the graphite edge planes [11]. The distortion of the basal planes at the a-C/graphite interface appears to be an intrinsic feature of any graphitic interface as demonstrated by the atomistic simulation.

1.3.3 Comparison of Experiment and Simulation

In comparing the simulated a-C/graphite interface with the microstructures obtained from HRTEM, there is much similarity between them, but also there exists noticeable differences between the MD result and the real interface. Distortion of the basal planes near the interface observed in HRTEM micrograph is very much similar to the bending of the graphitic planes near the interface observed in the MD simulation (see Fig. 1.2). In HRTEM micrographs of the interface, (002) lattice fringes close to the interface are disconnected and bent compared to the fringes away from the interface. Carbon atoms bombarding the substrate are energetic enough to penetrate and open-up the basal planes. This allows maximum possible formation of bonds with the incoming atoms even though the substrate is cooled during sputtering. Therefore, the HRTEM observation of the interface is consistent with the simulated result in that it is the graphite crystal that conforms to the a-C by bending its layers while retaining

individual hexagonal sheets more or less intact.

On the other hand, there is much difference between the HRTEM micrograph of the interface and the snapshot of the simulated a-C/graphite interface. The actual interface penetrates much deeper into the graphite and it has much rougher morphology. We believe that the discrepancy is due to the relatively low temperature which is dictated by the simulation model and to the small system size. If the interface were allowed to heat up in the simulation, the rise in kinetic energy would lead to a more pronounced bending and distortion of graphitic planes in the x-direction and, at the same time, to increased interface roughness. This could be reproduced in simulation if a larger system is used without applying the PBC which exerts the external pressure on the system.

From the analysis of the simulated interface, it has been proposed that the a-C/graphite interface is energetically unfavorable due to existence of many under-coordinated atoms at the interface. The MD study also shows that if the interface is allowed to form at an elevated temperature, the number of under-coordinated atoms should decrease and one can obtain much more stable interface. The mechanical testing of the a-C/pyrolytic carbon interface confirms that the interface formed at a low temperature is relatively weak compared to the bulk.

The mechanical testing also points out that the interface strength is very much affected by the surface roughness and surface chemistry, which was not addressed by the simulation effort. Here, we see a new possibility for future MD simulation effort. With availability of potential functions that can treat interaction between carbon atoms with different types of atoms [12]~[14], one has the potential to probe effects of the surface chemistry on the interface strength. Furthermore, a large scale simulation by using parallel computing could be done to also address the surface roughness issue.

1.4 Twin Interface

Although numerous evidences of existing twins have been observed in both artificial and natural graphite, the most frequent in occurrence is the one whose habit plane in the matrix is {11$\bar{2}$1}. For the structure of such {11$\bar{2}$1} twin interface, two different models have been proposed. The dislocation model, which is generally accepted as the correct model, consists of partial dislocations of the type: 1/3 a[0110] and 1/3 a[1010] lying on every alternate basal plane along the twin interface [15]. The second model proposed by Platt is based upon special local atomic structure so-called '8-4-8' along the twin interface [16]. Atomistic simulation is carried out to study the possible existence of 8-4-8 structure at the graphite twin interface using the empirical potential function for graphite developed earlier.

1.4.1 Structure of the 8-4-8 twin boundary

The simulation cell contains 560 particles equally divided among eight basal planes. Periodic boundary conditions are applied in both y-and z- directions. Along the x-direction, the crystal has free surfaces to allow free movement in that direction. Following a similar procedure from the earlier atomistic simulation study of the twin boundaries in the h.c.p. metals, two different initial atomic configurations are used (R- and D- configurations) [17],[18]. The initial atomic configurations are relaxed through the steepest descent quench method [19] to their respective minimum energy configuration. The proposed 8-4-8 structure was found to be most energetically favorable configuration in the twin-matrix interface.

Shown in Fig. 1.12 is the atomic arrangement of the 8-4-8 structure at the interface. Every other basal plane contains the 8-4-8 structure at the interface while the rest of the graphitic planes are just continuous hexagonal net with appropriate angular distortion at the interface. In the relaxed 8-4-8 structure, distortion of the lattice due to the twin boundary is localized; in fact, it is limited to the first two rows of atoms on either side of the twin plane. Atoms outside the interfacial region will retain their equilibrium structures. Even the atoms in the interfacial region closely retain their original trigonal configuration except the ones participating in the four-membered

square ring shown in Fig. 1.12. The atoms in the four-membered ring have one of its bond angle close to 90°; thus, they have a higher potential energy of -6.59 eV/particle due to the consequent angular distortion.

Due to the relatively small amount of overall distortion in the twin interface, the whole boundary has the excess energy of only 0.09 J/m^2 compared to the perfect graphite structure. However, this twin boundary energy is somewhat underestimated. By having free surfaces in the x-direction, we have ignored the lateral strain energy arising from the accompanying volume change as evidenced by increase of bond lengths across the interface from initial 1.18 Å to 1.56 Å after relaxation. The interface energy is substantially lower than the value conjectured by Platt [16]. The discrepancy is likely to be from Platt's lack of consideration for further energy reduction due to cooperative motion of atoms during relaxation and our omission of the volume change effect in the energy calculation.

1.4.2 Motion of Twin Boundary

So far, the 8-4-8 appears to be stable as the strain energy involved is reasonably low, but the {11$\bar{2}$1} twin boundary in graphite must have a small activation energy for displacement, which is experimentally observed to occur easily under slight pressure [15]. Using the analytical potential model, an attempt was made to predict the activation energy of the 8-4-8 structure and to observe its propagation though the matrix in order to ensure validity of the 8-4-8 structure.

Like any other dislocation, the motion of 8-4-8 boundary will probably not involve a jump of the whole twin plane, but an initial step or kink in the twin boundary, which assists jumps of the subsequent section in the boundary. To simulate such motion and calculate the barrier energy for the migration, a kink is inserted in the 8-4-8 boundary as shown in Fig. 1.13. The simulation cell consists of a single graphite sheet (216 particles), containing the kink. Excess energy is calculated as one of atoms adjacent to the kink (labeled as 1 in Fig. 1.13) is displaced in the y-direction. Continuation of such motion will effectively move the twin boundary by one atomic step in the x-direction. The calculated energy is plotted in Fig. 1.14. The plot indicates that the energy drops continuously except the small barrier in the initial stage of

displacement. The energy drop is achieved as atoms around the atom 1 attain more favorable angular configuration during displacement of the atom 1. The initial barrier observed in the curve is caused by breaking of the bond with its neighbor labeled 2 in Fig. 13. Obviously, if the atom 2 is also allowed to move in the opposite direction to that of atom 1, the energy of the system can be further lowered. The plot of the energy for such simultaneous displacements is also shown in Fig 14. When both atom 1 and atom 2 are appropriately displaced so as to propagate the 8-4-8 twin boundary, the energy is always lower than that of the initial structure with the kink. This suggests that once a kink is present along the interface, the migration should be spontaneous; therefore, the activation energy for the migration is solely due to nucleation of a step in the boundary.

The energy required to nucleate such a kink was computed to be ~3 eV. It is largely due to the displacement required in the z-direction, which leads to puckering of the graphitic plane at the kink. The calculated nucleation energy is comparable to the formation energy of a vacancy in graphite, which is 5 eV for the Brenner potential function used in this calculation (7.6 eV from ab initio calculation [20]). Hence, existence of such step on the twin boundary is not highly improbable. In addition, the fact that the energy is required mostly to displace the atom in the z-direction in creating the kink agrees well with the experimental observation since the twins in graphite are easily produced by a compressive stress on the basal plane [15].

1.4.3 Discussion

We have considered the $\{11\bar{2}1\}$ twin interface using the Brenner's analytical model of graphite. The simulation study indicates that the 8-4-8 structure first proposed by Platt is a viable mechanism by which the given twin can be created and displaced through the graphite crystal although the dislocation theory for the twin/matrix is very plausible. It may be possible that such twin interface is composed of either the 8-4-8 polygons or a pair of alternating partial dislocations depending on the condition of the matrix such as orientation and magnitude of the applied stress and density of the existing dislocations. Therefore, efforts for experimental confirmation of existence of the 8-4-8 structure is highly desirable.

1.5 Conclusion and Recommendation

Although there has been extensive amount of research carried out on the bulk properties of carbon materials, this thesis work represents the first attempt to study carbon/carbon interfaces by means of atomistic simulation. In the process, the Brenner's empirical function was modified to treat both in-plane and out-of-plane bonding in graphite. In addition, amorphous/crystalline interface was created by compressing the two phases, which represents a new way of generating such interface.

This work is unique in that atomistic simulation using empirical potential function is integrated with appropriate experiment. The experiment is designed to validate key aspects of the simulation. It has been demonstrated here that such integrated approach can be a powerful tool by providing insights to adhesion of a-C to the graphite crystal. It was concluded from this integrated approach that the unique structure of graphite renders the a-C/graphite interface energetically unfavorable and leads to deformation of the graphitic layers in the interfacial region to accommodate the distortion necessary to have a maximum number of bonds across the interface.

The modified Brenner's graphite model is also utilized to probe the $\{11\bar{2}1\}$ twin structure in graphite. It has been shown that the twin interface composed of a special atomic geometry ('8-4-8' polygons) can be stable and easily mobile, which confirms the model previously proposed by Platt.

The approach here was developed for amorphous/crystalline and crystalline/ crystalline interfaces which represent structurally extreme ends of carbon materials. However, the same methodology can be readily applied to other carbon/carbon interfaces that may consist of intermediate degree of crystallinity.

As an extension of this work, more reliable potential function and parallel computing to allow a large scale simulation are sought to study effects of surface roughness and chemistry on the mechanical properties of interfaces through atomistic simulation. To facilitate such effort, it is desirable to develop a hybrid system which enables the use

of more rigorous approach such as tight-binding method for the critical portion of simulation cell and an empirical potential function for rest of the cell.

Furthermore, using scanning tunneling microscope an experimental confirmation of existence of 8-4-8 structure at the twin boundary is highly desirable.

1.6 List of Papers Published/Submitted

o *Molecular dynamic simulation of amorphous carbon and graphite interface,* C. S.Yoon and J. Megusar, Interface Science (1995) in press.

o *Simulation of twin interface in graphite*, C. S.Yoon and J. Megusar, submitted to Carbon.

o *High resolution microscopy and compression testing of carbonized and graphitized foams*, J. Megusar and C. S. Yoon, in preparation.

1.7 References

1. J. Tersoff, Phys. Rev. Lett. **61**, 2879 (1988).

2. D. W. Brenner, Mater. Res. Soc. Symp. Proc. Vol. **141**, 59 (1989).

3. T. Takai, C. Lee, T. Halicioglu and W. A. Tiller, J. Phys. Chem. **94**, 4480 (1990).

4. K. S. Cheung and S. Yip, J. Appl. Phys. **70** (10), 5688 (1991).

5. T. Halicioglu, Chem. Phys. Lett. **179**, 159 (1991).

6. D. J. Oh and R. A. Johnson, Mater. Res. Soc. Symp. Proc. Vol. **141**, 51 (1989).

7. C. S. Yoon and J. megusar, to be published in Interface Science (1995).

8. C. S. Yoon, Ph. D. Thesis at Massachusetts Institute of Technology, Department of Materials Science and Engineering (1995).

9. J. C. Bokros, in *Chemistry and Physics of Carbon*, Vol. 5, edited by P. W. Walker Jr. (Marcel Dekker, Inc., New York 1969), p. 81.

10. K. Wolf, R. E. Fornes, J. D. Memory, and R. D. Gilbert, in *Chemistry and Physics of Carbon*, Vol. 18, edited by P. A. Thrower (Marcel Dekker, Inc., New York 1982), p. 104.

11. G. Katagiri, H. Ishida and A. Ishitani, Carbon **26**, 565 (1988).

12. T. Takai, T. Halicioglu and W. A. Tiller, Surf. Sci. **164**, 327 (1985).

13. Th. Frauenheim, P. Blaudeck, U. Stephan, and G. Jungnickel, Phys. Rev. B **48**, 4823 (1993).

14. D. W. Brenner, Phys. Rev. B **42**, 9458 (1990).

15. E. J. Freise and A. Kelly, Proc. Roy. Soc. A **264**, 269 (1961)

16. J. R. Platt, Z. Kristallogr. **109**, 226 (1957).

17. Y. Minonish, S. Ishioka, M. Koiwa and S. Morozumi, Phys. Stat. Sol. (a) **71**, 253 (1982).

18. A. Serra and D. J. Bacon, Phil. Mag. A **54**, 793 (1986).

19. R. L. Burden and J. D. Faire, *Numerical Analysis* (Prindle, Weber & Schmidt, Boston, 1985), p. 511.

20. E. Kaxires and K. C. Pandey, Phys. Rev. Lett. **61**, 2693 (1988).

Appendix: tables and figures

Table 1.1 Calculated structural properties of diamond and graphite at 0K.

		Takai	Tersoff	Brenner	Experimental
Diamond	Cohesive Energy (eV/atom)	-7.126	-7.371	-7.346	-7.349
	Bond Length (Å)	1.566	1.54	1.51	1.54
Graphite[a]	Cohesive Energy (eV/atom)	-7.596	-7.395	-7.377	-7.374
	Bond Length (Å)	1.362	1.46	1.38	1.42

a. The values for graphite is limited to an individual graphite plane for the Tersoff and Brenner function. The experimental value is also given for a single layer.

Table 1.2 Elastic constants for diamond at 0 K.

	Takai	Tersoff	Brenner[I]	Experimental
C_{11} (GPa)	981	1070	145	1080
C_{12} (GPa)	743	102	308	130
C_{44} (GPa)	111	656	11500	580
Bulk Modulus (Mbar)	-	4.26	-	5.45

Table 1.3 Elastic constants for graphite at 0 K.

	Takai	Tersoff	Brenner + Pair potential	Experimental
C_{11} (GPa)	1160	1240	271	1060
C_{12} (GPa)	661	-243	328	180±20
C_{13} (GPa)	15.5	-	2.81	15±5.0
C_{33} (	11.0	-	38.6	36.5±10
C_{44} (GPa)	-0.987	-	2.82	0.18~0.35
Bulk Modulus (Mbar)	-	2.33	-	2.8

Table 1.4 Classification of atoms in a-C side bonded with graphite at the amorphous carbon/graphite interface.

Coord. Number	Atoms bonded with graphite	Number of bonds present at the interface	Average Binding Energy (eV)	Standard Deviation of Binding Energy (eV)
3	1	14	-7.2238	0.0509
		4	-6.8258	0.2479
3	2	3	-7.2213	0.1498
4	1	5	-7.1307	0.0516
2	1	1	-5.9487	-
6	1	1	-7.1912	-
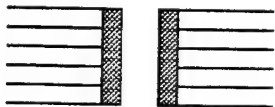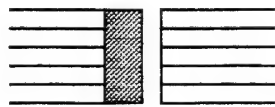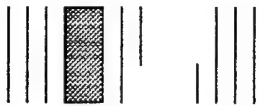
Specimen Conditions	IDS (MPa)
1. Basal plane ⊥ Interface Ultrasonic clean, 15 min. etching 	11.4
	7.92
	18.8
	8.89
	11.8 ± 5.0
2. Basal plane ⊥ Interface No ultrasonic clean, no etching 	2.96
	1.82
	3.12
	2.63 ± 0.70
3. Basal plane // Interface 	2.41
	0.54
	4.81
	2.58 ± 2.1

Table 1.5   Interface debonding strength for a-C/pyrolytic carbon couple.

Table 1.6 Peak positions and FWHM of XPS C1s spectrum

	Position (eV)	FWHM (eV)
Pyrolytic carbon	284.61	1.70
a-C	284.68	1.57
Fractured surface 1 (condition 1)	284.72	1.59
Fractures surface 2 (condition 1)	284.63	1.67
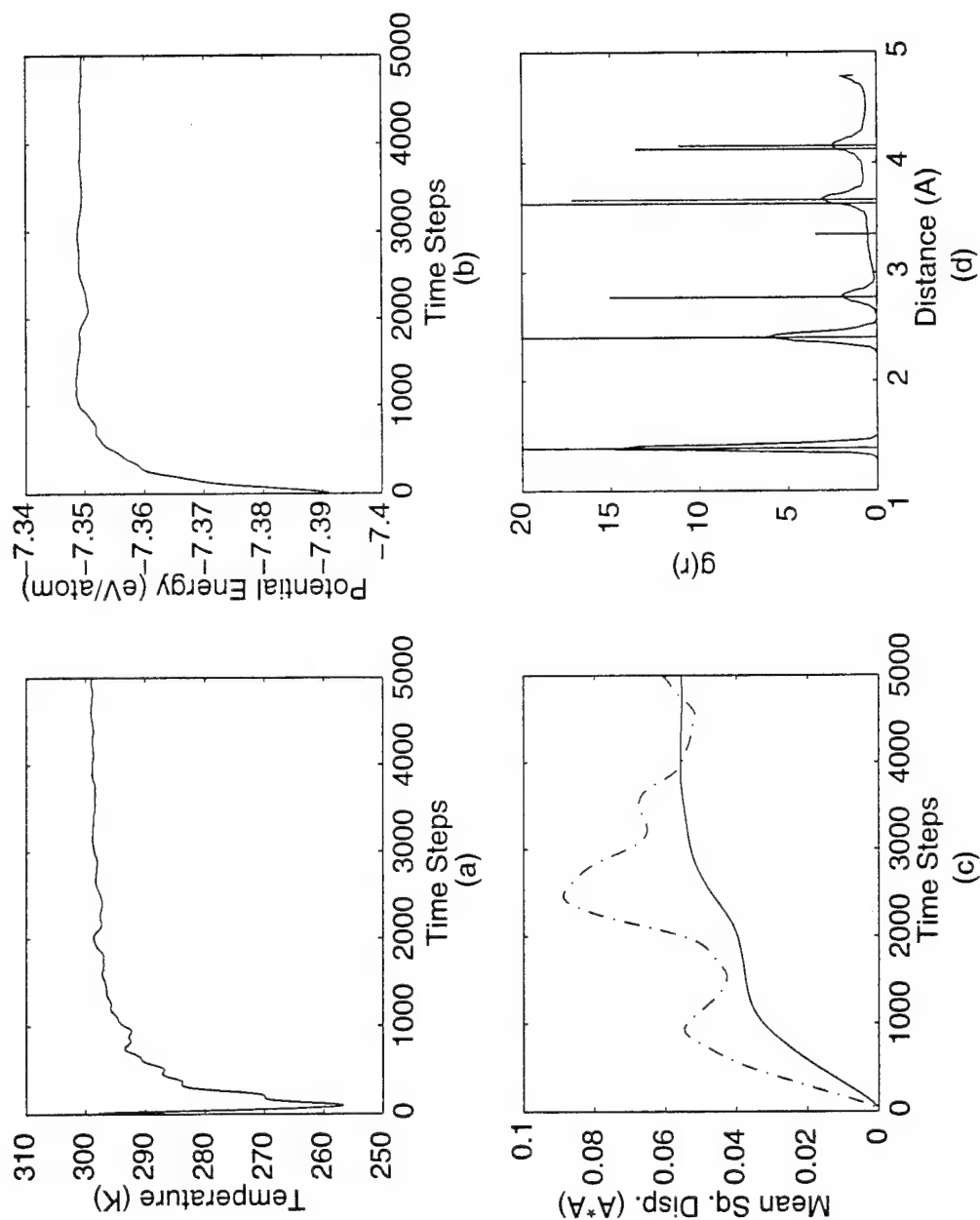
Fig. 1.1 Simulation results for graphite at 300 K using the combined potential (see text). (a) and (b) show the temperature and potential energy of the system respectively during equilibration while (c) plots the mean square displacement (-.- instantaneous, - time-averaged). (d) shows the RDF at 300 K (Straight lines correspond to the peaks at 0 K).

38
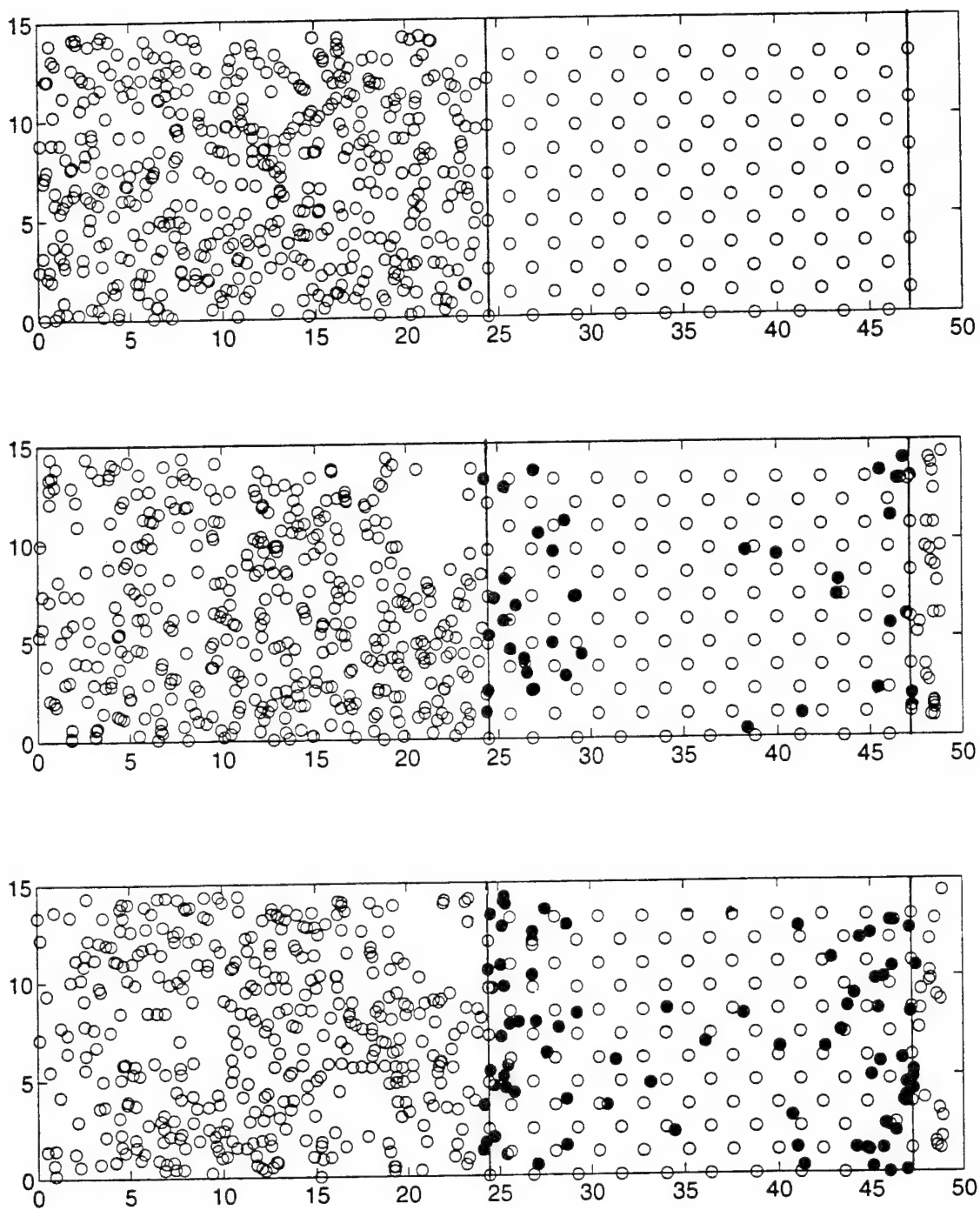
Fig. 1.2 Snapshots of liquid carbon/diamond interface at 8000 K after (a) 2 time steps, (b) 10000 time steps and (c) 20000 time steps. 'Hot' atoms (shaded) from molten carbon diffuse rapidly through the diamond crystal.
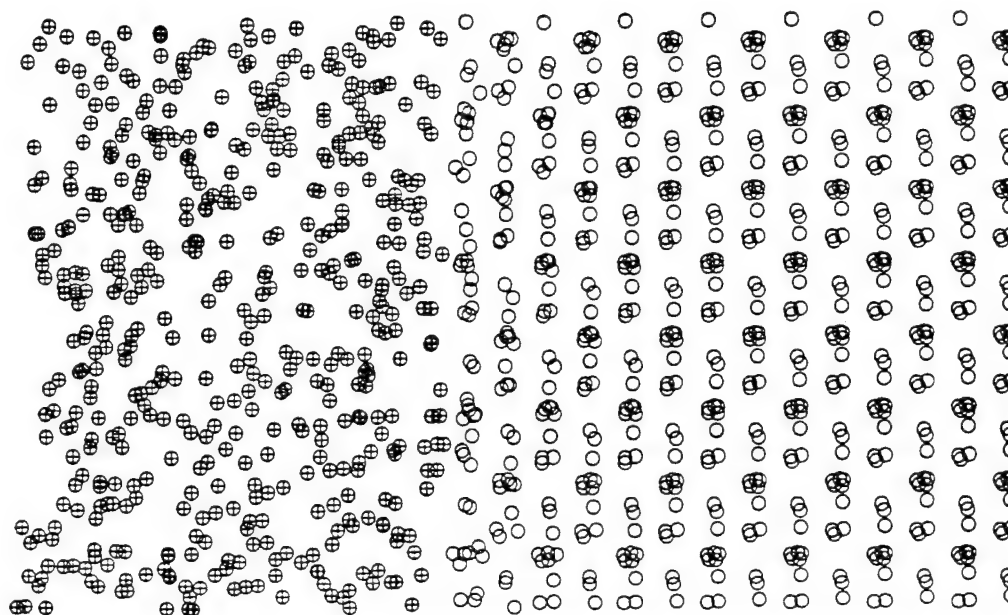
(a)
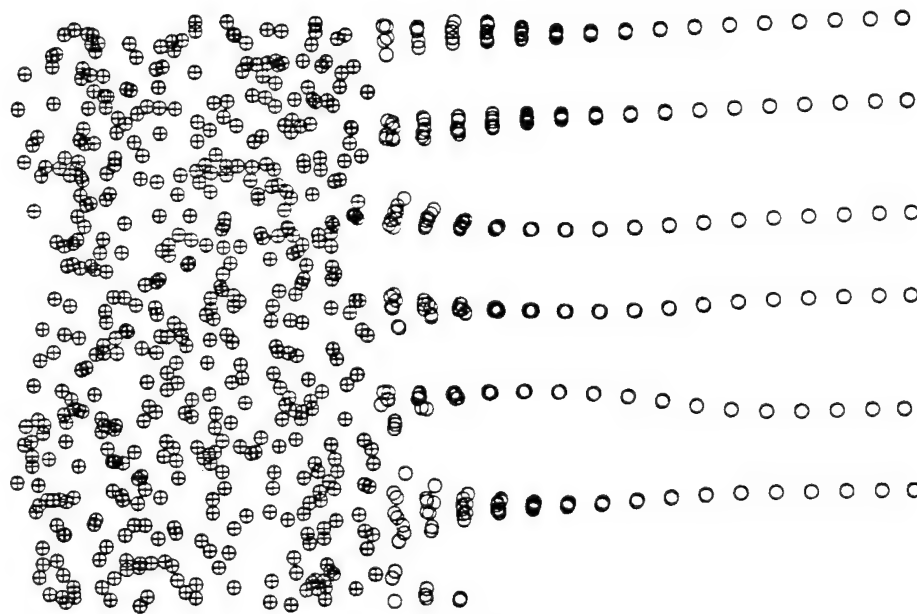
(b)

Fig. 1.3 Time-averaged atomic positions at the a-C/graphite interface. (a) and (b) show X-Y and X-Z projection of the cell, respectively. (c) is the averaged atomic positions for a graphene layer from the graphite cell, showing deformation of the hexagonal net near the interface.

Interface ▶

(c)
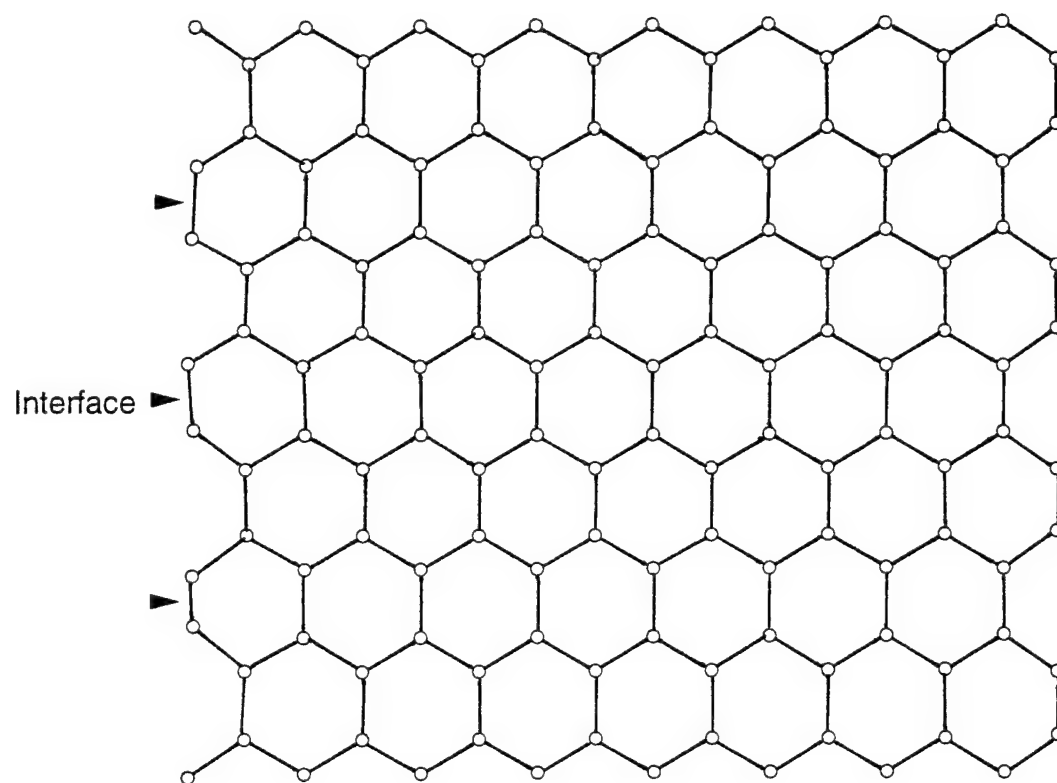
Fig. 1.3
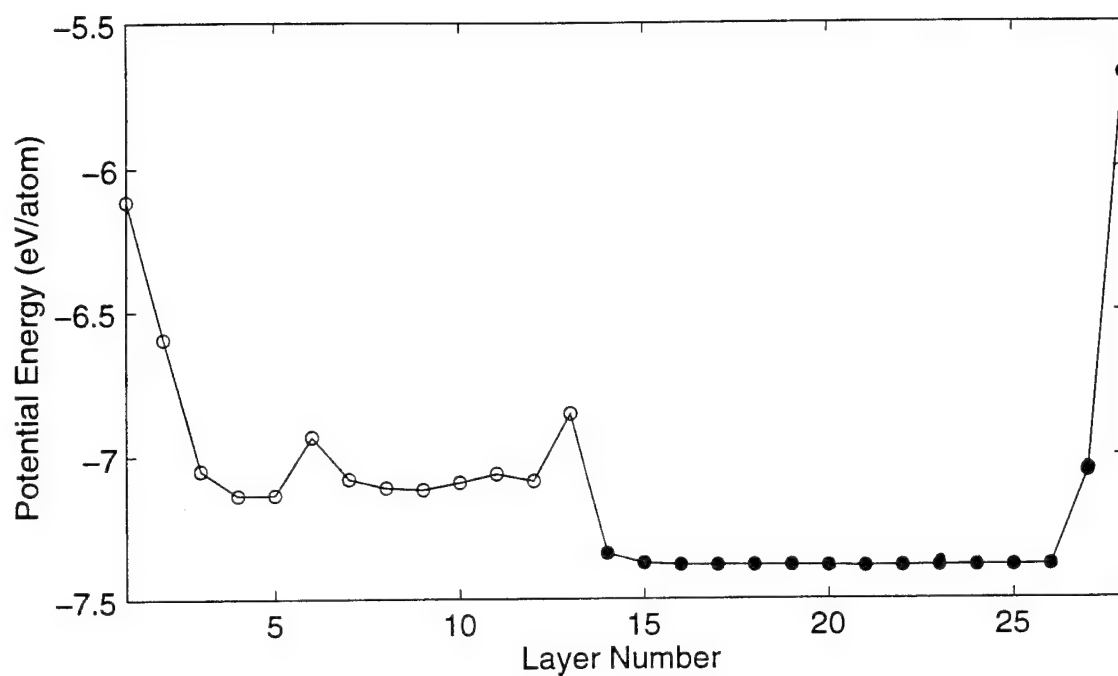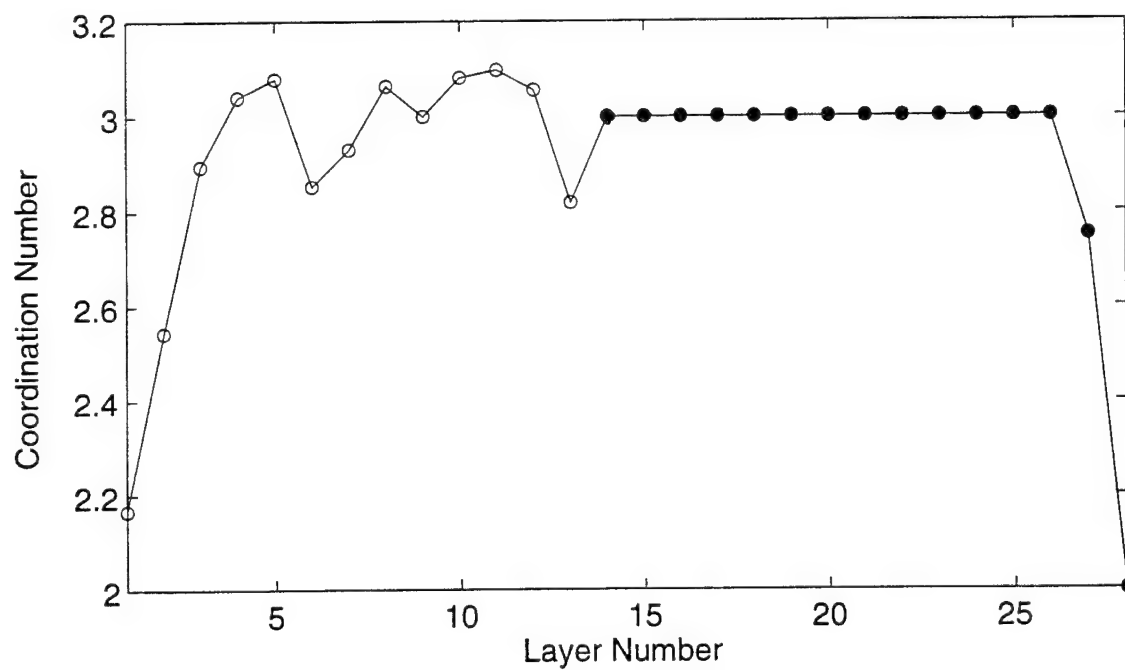
Fig. 1.4 (a) time–averaged potential energy profile and (b) time–averaged coor
number profile across a–C/graphite interface are shown. Shaded atoms represe
graphite side of the simulation cell.

3-coord. High-energy Configuration

sum of angles = 359.90

1.5151 Å   157.81   1.4936 Å

100.01   102.07

1.4303 Å

3-coord. Preferred Configuration

1.4393 Å

118.61

118.94

1.4914 Å

116.31   1.4211 Å

sum of angles = 353.86

3-coord. Configuration Linking Two Layers

sum of angles = 347.66

1.4474 Å

117.58

1.4261 Å   116.73

113.34

1.4378 Å

4-coord. Configuration
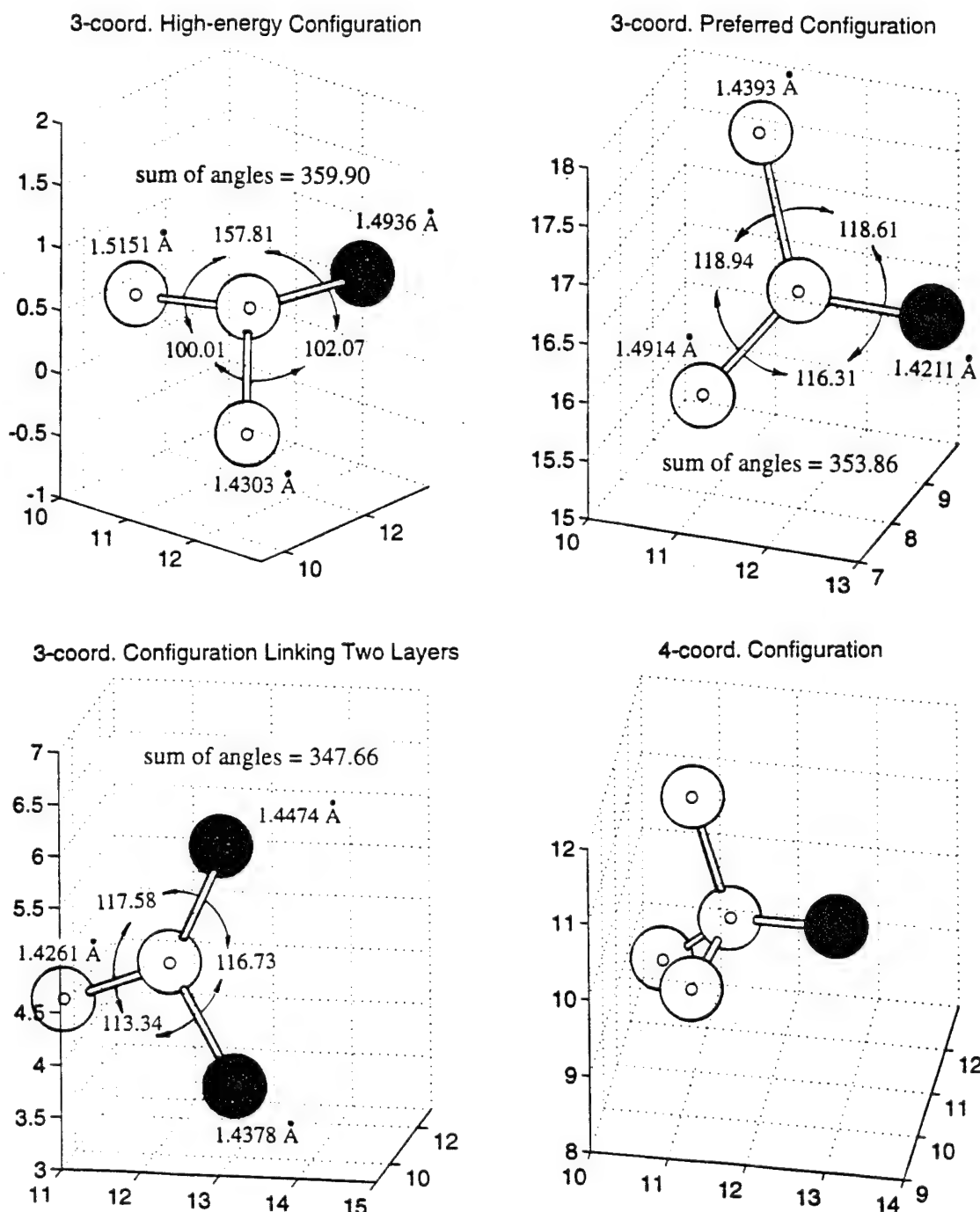
Fig. 1.5 Typical atomic configurations of a-C atoms bonded to graphite found in table 1.4 are drawn. Shaded atoms represent the graphite atoms.

43

1. Pyrolyticbon carbon substrates are embeded in LR white epoxy.

2. Substrates are machined and metallographically polished.

3. ~1.5 μm thick layer of a-C is deposited after in-situ sputter-cleaned.
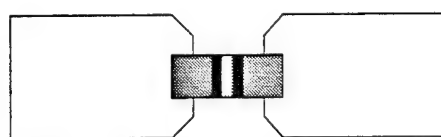
4. Two specimen are glued.
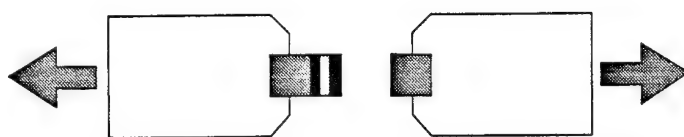
5. The specimen is tested in tensile mode using a self-aligning fixture in an Instron machine.

Fig. 1.6 Schematic drawing for preparing a test specimen for measuring IDS of a-C/ graphite interface.
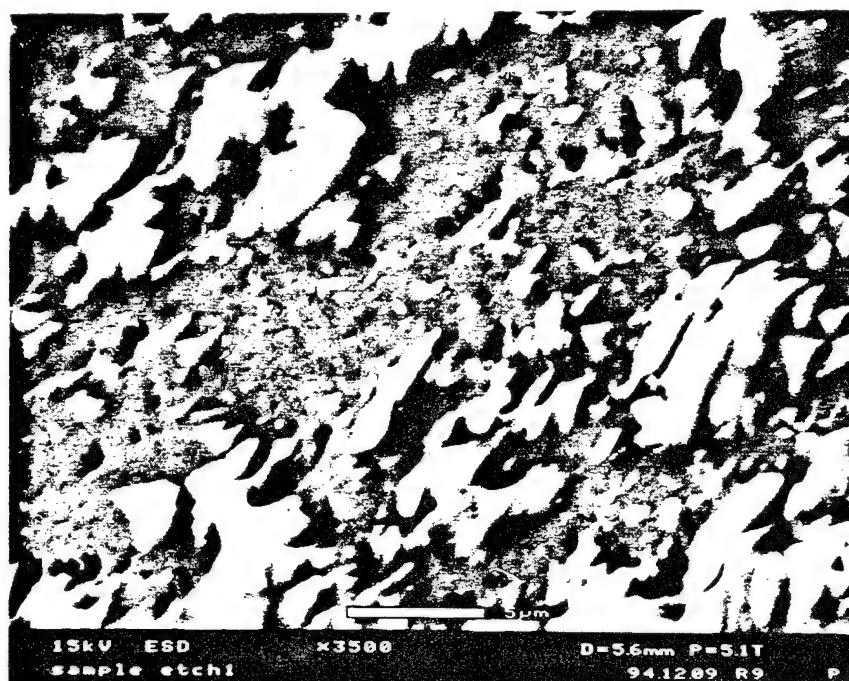
(a)
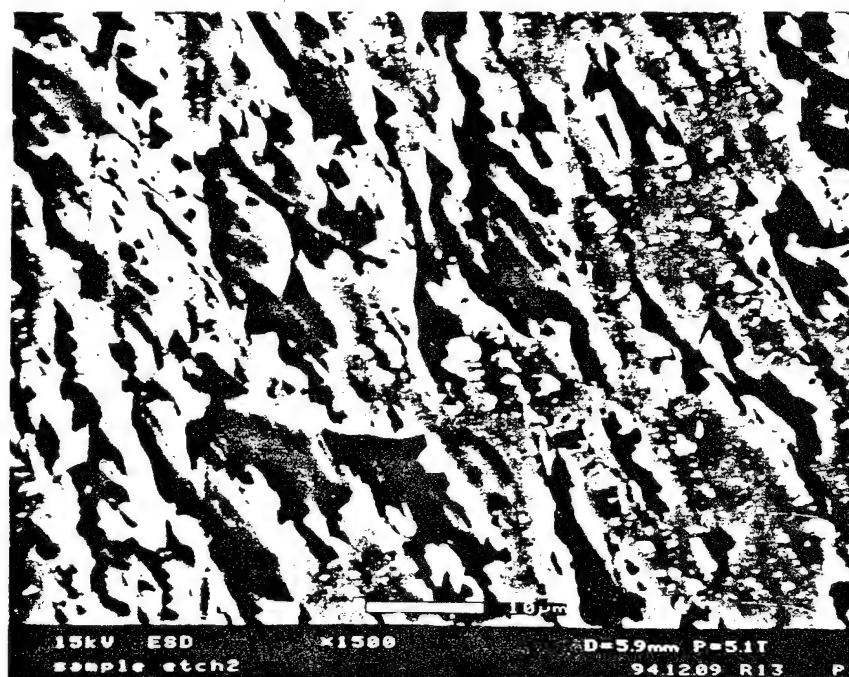
(b)

Fig. 1.7 (a) and (b) are SEM image of fractured a-C/pyrolytic carbon bimaterial with 15 min. etching of pyrolytic carbon substrate prior to deposition.
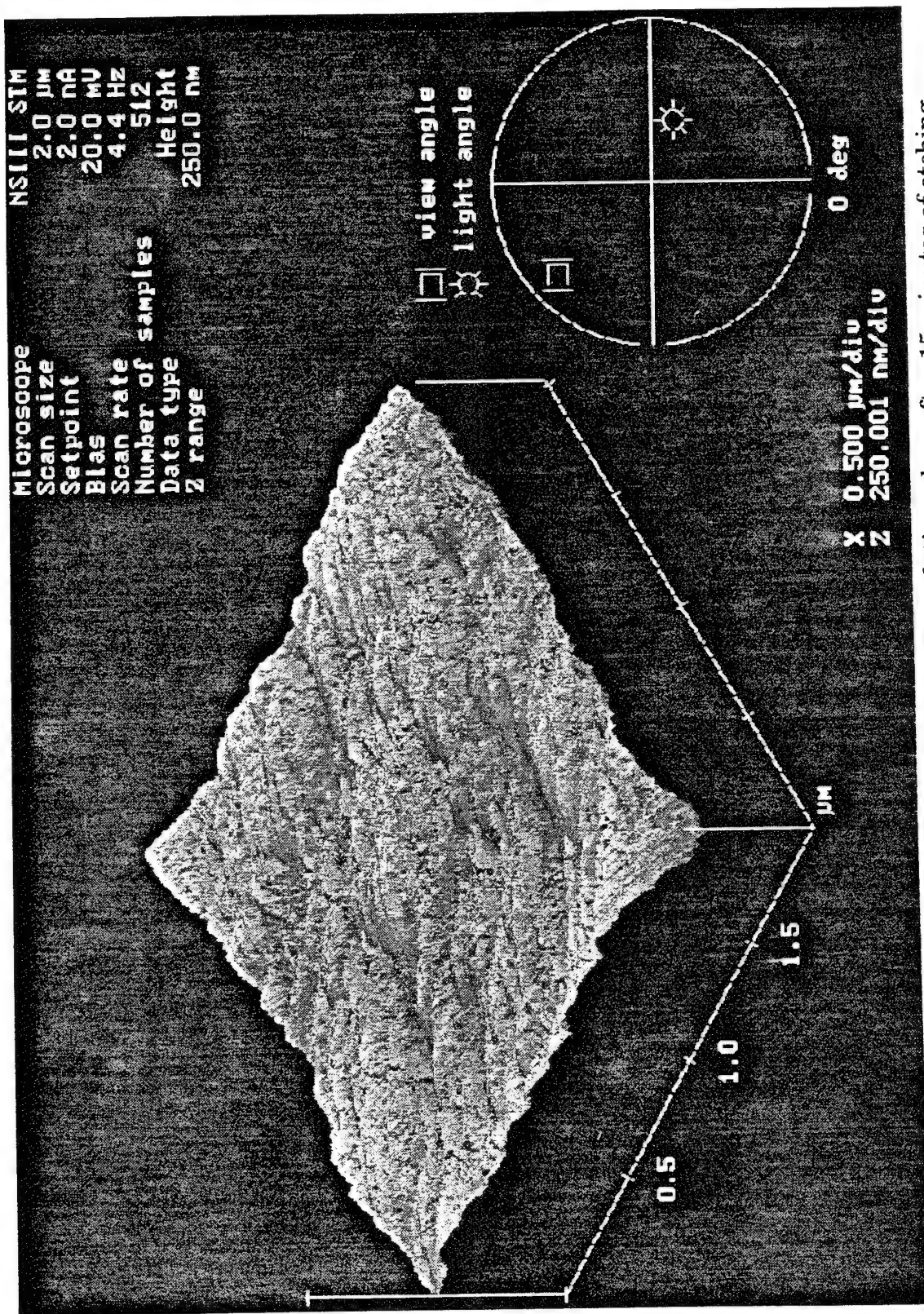
Fig. 1.8 STM image of oxygen plasma-etched surface of pyrolytic carbon after 15 minutes of etching.
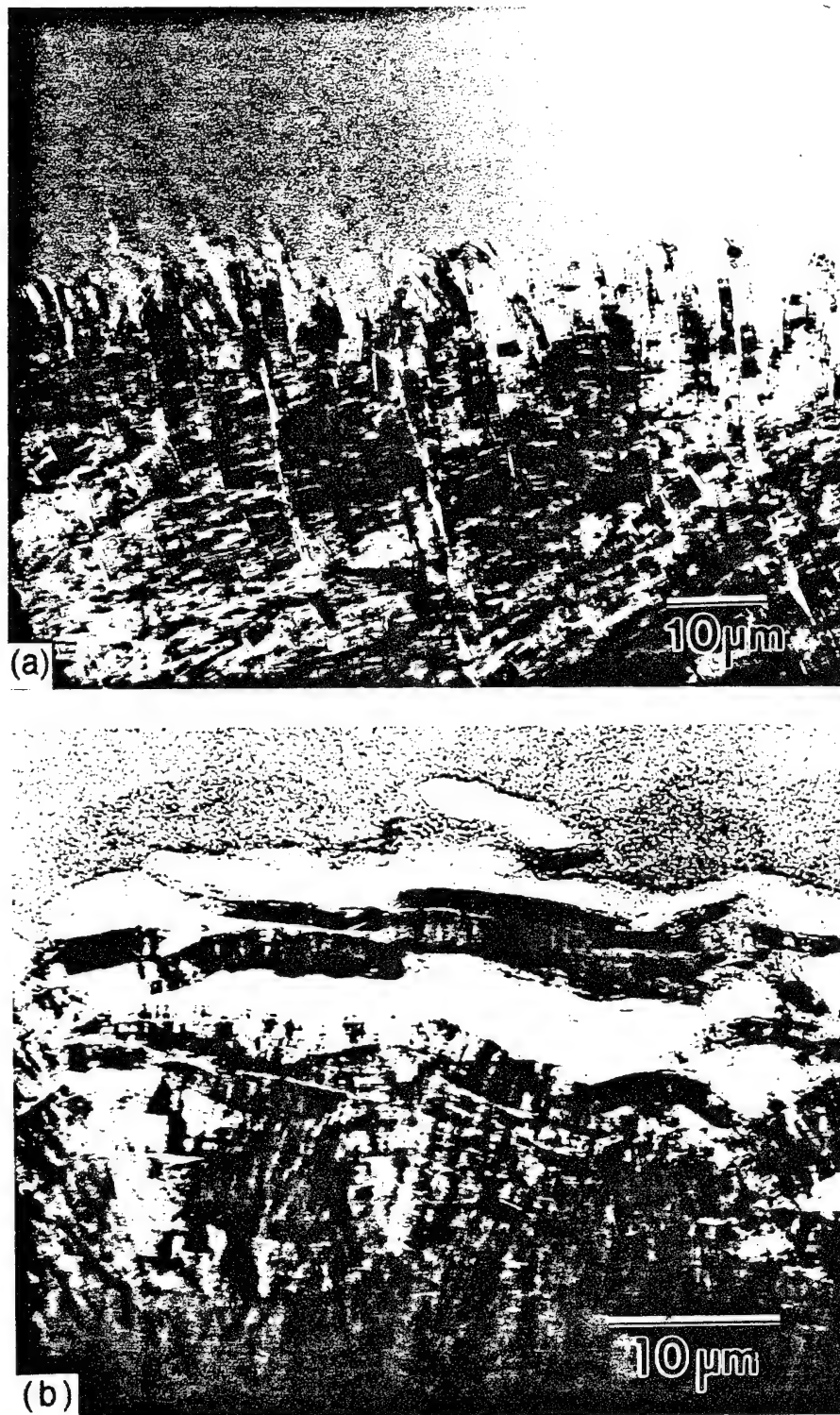
Fig. 1.9 Bright field image of a-C/pyrolytic carbon interface. In (a), basal planes are normal to the interface and in (b), basal planes are parallel to the interface.
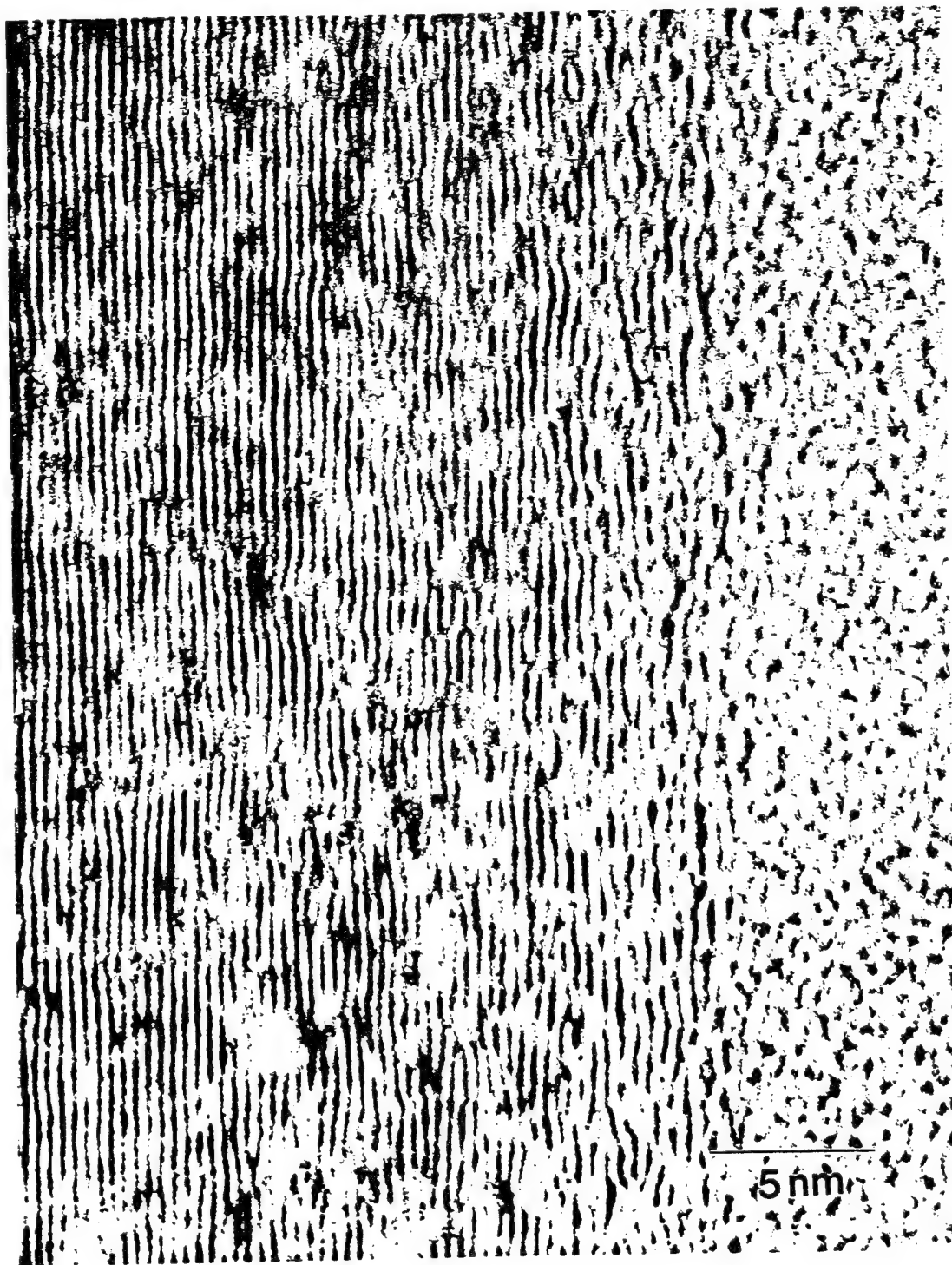
Fig. 1.10 HRTEM image of the a-C/HOPG interface showing damage to the top layers during the deposition process.
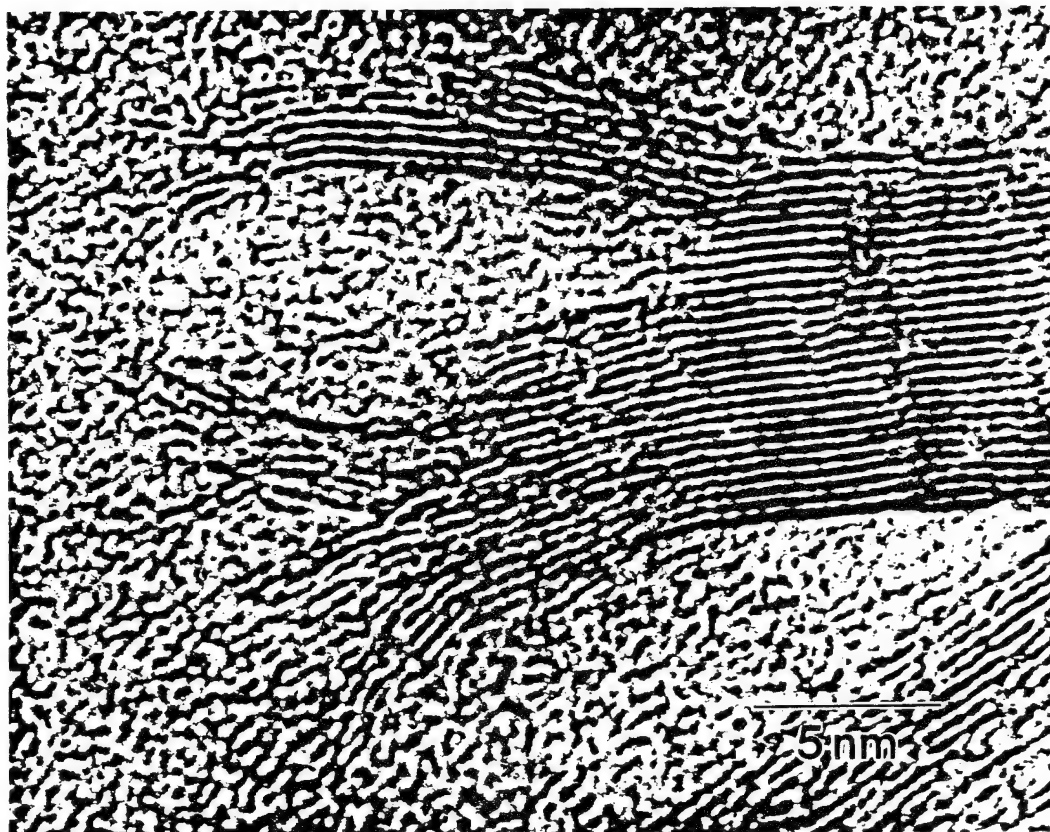
Fig. 1.11 HRTEM image of the a-C/pyrolytic carbon interface showing substantial distortion of the basal planes at the interface.
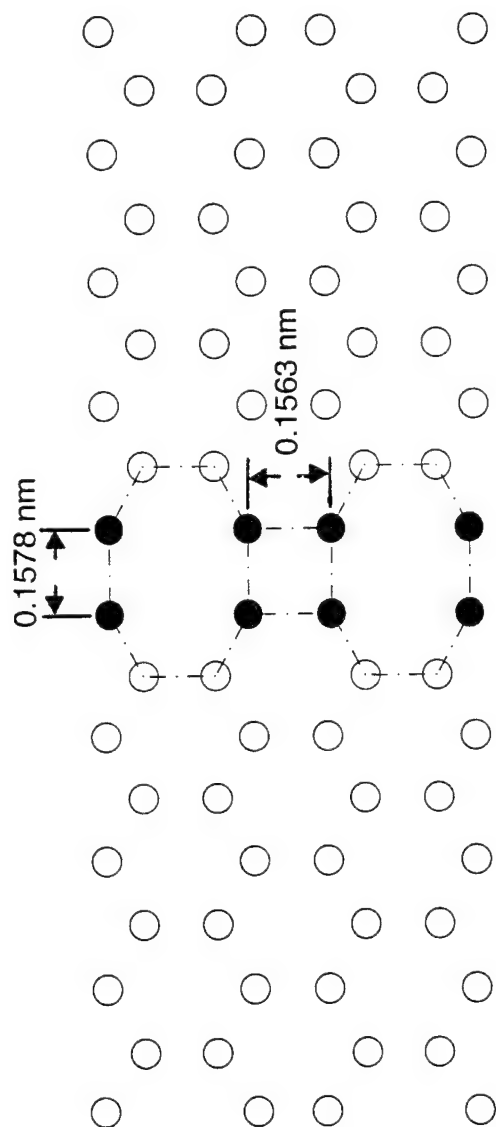
Fig. 1.12 Relaxed 8–4–8 structure at {1121} twin interface shown by dashed line. Bond lengths are shown and the shaded atoms have potential energy of −6.59 ev/atom.
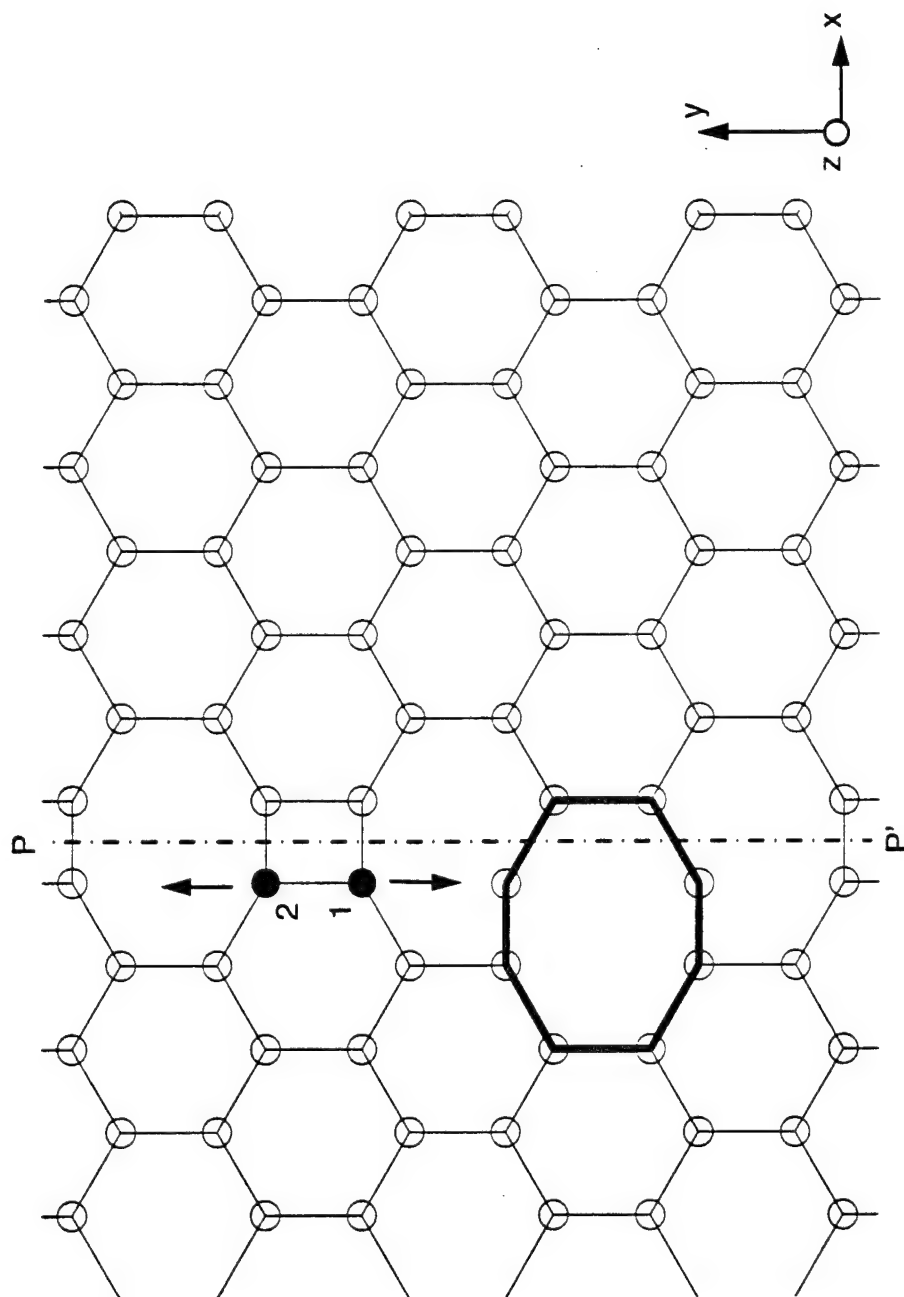
Fig. 1.13 Atomic arrangement of the {11–21} twin interface containing a kink along the boundary. Atoms 1 and 2 (shaded) are displaced in the indicated directions to calculate the energy at a saddle point. Line P–P' shows the twin plane and the kink is shown by the thicker line.
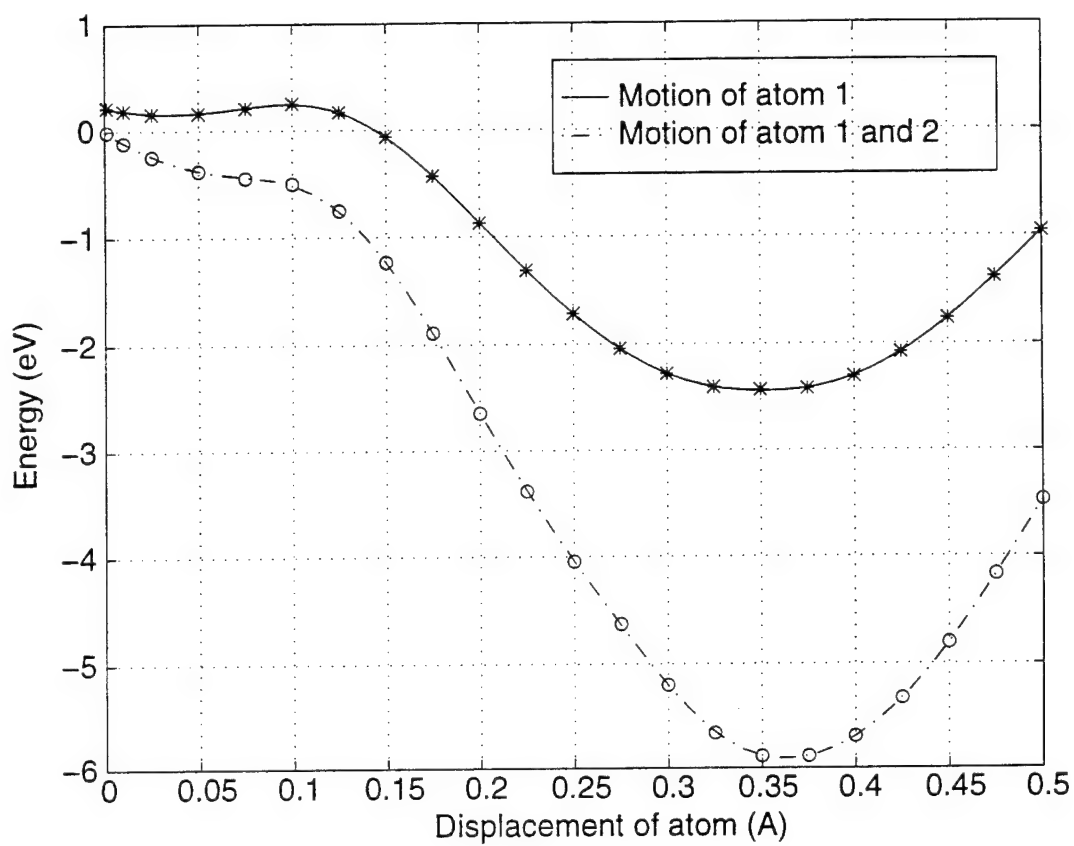
Fig. 1.14 Energy of the system as a function of displacement of the atoms (see Fig. 1.13).

Chapter 2. Research on SiC

2.1 Scope of research

In this study, SiC has been studied in atomistic simulations for the first time by both empirical many-body potential function and tight-binding method. Extensive calculations of the fundamental properties of bulk and surfaces of β-SiC have been performed with special focus on the structural and mechanical behavior of β-SiC under large deformation. The problem addressed in this work is an atomistic study of deformation and unstable structural responses of β-SiC (zincblende structure) under hydrostatic tension and compression through an integrated approach of molecular dynamics (MD) simulations [1] using a modified classical, many-body empirical potential function [2] and self-consistent elastic stability analysis based on the concept of elastic stiffness coefficients [3]. The phenomena being studied are tension-induced crack nucleation and brittle fracture and pressure-induced lattice disordering. An emphasis of the investigation is the clarification of the role of chemical ordering in the amorphization process of β-SiC, specifically, a probe of the relative importance of the atomic size disparity and mixed bonds chemical preference. The elastic stability analysis predicts the instability mechanism and the critical stress at which the instability will occur. However, it does not predict what will happen to the structure of the crystal when it reaches the instability. MD simulation on the other hand is able to provide detailed atomic configurations and allow one to examine the structure of the system at any time instant. Combining the elastic stability analysis and the MD simulations, one can predict the instability mechanism, and the critical stress, or verify the predictions from elastic stability analysis by direct MD simulations, and directly observe the structural changes at the instabilities. In this way, a comprehensive understanding of the elastic instabilities and the unstable structural responses of crystals can be obtained.

The major contributions from this work are the proper implementation of the Tersoff potential, a modification of the potential at large deformation, extensive calculations of fundamental bulk and surface properties, instability analysis and structural responses under hydrostatic tension and compression, construction of crystalline/

amorphous interface, and an estimation of work of adhesion. The results are summarized in the next section. Major equations are presented in the appendix. Papers published/submitted based on this work are also listed in the appendix.

2.2 Results and Discussion

The major results and achievements from this study are summarized below followed by detailed discussions of their significance and implications.

2.2.1 Implementation of the Tersoff potential

 The first significant contribution of this work is the successful implementation of the Tersoff potential to perform constant stress molecular dynamics simulations with full capability to calculate forces, stresses and elastic constants. Analytical derivations of the interatomic force, atomic stress and the elastic constants using fluctuation formula [4] have been obtained. To our knowledge, this is the first time that the fluctuation formulae of elastic constants are properly derived for the Tersoff potential. The derivation has been verified self-consistently with the direct stress-strain method for elastic constants calculations. The fluctuation formulae offer an efficient method to calculate elastic constants under arbitrary stress and temperature conditions. This capability has been invaluable for the elastic stability analysis. The major expressions for the elastic constants are given in the appendix. The fundamental equilibrium properties calculated using the Tersoff potential, the Pearson potential, a tight-binding method and experimental data are summarized in Table 1.

2.2.2 Modification of the Tersoff potential

The original Tersoff potential is useful in describing the mechanical properties of β-SiC at low temperature ($0K$). From this potential, the three elastic constants of β-SiC are calculated to be C_{11}=4.36 $Mbar$, C_{12}=1.20 $Mbar$ and C_{44}=2.55 $Mbar$ compared to the experimental data of 3.90 $Mbar$, 1.42 $Mbar$ and 2.56 $Mbar$ respectively at room temperature. The results are satisfactory considering the fact that the potential

function has not been fitted to elastic constants. However, temperature dependence of the elastic constants are not correctly described by the original Tersoff potential. The elastic constants calculated at room temperature (C_{11} =5.23 *Mbar*, C_{12}=1.63 *Mbar* and C_{44}=3.13 *Mbar*) are inconsistent with the experimental data. Our modified Tersoff potential, on the other hand, not only gives the same elastic constants at *0K*, but also correctly describes the temperature dependence of the elastic constants. The room temperature elastic constants of β-SiC calculated from the modified Tersoff potential are C_{11}=4.25 *Mbar*, C_{12}=1.18 *Mbar* and C_{44}=2.66 *Mbar*, in excellent agreement with experiment. This agreement in C_{44} demonstrates that the modified Tersoff potential can treat rather well the angular dependent forces in covalent SiC.

We have found that the incorrect behavior of the elastic constants at higher temperature is due to the inclusion of second nearest neighbor interactions which impose a strong repulsion to the dominant nearest neighbor interaction. To avoid this strong repulsion and keep the dominant interactions between the first nearest neighbors, we introduce a simple modification which scales the cutoff of the potential with the volume of the system ($V^{1/3}$). In Fig. 2.1, we show the cohesive energy and pressure curve for β-SiC under deformation, where the dashed line is calculated using the universal binding curve [5] and the solid line is calculated by ab initio method. From this figure, it is seen that the modified Tersoff potential gives a very satisfactory description of the behavior of β-SiC under large deformation.

2.2.3 Bulk and Surface Properties

Using the modified Tersoff potential, we have calculated a number of fundamental bulk and surface properties of β-SiC and compared our results with experimental and first-principles calculations extensively. The bulk properties include phonon dispersion curve, equation of state, thermal expansion coefficient and elastic constants at elevated temperatures. The surface properties include surface energy, surface relaxation and reconstruction.

In Fig. 2.2, we show the dispersion curves along high symmetry directions obtained from the Tersoff potential and experimental data [6]. We find that the transverse acoustic modes from the Tersoff potential agree with experimental data very well.

However, the optic modes are underestimated. Also, the optic modes at Γ point are degenerate from the Tersoff potential, while experimental data shows a splitting of transverse and longitudinal branches. This splitting is an indication of charge effects in SiC [7]. Since the Tersoff potential treats β-SiC as a fully covalent material, it naturally can not treat this effect, and therefore can not describe the splitting.

The equation of state, namely the P-V curve, of β-SiC under compression at room temperature (*300K*) is calculated and shown in Fig. 2.3, compared with two sets of experimental data obtained by Bassett et al [8] and Yoshida et al [9]. The symbols are data from the modified Tersoff potential (cross), by Bassett et al (star) and by Yoshida et al (circle). These data are in close agreement with each other. The lines are fitted results using Birch-Murnaghan equation of state [10]

$$P = \frac{3}{2} k_o \left[(\frac{V_o}{V})^{7/3} - (\frac{V_o}{V})^{5/3} \right] \times \left[1 - \frac{3}{4} (4 - k_o') \left((\frac{V_o}{V})^{2/3} - 1 \right) \right] \qquad (1)$$

where V_0 and V are the volume at zero pressure and under deformation respectively, k_0 is the isothermal compressibility, and k_0' is the pressure derivative of k_0. As Fig. 2.3 shows, data from the modified Tersoff potential can be fitted by the Birch-Murnaghan's equation of state very well. Furthermore, we compare the fitted parameters k_0 and k_0' from the three sets of data. The results are shown in Table 4. The values obtained from the modified Tersoff potential agree with the other two reasonably well. This suggests that the modified Tersoff potential describes very well the homogeneous response of β-SiC to hydrostatic compression.

Calculated lattice constant of β-SiC as a function of temperature up to *1500 K* under zero pressure is calculated, shown in Fig. 2.4 and compared with experimental data[11]. The difference between simulation and experiment is less than 1%. Both data from simulation and experiment are fitted to polynomial functions of temperature. The fit from experimental data yields

$$a(nm) = 0.43577 + 1.3887 \times 10^{-6}\, T + 7.8494 \times 10^{-10}\, T^2 - 2.4434 \times 10^{-13}\, T^3 \qquad (2)$$

Whereas the fit from simulation data gives

$$a(nm) = 0.43253 + 2.4719 \times 10^{-6}\, T + 1.5980 \times 10^{-10}\, T^2 + 1.0706 \times 10^{-14}\, T^3 \qquad (3)$$

By definition, the linear thermal expansion coefficient is $\alpha = 1/a\,(\partial a/\partial T)$. From Eq. (2) and Eq. (3), we find that the thermal expansion coefficients determined by simulation to be $\alpha = 2.5 \times 10^{-6}\, /K$, and that determined by experiment is $\alpha = 1.4 \times 10^{-6}\, /K$. The modified Tersoff potential therefore produces satisfactory thermal expansion coefficient and gives a reasonable account of the anharmonic effecst which control the thermal expansion.

Elastic constants at finite temperatures have been calculated using the fluctuation formula. The results are shown in Fig. 2.5, along with literature data. As the comparison shows, significant improvement of the elastic constants at elevated temperatures is achieved by the modified Tersoff potential. Also, for the temperature range being studied, all elastic constants show the expected thermal softening behavior [12] and they can be well fitted as linear functions of temperature. The variation coefficients of the elastic constants are summarized in Table 2.5, which show that the modified Tersoff potential predicts good elastic constants behavior at elevated temperatures.

The results of unrelaxed surface energies of β-SiC are given in Table 2.6. The shuffle-(111) surface has the lowest surface energy. This is to be expected since the shuffle-(111) has the lowest density of bonds. The only experimental value of surface energy reported in the literature is 2180 erg/cm^2 [13], which agrees with our result of 2525 erg/cm^2 quite well.

Surface relaxation of (100) and (111) planes have been performed. In Table 2.7, results of energy decreases and vertical displacements of atoms during surface relaxation are summarized. Also shown in the table are results obtained from the Pearson potential[14], tight-binding calculation[15] and ab initio calculation[16]. For the energy decrease dE, the Tersoff potential gives better results for Si-(100) and Si-(111), while the Pearson potential gives better results for C-(100) and C-(111). We believe this is because that the Pearson potential has used some information of C clusters during the fitting procedures. For the displacements of dH_1, dD_{12} and dH_2, the Tersoff potential always gives better results than the Pearson potential. Also, dH_1

and dD_{12} from the Tersoff potential are in excellent agreement with the tight-binding calculations. For the (100) and (111) surface relaxation, the C surfaces exhibit larger inward displacements and gain more energy than the Si surfaces. This is because C has a stronger tendency to form sp^2 based planar structure. For all surfaces, contraction of the top two layers during relaxation is observed.

Another aspect of surface relaxation involves the change in symmetry of the surface layer relative to the structure embedded in the bulk. Several reconstruction patterns have been observed in experiments. Two typical ones are the 2 x 1 and 2 x 2. Here we study the (100) surface reconstruction of β-SiC by the Tersoff potential and the Pearson potential. We have observed 2 x 1 and 2 x 2 dimers on both C-(100) and Si-(100) surfaces using the Tersoff potential. For the Pearson potential, no 2 x 1 dimers are observed on the Si-(100) surface.   In Table 2.8, we summarize the results from the Tersoff potential, the Pearson potential and the tight-binding calculation. From the bond lengths and energy gain, we find that the 2 x 1 reconstruction is favored over the 2 x 2 reconstruction, which is in agreement with the tight-binding calculation.

2.2.4 Crack Nucleation and Brittle Fracture Under Tension

Under hydrostatic tension and at room temperature, we have studied the elastic instability and the unstable structural response of β-SiC combining the newly developed elastic instability analysis [17] with molecular dynamics simulations. The elastic stability criteria for a cubic crystal is

$$K(P) = (C_{11} + 2\,C_{12}) \,/\, 3 + P/3 > 0 \qquad (4)$$
$$G'(P) = (C_{11} - C_{12}) \,/\, 2 - P > 0$$
$$G(P) = C_{44} - P > 0$$

where K is called the spinodal instability, G the shear instability, and G' the tetragonal shear instability. Fig. 2.6 shows how the three instability criteria vary with tensile loading. It is found that under tension, the spinodal stability criterion $K(P)$ reaches zero first and determines the instability mechanism. The critical pressure and strain predicted from this instability analysis are $\eta_c = r/r_0 - 1 = 0.153$ and $P_c = 0.370\ Mbar$. On the other hand, we perform constant stress molecular dynamics

simulations under tension. Fig. 2.7 shows the overall system responses to the applied tension. One sees that the instability manifests as an abrupt release in internal pressure, increase in potential energy, and increase in lattice parameter. And the observed critical pressure is P_c= 0.369 *Mbar* which is in close agreement with that predicted by the stability analysis.

In order to see in more detail the nature of the instability we show in Fig. 2.8 the time-dependent variation of the shape of the simulation cell, expressed in terms of elements of the matrix $\underline{h}$, and correspondingly, the elements of the internal stress tensor. Also given in Fig. 2.8 is the variation of the energy per atom. Although the temporal evolution behavior shown in Fig. 2.8 indicates a rather complex structural response which involves dilatation as well as shear deformation, one can not tell precisely what is the structural response of the lattice. For more information, it is necessary to scrutinize the molecular dynamics trajectories in greater detail. We now show that the unstable structural responses described in Fig. 2.8 correspond to crack nucleation and brittle fracture. Fig. 2.9 shows a sequence of the instantaneous atomic configurations obtained at four instants during the simulation. The simulation cell is oriented to display the stacking sequence along the body diagonal $[1\bar{1}1]$,... =Si-C=Si-C=Si-..., where - and = denote alternating interplanar separation distances of l/12 and l/4 (l is the length of the body diagonal of the unit cell), respectively. The stacking of alternating $\{1\bar{1}1\}$ planes which contain only Si or C is most clearly visible in Fig. 2.9 (a), at the stage of simulation (about 0.3ps after the applied stress is increased from Σ =5.55 to 5.575) when lattice instability apparently has not yet set in. In Fig2.9 (b) the atomic configuration at 0.45ps into the simulation clearly indicate a crack opening from the right on the shuffle plane in the lower right part of the cell. In addition, there appears somewhat less pronounced distortion in the upper left part of the cell. In Fig. 2.9 (c), the configuration at 0.06ps later, we see both nucleated cracks begin to propagate and atomic relaxation on the crack surfaces become visible. Specifically one can see the appearance of mixing of Si and C atoms on the crack surfaces (a layer is visualized by imaging a line drawn through the centers of atoms). In Fig. 2.9 (d) the configuration after another 0.09ps shows quite clearly the consequence of the structural instability induced by the tension loading. Both cracks have propagated in a rather clean fashion through the simulation cell, with crack surfaces which appear

to be well relaxed.   The foregoing results show that brittle fracture has occurred on the {1$\bar{1}$1} shuffle plane. This is not unexpected considering that the unrelaxed surface energies, given in Table2.6, show that the shuffle {111} plane is indeed the one with lowest energy.

2.2.5 Pressure-induced Amorphization

While crack opening and brittle fracture occurs in β-SiC under tension at the spinodal instability, the structural response of β-SiC under compression is more complicated. We have observed pressure-induced amorphization in SiC which is driven by the elastic shear instability. Fig. 10 shows the overall system responses to the applied compression as a function of the internal pressure P. As shown in Fig 2. 10 (a), the structure factor $s(k)$ suddenly drops to zero. Correspondingly, we see an internal energy decrease in Fig. 2.10 (b) and a volume increase in Fig 2.10 (c). All these suggest a change in the β-SiC structure. The critical pressure observed is P_c= 707 GPa. In order to show more detailed change of properties of the system, we plot the time-dependent system responses in Fig. 2.13, where one clearly sees that, during the transition the off-diagonal elements grow to non-zero values indicating a shear deformation of the system. In order to examine the final structure, we plot the atomic configuration projections along x, y and z directions in Fig. 2.11, which show a completely disordered structure. To elucidate the driving force of the amorphization, we have carried out elastic stability analysis using the criteria in Eq. (4). First, we perform the stability analysis at $0K$ and identify that the instability mechanism of β-SiC under compression is the shear instability $G'(P)$, shown in Fig. 2.12 (a). Then, we calculate the shear instability criterion at $300K$ and obtain the critical pressure of 714 GPa, which is in good agreement with that observed directly in the MD simulation. Also, we have found that the vanishing of the shear instability is due to large fluctuation of shear stresses caused by internal strain relaxation of atoms.

The fact that SiC amorphizes under compression stands in contrast to the behavior of elemental Si which undergoes polytypic phase transformation under compression (from diamond cubic to β-tin) [18]. As shown in Fig. 2.12 (b), for Si in the diamond structure both $G(P)$ and $G'(P)$ decrease under sufficient compression, with $G'(P)$

vanishing first at $r / r_0 = 0.86$ and corresponding pressure of 111 GPa.

Since this tetragonal shear instability results in a transition from diamond cubic to β-Sn structure, one may ask, in view of Figs. 2.12 (a) and 2.12 (b), what is the origin of the different structural response to compression between β-SiC and Si. To address this question we consider the two fundamental effects associated with the binary nature of β-SiC, a difference in the atomic sizes of C and Si, and the chemical preference of Si (C) to have the other species as its nearest neighbors. To separate the effects of size disparity from that of mixed bond preference, we note that the Tersoff potential is of the form $V_{ij} = f_c(r_{ij})[A_{ij} e^{-\lambda_{ij}r_{ij}} - B_{ij} \chi b_{ij}] e^{-\mu_{ij}r_{ij}}$, where the two effects are described through the bond order parameter b_{ij} and the factor χ, respectively. Since $\chi = 1$ when i and j refer to atoms of the same species, its value affects only V_{si-c} and V_{c-si}, and therefore the heat of formation ΔH. On the other hand, to suppress the effect of atomic size difference, one can simply set $b_{c-j}=b_{si-j}$ in functional form. This observation leads us to examine two idealizations of the Tersoff potential, one in which mixed bond preference is suppressed through adjusting χ to give $\Delta H = 0$ (model I), and another in which size difference is suppressed by the method just described while at the same time adjust χ so that ΔH remains unchanged (model II). In Table 2.9 the elastic constants, lattice parameter, and cohesive energy calculated for the two idealized models at equilibrium configuration and 0 K are compared with values for the full model. It is clearly seen that while the elimination of chemical bond preference has little effect, all three elastic constants are significantly altered in the absence of atomic size difference. Although both (C_{11}- C_{12}) and C_{44} are appreciably reduced, the lowering of the former is more drastic such that in model II the elastic instability is found to be the vanishing of G'. This result is consistent with the behavior obtained in the case of Si. Thus we have shown that the difference between SiC and Si in compression-induced structural response lies in the dominant role of atomic size effect. In other words, amorphization occurs in SiC because the onset of vanishing of G precludes a polymorphic transition associated with the instability of $G' = 0$. To demonstrate that this is the correct interpretation, we have carried out a simulation of model II under compression and indeed observed a transition from zincblende to rock salt structure which is triggered by the tetragonal shear instability.

2.3 Conclusions

We have demonstrated that the bond-order potential developed by J. Tersoff gives a generally satisfactory description of the interatomic interactions of β-SiC provided one considers only the interactions between nearest neighbors. Since the model involves the assumption of a completely covalent material, no charge effects are taken into account. This means that the model will not give the splitting of the optic phonon mode at X point and the buckling behavior of the (100) surface relaxation. Nevertheless, the modified Tersoff is superior to all other existing empirical potential models for SiC.

We need to keep in mind that classical potential models are inherently limited in their transferability in that they are restricted to system configurations close to those at which the properties have been fitted. We have investigated a tight binding approach to modelling β-SiC [19] with moderate success. Because the method is computationally intensive, we have applied it only to rather small systems. Thus far we have obtained reasonable values for the elastic constants, and similar behavior of a crack nucleation under hydrostatic tension.

An important goal of this work is to study the deformation responses of a binary covalent lattice to hydrostatic tension and compression using an atomistic approach of self-consistent elastic stability analysis combined with molecular dynamics simulations. The use of a classical potential models has allowed us to demonstrate the practical feasibility of modelling mechanical behavior of crystals under stress; moreover, it has also enabled us to highlight the role of chemical ordering and the relative importance of atomic size and mixed-bond preference effects in the process of pressure-induced amorphization.

Concerning future investigations using the models and methodologies we have developed here, we believe that our work provides a starting point for modelling thermomechanical properties of a class of covalent materials which hold considerable technological interest, with focus on heterogeneous systems such as composite interface, grain boundaries and dislocations. Because atomistic simulation is able to treat properly temperature and nonlinear stress effects, issues such as interfacial

strength, thermal stress, deformation and debonding at interfaces, in principle, all can be addressed, although none of those problems will be straightforward extensions.

2.4 List of Papers Published/Submitted

o *Lattice instability in* β*-SiC and simulation of brittle fracture*, M. Tang and S. Yip, J. Appl. Phys. **76,** 2719 (1994).

o *Atomic size effects in pressure-induced amorphization of SiC*, M. Tang and S. Yip, Phys. Rev. Lett., submitted.

o *Modeling and simulation of structural, mechanical and thermal properties of* β*-SiC*, M. Tang and S. Yip, Phys. Rev. B, submitted.

o *Elastic instability driven amorphization in SiC*, M. Tang and S. Yip, Phys. Rev. B, in preparation.

2.5 References

[1] M. Parrinello and A. Rahman, J. Appl. Phys. **52**, 7182 (1981).

[2] J. Tersoff, Phys. Rev. B **39**, 5566 (1989).

[3] J. Wang, S. Yip, S. R. Phillpot, and D. Wolf, Phys. Rev. Lett. **71**, 4182 (1993).

[4] J. R. Ray, Comp. Phys. Rept. **8**, 109 (1988).

[5] J. H. Rose, J. R. Smith, F. Guinea and J. Ferrante, Phys. Rev. B **29**, 2963 (1984).

[6] D. W. Feldman, J. H. Parker, W. J. Choyke, and L. Patrick, Phys. Rev. **173**, 787 (1968).

[7] E. O. Kane, Phys. Rev. B **31**, 7865 (1985).

[8] W. A. Bassett, M. S. Weathers, and T. C. Wu, J. Appl. Phys. **74**, 3824 (1993).

[9] M. Yoshida, A. Onodera, M. Ueno, K. Takemura, and O. Shimomura, Phys. Rev. B **48**, 10587 (1993).

[10] F. Birch, J. Geophys. Res. **83**, 1257 (1978).

[11] Z. Li and R. C. Bradt, J. Mat. Sci. **21**, 4366 (1986).

[12] K. S. Cheung, A. Argon, and S. Yip, J. Appl. Phys. **69**, 2088 (1991)

[13] B. N. Oshcherin, Phys. Stat. Sol. (a) **34**, K181 (1976)

[14] E. Pearson,T. Takai, T. Halicioglu, and W. A. Tiller, J. Crys. Growth **70**, 33 (1984).

[15] S. P. Mehandru and A. B. Anderson, Phys. Rev. **42**, 9040 (1990).

[16] D. H. Lee and J. D. Joannopoulos, J. Vac. Sci. Technol. **21**, 351 (1982).

[17] J. Wang, S. Yip, S. R. Phillpot, and D. Wolf, Phys. Rev. Lett. **71**, 4182 (1993)

[18] K. Mizushima, S. Yip and E. Kaxiras, Phys. Rev. B **50**, 14952 (1994)

[19] A. Isik, Ph. D. Thesis, Massachusetts Institute of Technology, Department of Nuclear Engineering, 1994.

Appendix A: tables and figures

Table 2.1 Comparison of β-SiC properties by the Tersoff potential (TP), Pearson potential (PP), tight-binding method (TBA) and from experiment (Exp't). r is the lattice parameter; E is the cohesive energy; B is the bulk modulus.

	TP	PP	MEAM	TBA	Exp't
r (Å)	4.32	4.19	4.2	4.36	4.36
E (ev)	-6.18	-7.71	-6.4		-6.34
B (Mbar)	2.25	9.90	2.11	2.29	2.25
C_{11}(Mbar)	4.36	10.95		3.72	3.90
C_{12} (Mbar)	1.20	9.37		1.57	1.42
C_{44} (Mbar)	2.55	6.06	2.05	2.56 (unrelaxed)	2.56

Table 2.2 Cutoff values (in units of Å) for β-SiC at zero pressure at $0K$.

	$R_{C\text{-}C}$	$S_{C\text{-}C}$	$R_{Si\text{-}Si}$	$S_{Si\text{-}Si}$	$R_{C\text{-}Si}$	$S_{C\text{-}Si}$
Modified	1.93	2.13	2.60	2.80	2.36	2.56
Original	1.80	2.10	2.70	3.00	2.20	2.51

Table 2.3 Elements of force constant matrix (in units of $eV/Å^2$) between nearest neighbors in β-SiC. $D_{\alpha\alpha}$ stands for D_{xx} and, D_{yy} and D_{zz}; $D_{\alpha\beta}$ stands for $D_{xy}, D_{xz}, D_{yx}, D_{yz}, D_{zx}$ and D_{zy}.

	Lee and Joannopolous	Tersoff
$D_{\alpha\alpha}$	-5.66	-7.59
$D_{\alpha\beta}$	-3.08	-3.37

Table 2.4 Comparison of bulk modulus k_0 and its pressure derivative and its derivative k_0'.

	k_0 (GPa)	k_0'
present study	219 1	4.11 0.05
Yoshida et al	260 9	2.9 0.3
Bassett et al	230 4	4.0 (fixed)

Table 2.5 Variations coefficients of elastic constants as a function of temperature (in units of $GPa/°C$).

	dC_{11}/dT	dC_{12}/dT	dC_{44}/dT
present study	-0.036	-0.0046	-0.038
Li and Bradt	-0.025	-0.011	-0.007

Table 2.6 Unrelaxed surface energies of β-SiC from the modified Tersoff potential

Planes	Energy (erg/cm^2)
shuffle (111)	2525
(110)	3093
(100)	4618
glide (111)	8219

Table 2.7 Summary of energy decrease and vertical layer displacements due to surface relaxation of β-SiC. dE is the energy decrease per atom; dH_n is the averaged atomic displacement from its bulk position in the nth-layer; dD_{mn} is the change in percentage of interlayer spacing between nth and mth layers compared to their bulk spacing. Negative (or positive) sign represents inward (or outward) movement to (or away from) the bulk.

		Tersoff Potential	Pearson Potential	Tight Binding	Ab Initio
C- (100) Relaxation	dE (ev / Atom)	0.46	0.25	0.34	
	dH_1 (Å)	-0.17	-0.15	-0.17	
	dD_{12} (%)	-23.0	-14.0	-22.0	
	dH_2 (Å)	0.04	-0.01	0.07	
Si- (100) Relaxation	dE (ev / Atom)	0.09	0.18	0.02	
	dH_1 (Å)	-0.04	-0.07	-0.04	
	dD_{12} (%)	-6.2	-8.4	-4.6	
	dH_2 (Å)	0.03	-0.02	0.01	
C- (111) Relaxation	dE (ev / Atom)	0.83	0.62	0.43	
	dH_1 (Å)	-0.27	-0.30	-0.21	
	dD_{12} (%)	-51.2	-61.2	-52.4	
	dH_2 (Å)	0.05	0.08	0.12	
Si- (111) Relaxation	dE (ev / Atom)	0.11	0.31	0.03	
	dH_1 (Å)	-0.04	-0.06	-0.05	
	dD_{12} (%)	-11.8	-20.5	-11.1	
	dH_2 (Å)	0.03	0.06	0.02	
Si- (111) Relaxation	dE (ev / Atom)	0.29	0.41		0.21
	dH_1 (Å)	-0.17	-0.15	-0.17	
	dD_{12} (%)	-23.0	-14.0	-22.0	
	dH_2 (Å)	0.04	-0.01	0.07	

Table 2.8 Surface reconstruction of the (100) surfaces of β-SiC. r is the bond length (in units of Å); dE is the energy gain (in units of ev); and dL is the top layer lateral displacement (in units of Å).

		dE		r		dL	
		2 x 1	2 x 2	2 x 1	2 x 2	2 x 1	2 x 2
C-(100)	TP (SiC)	2.42	2.29	1.48	1.49	0.79	0.78
	PP (SiC)	2.97	2.90	1.49	1.49	0.74	0.73
	TB (SiC)	2.31		1.74		0.67	
Si-(100)	TP (SiC)	0.67	0.63	2.46	2.54	0.30	0.26
	PP (SiC)	No dimer	0.41	No dimer	2.49	No dimer	0.24
	TB (SiC)	1.03		2.16		0.45	

Table 2.9 Comparison of properties calculated using the Tersoff potential and the two idealizations, models I and II.

	Tersoff	model I	model II
lattice parameter (Å)	4.32	4.34	4.32
cohesive energy (eV)	-6.19	-6.03	-6.19
bulk modulus (Mbar)	2.25	2.18	2.25
C_{11} (Mbar)	4.36	4.19	3.31
C_{12}	1.20	1.17	1.72
C_{44}	2.56	2.42	1.61
$C_{11}-C_{12}$	3.16	3.02	1.59
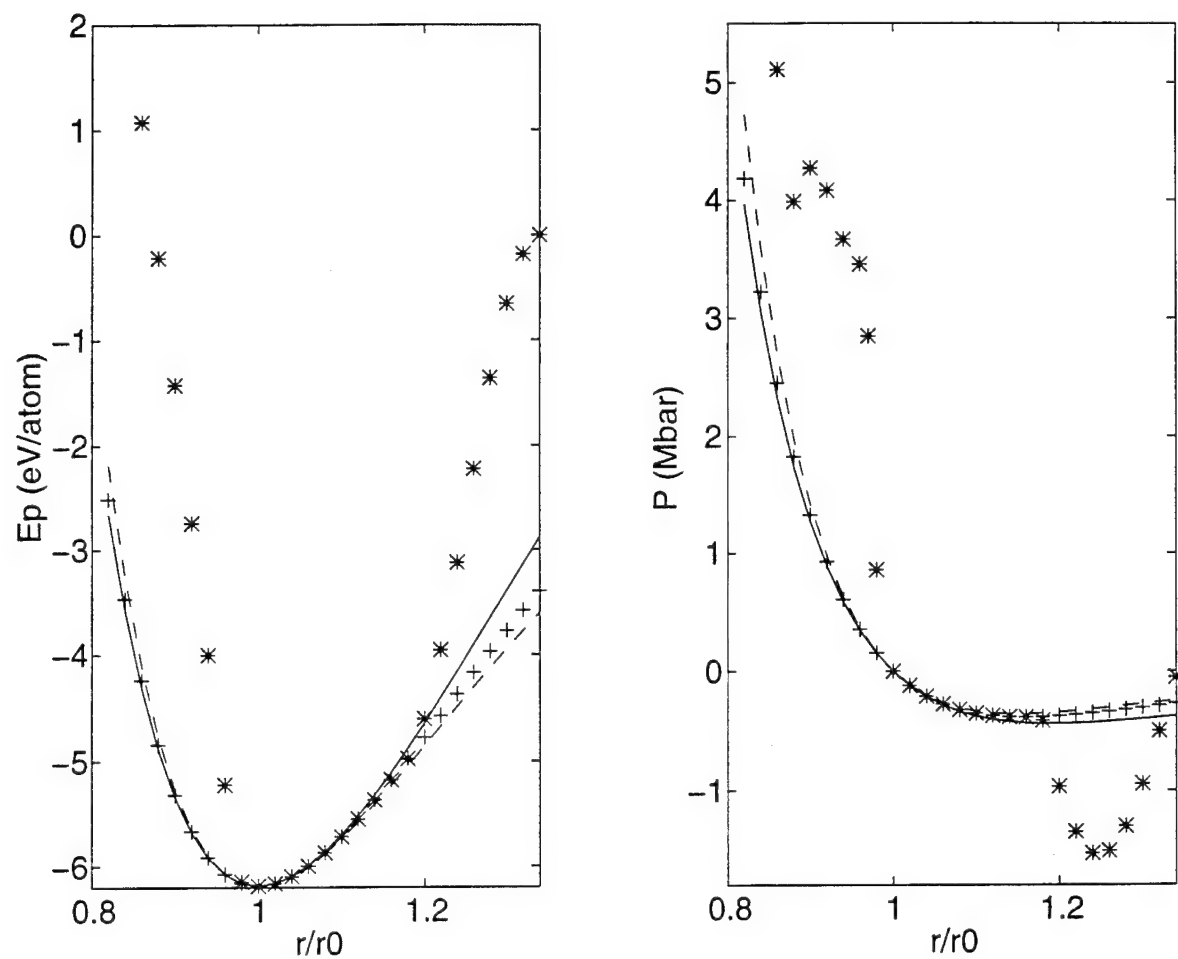
Fig. 2.1 Comparison of (a) cohesive Energy (eV/atom) and (b) pressure of β-SiC under deformation at $0K$. Solid line: ab initio calculation; dashed line: universal binding curve; star: original Tersoff potential; cross: modified Tersoff potential.
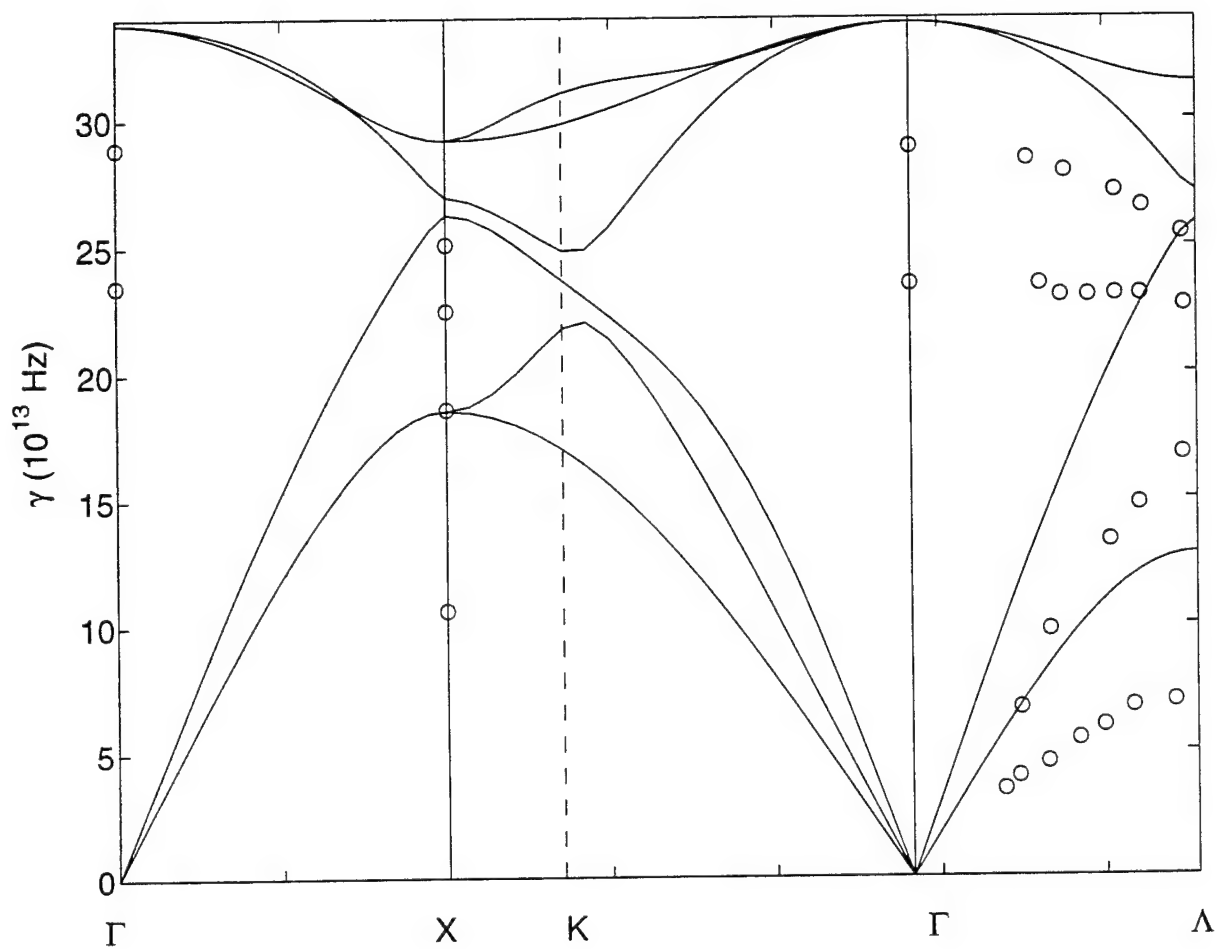
Fig. 2.2 Phonon dispersion curves of β-SiC at $0K$ under zero pressure. Circles are experimental data.
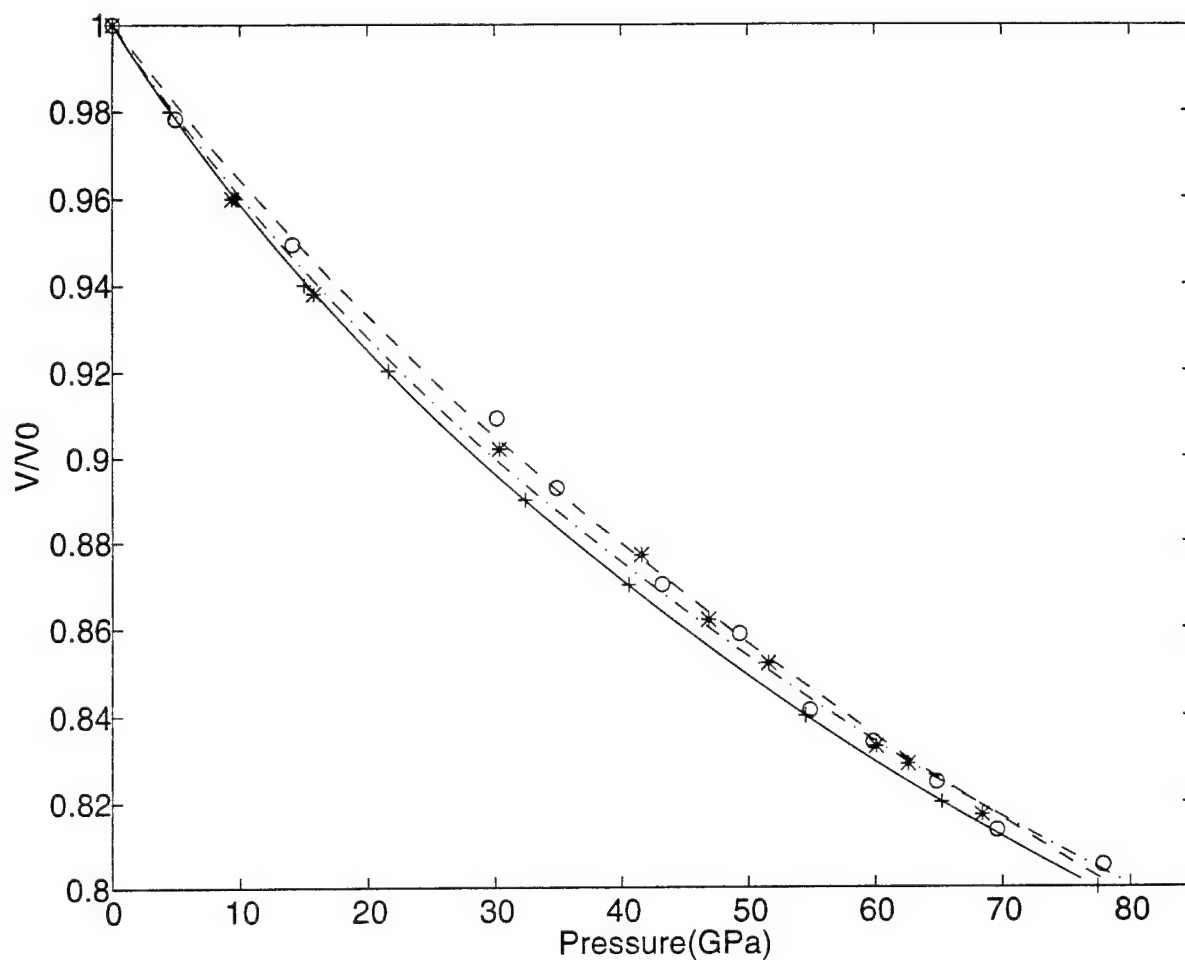
Fig. 2.3 Pressure-volume curve for β-SiC under compression. Circles and dashes line are data and fitted function obtained by Yoshida et al; stars and chained line are data and fitted function obtained by Bassett et al; crosses and solid line are data and fitted function from the modified Tersoff potential.
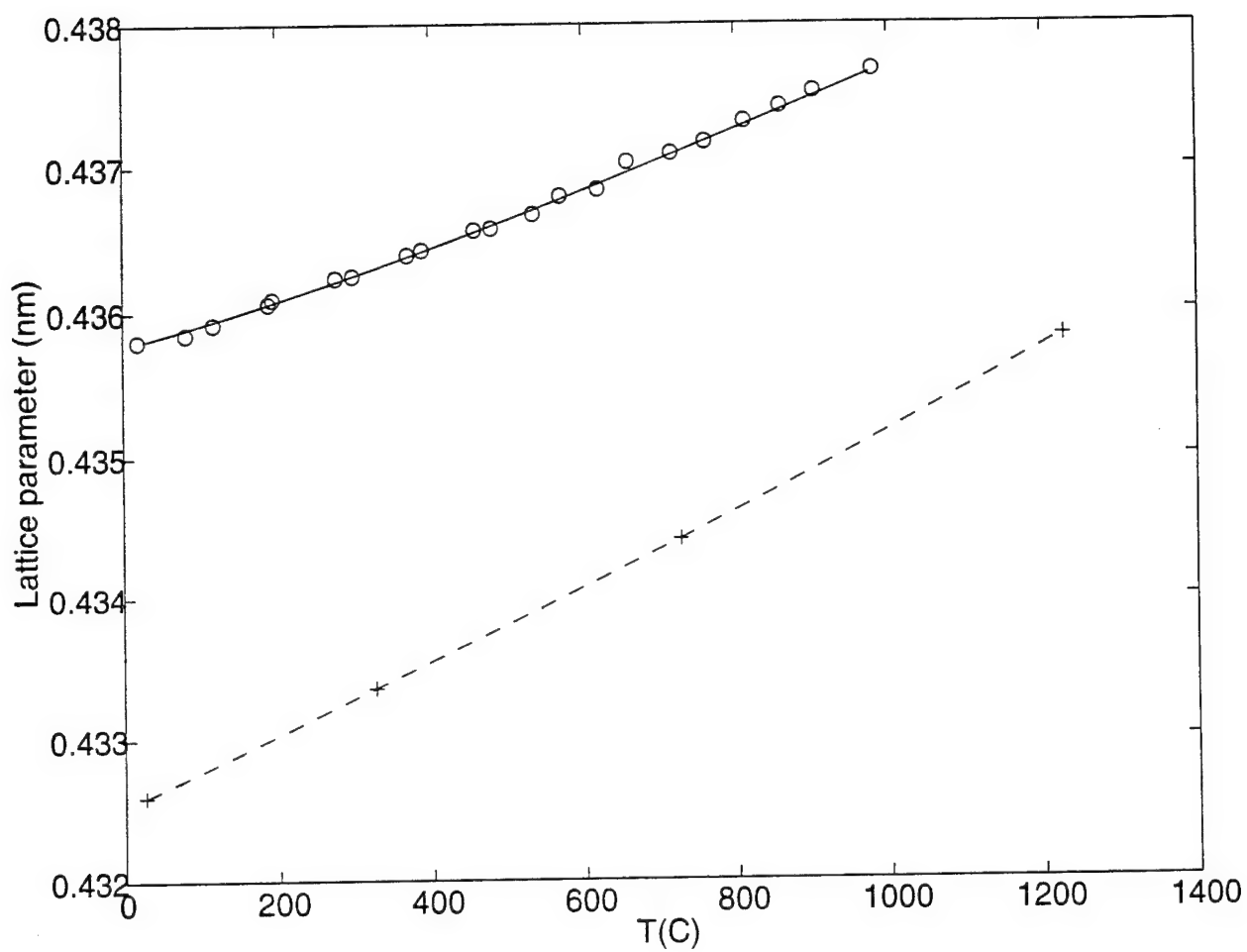
Fig. 2.4 β-SiC lattice constant versus temperature. Circles: experimental data; solid line: fitted from circles; cross: simulation data; dashed line: fitted from crosses.
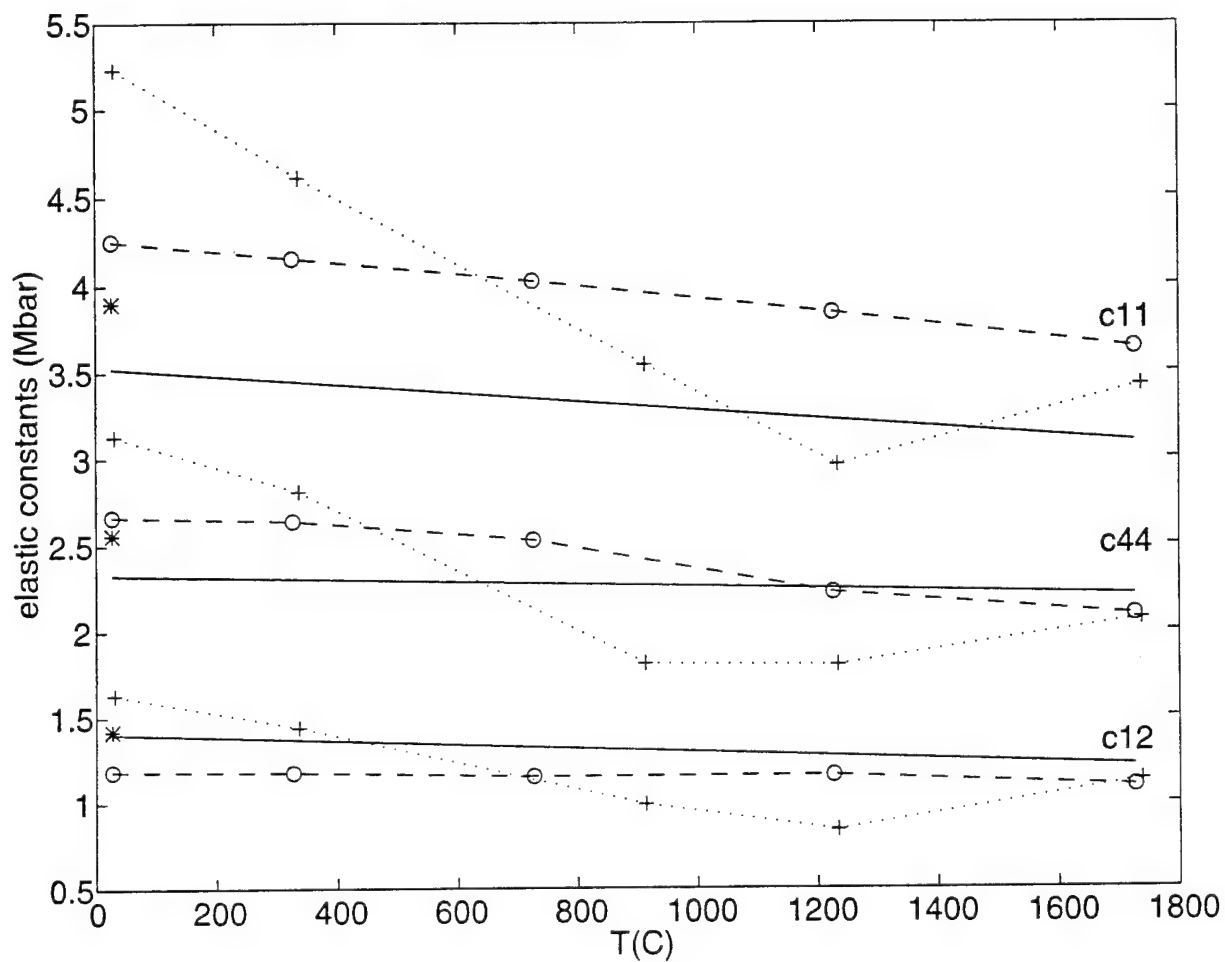
Fig. 2.5   Temperature variation of elastic constants of β-SiC. Circles: data from the modified Tersoff potential; dashed line: fitted from the circles; solid line: results of I and Bradt; cross: data obtained by the original Tersoff potential; dotted line: lines to guide the eyes. Stars are experimental data of β-SiC at 300K.
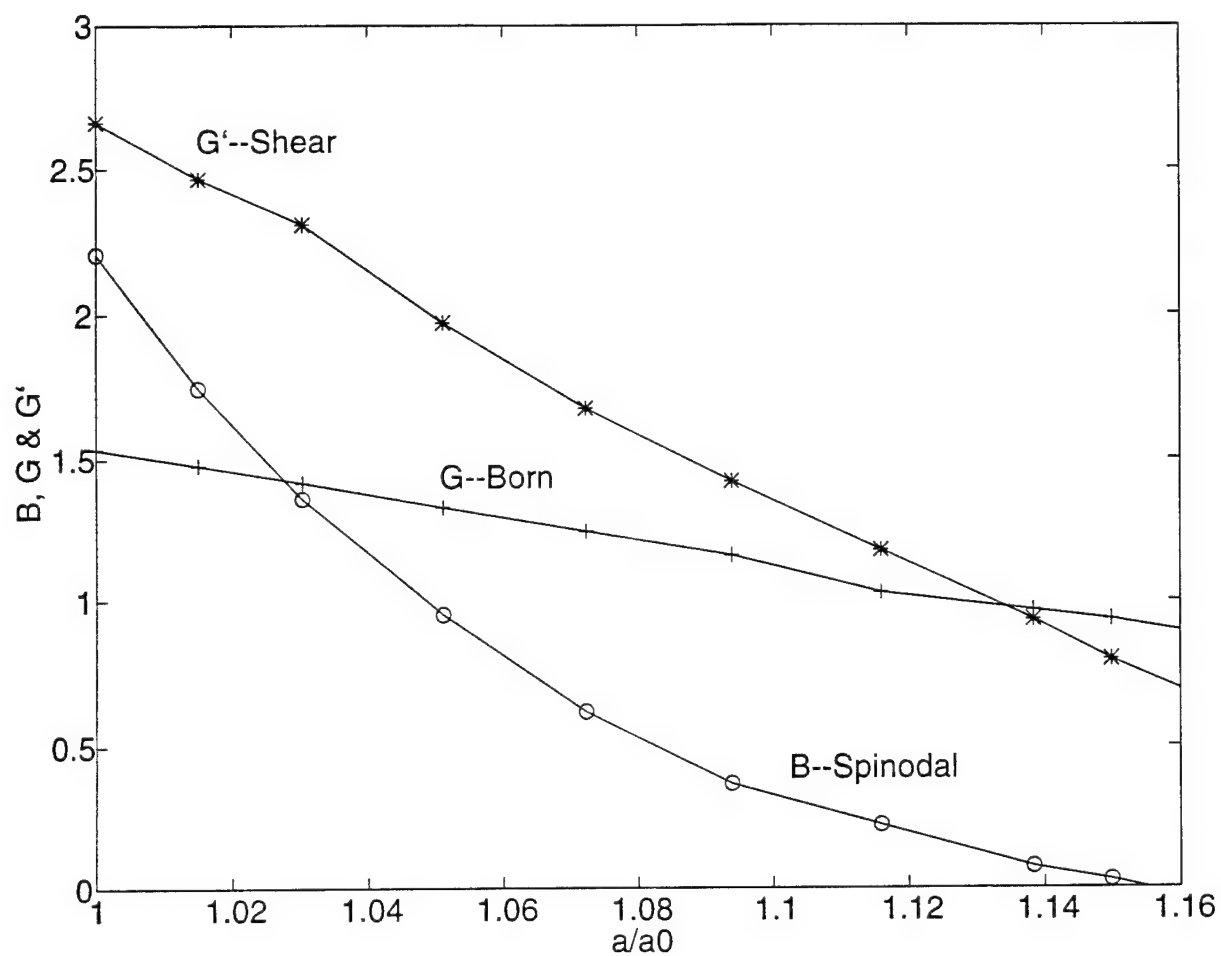
Fig. 2.6 Elastic stability criteria. Closed symbols are from stiffness coefficients and open symbols are from elastic constants. Arrows indicate where the spinodal stability is violated. Lines are drawn to connect the data points.
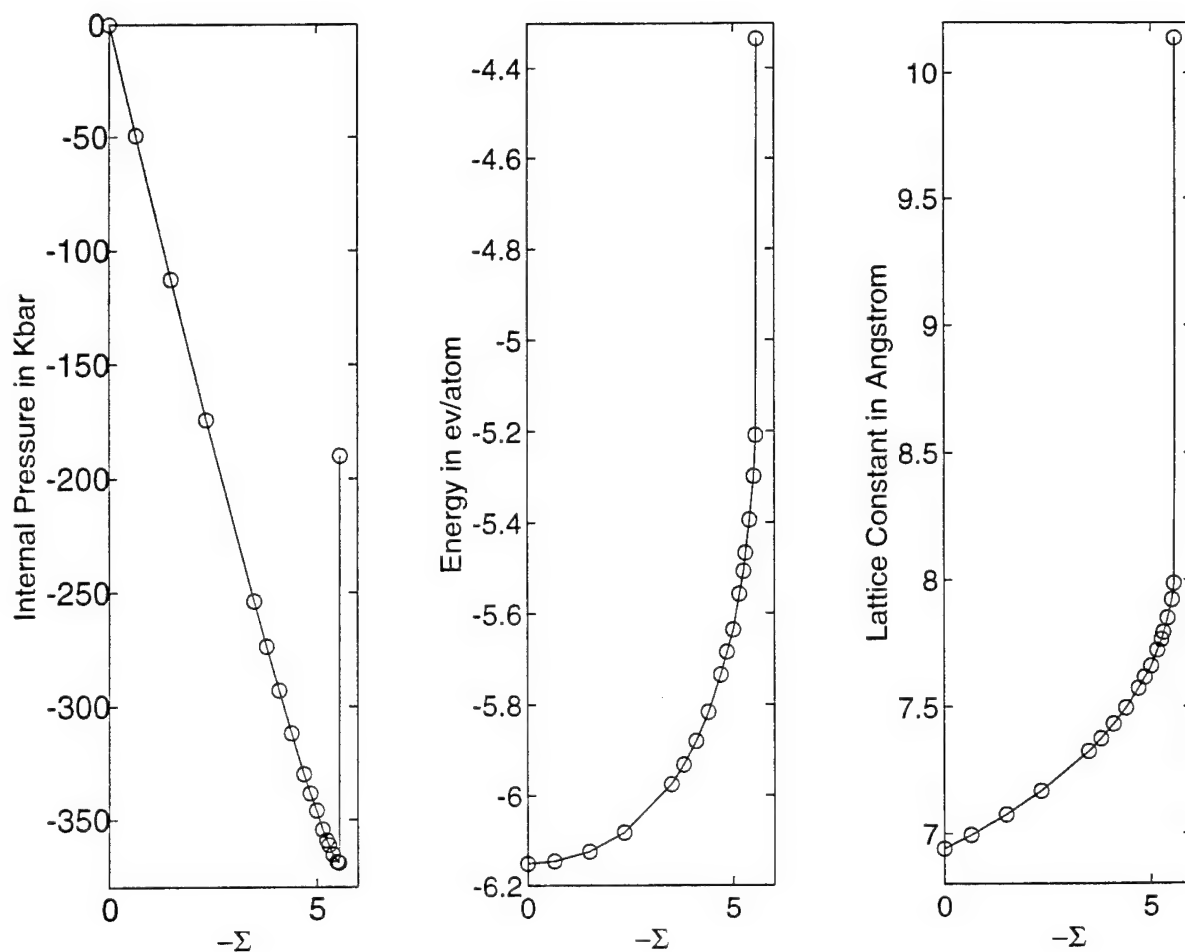
Fig. 2.7 System responses of β-SiC at 300K to applied hydrostatic tension simulated using the modified Tersoff potential. Results for internal pressure P, potential energy Ep, and lattice parameter r are values averaged over the length of each simulation run except for the last point where the system has become unstable and continued to change in time.
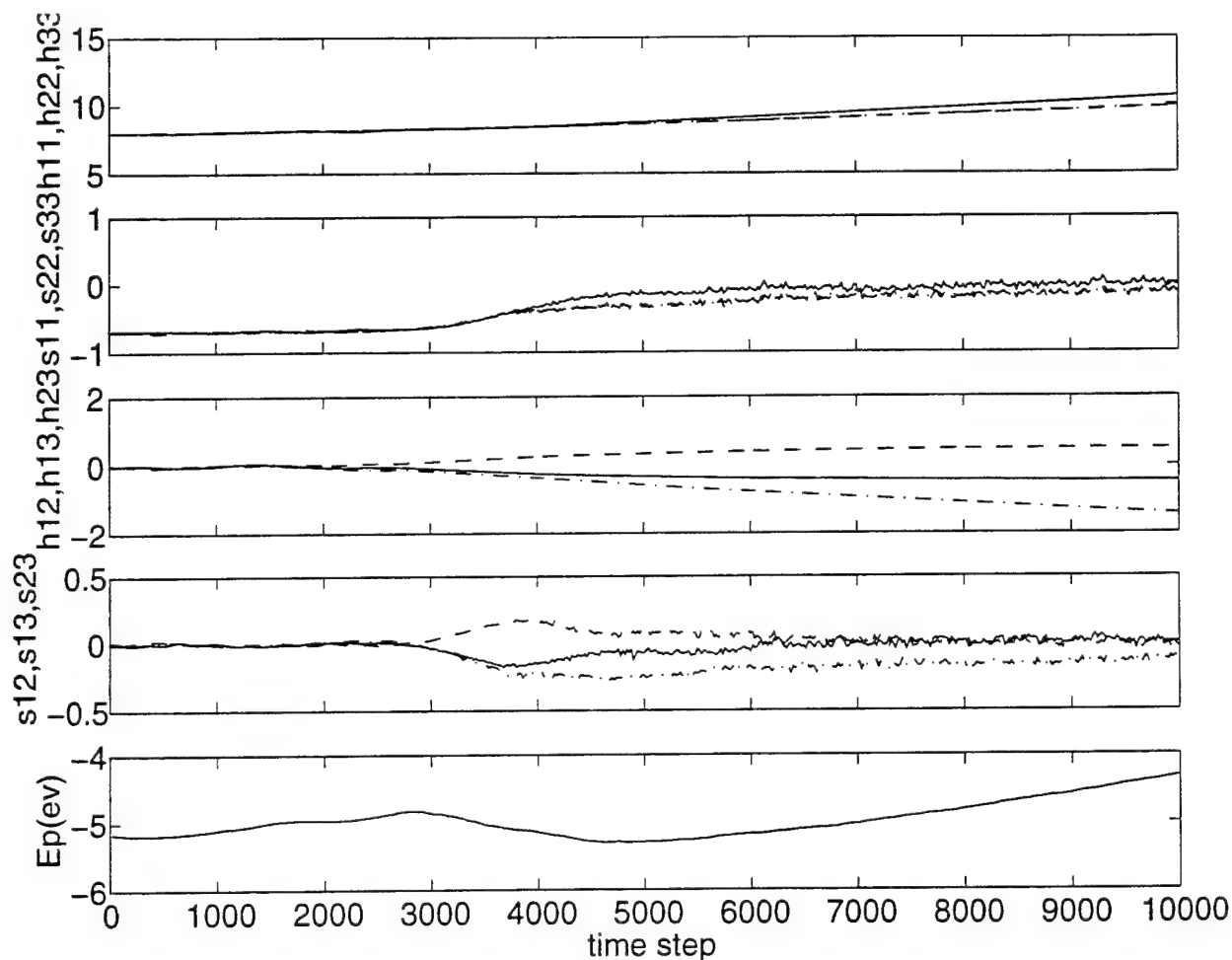
Fig. 2.8 Time-dependent system responses at $\Sigma = 5.575$, from top to bottom are (a) diagonal elements of h matrix (in unit of Å), (b) diagonal elements of stress tensor (in unit of $Mbar$), (c) off-diagonal elements of cell matrix (in unit of Å), (d) off-diagonal elements of stress tensor (in unit of $Mbar$), (e) potential energy per atom (in unit of ev).
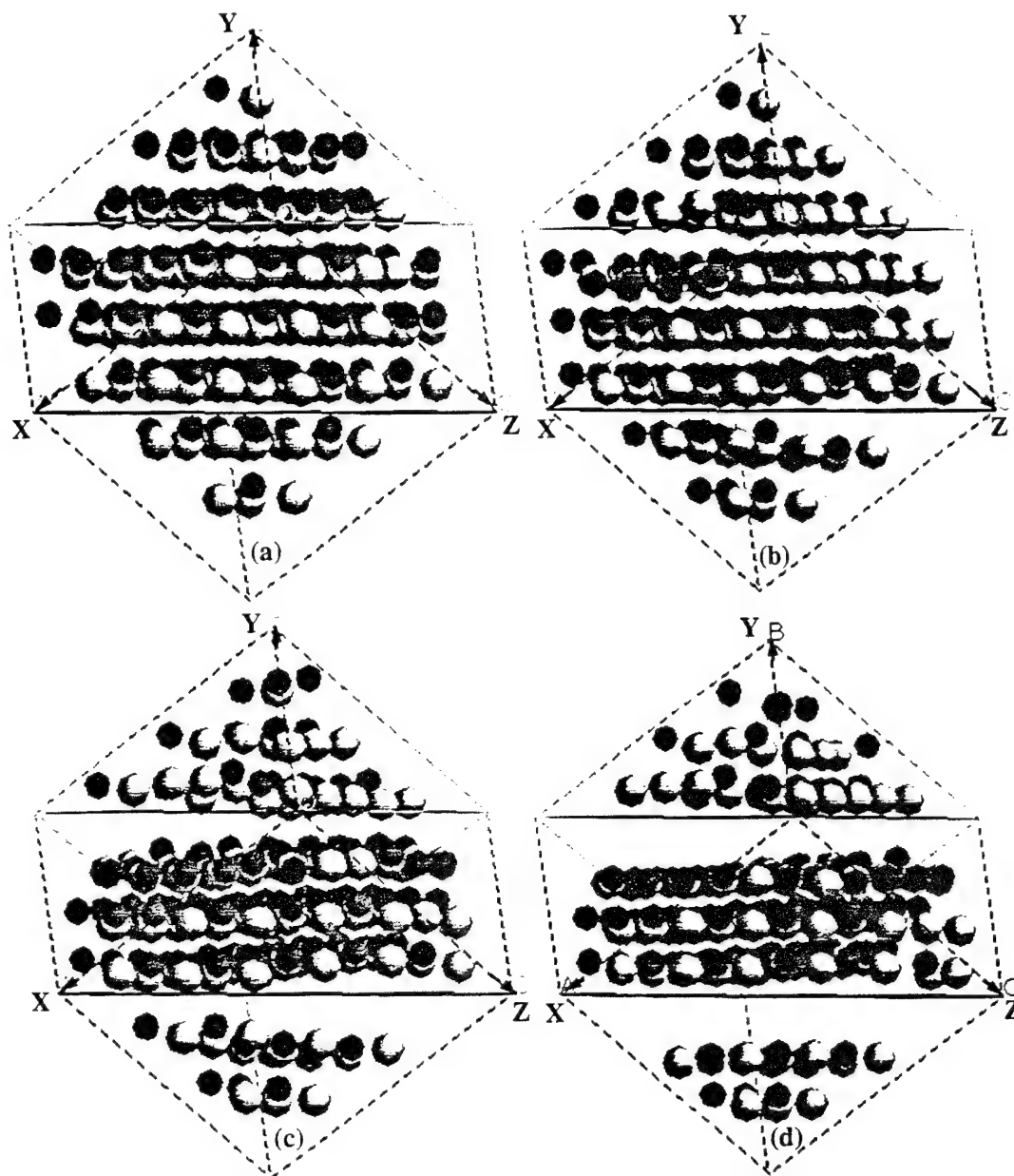
Fig. 2.9 View of simulation cell showing instantaneous atomic configurations at several instants during simulation at supercritical tension. C and Si atoms are shown as dark and light spheres, respectively. X, Y and Z are along [100], [010] and [001] respectively. Two solid lines in the middle are {1$\bar{1}$1} planes that are perpendicular to the plane to the paper. (a) at 0.3ps into the simulation (time step 2000) after applying a small step increase in tension, prior to the onset of instability; (b) at about 0.15pslater (time step 3000) when interplanar decohesion has occurred; (c) at about 0.06ps later (time step 3400) than (b) showing two well-defined crack propagations and indications of atomic relaxation on the crack surfaces; (d) at another 0.09ps later (time step 4000) showing two relatively clean cracks with relaxed surfaces.

78
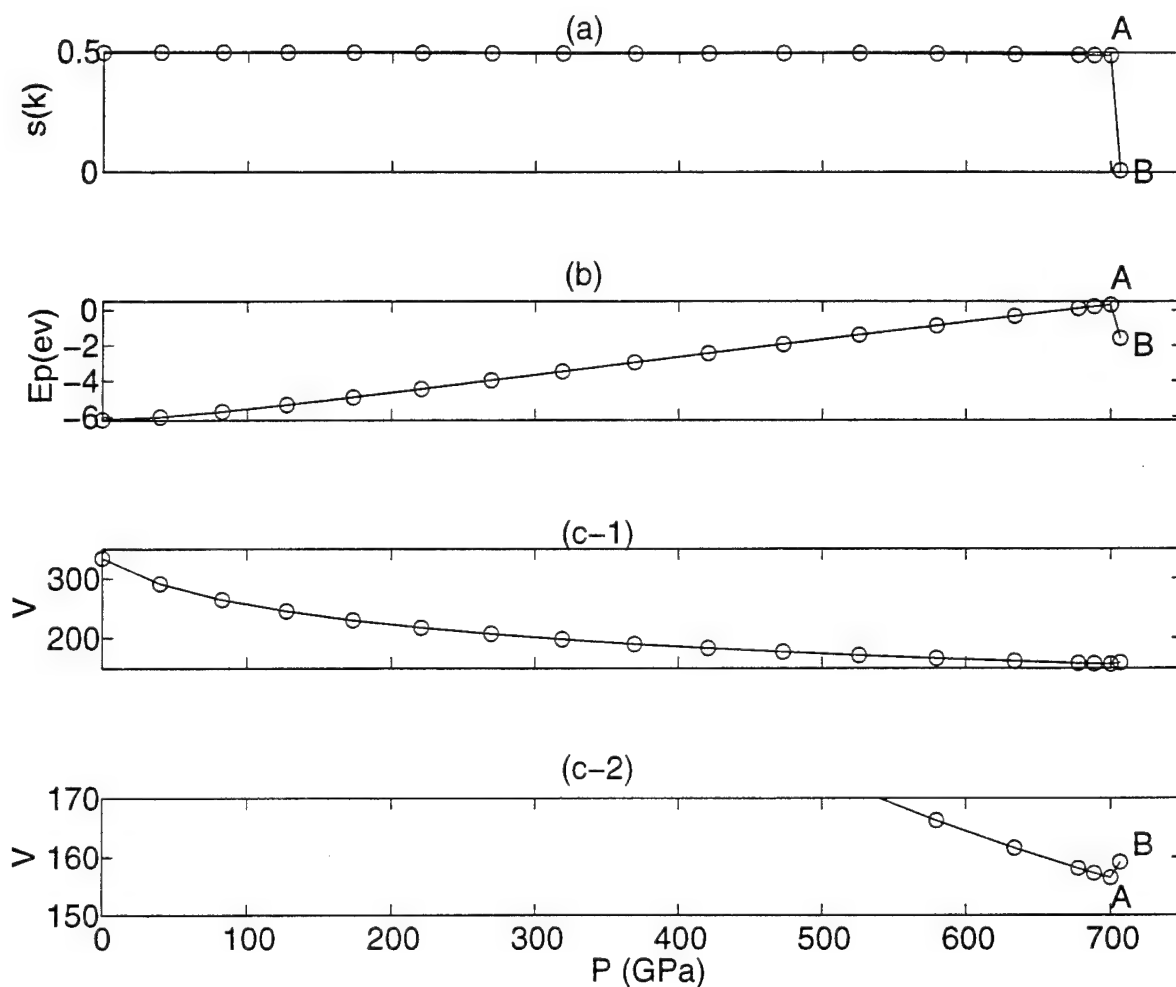
Fig. 2.10 System responses to compression. P is the internal pressure at each equilibrium state. From top to bottom, (a) structure factor $s(k)$, (b) potential energy per atom Ep (ev), (c-1) volume V in units of 6.538 Å^3, and (c-2) same as (c-1) except that data are shown in a scale that allows one to see clearly the volume increase of the last point in the plot.
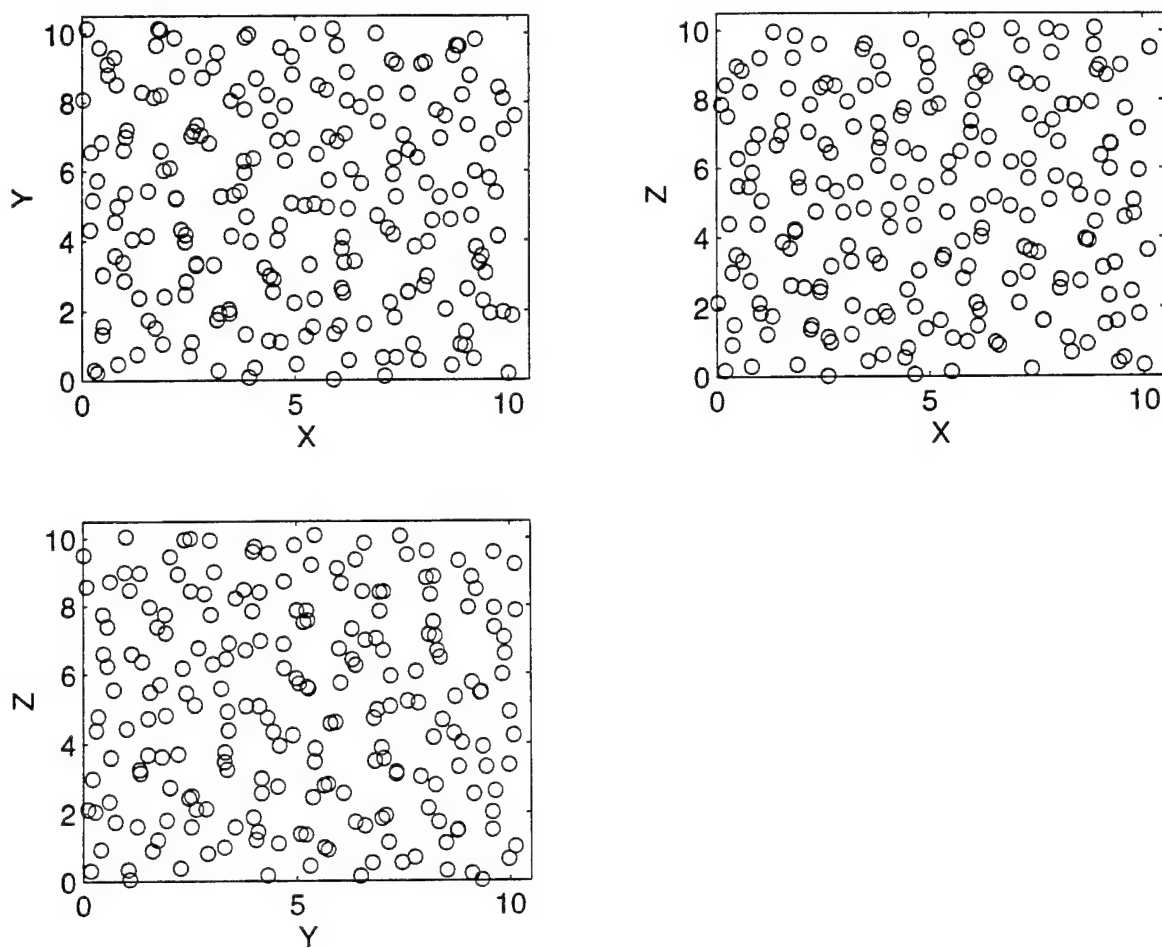
Fig. 2.11 Projections of the atomic configuration of SiC after amorphization.
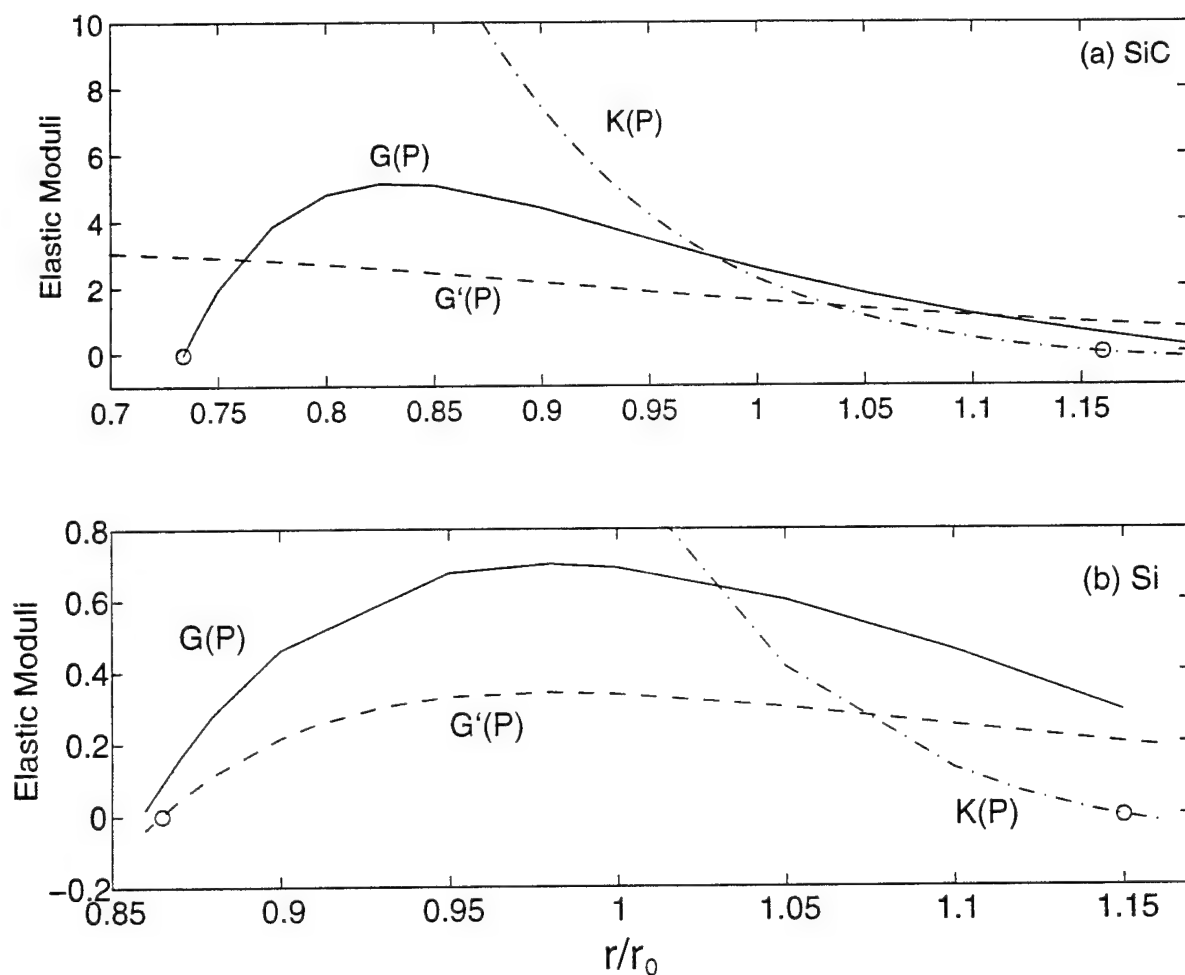
Fig. 2.12 Variations of elastic moduli (in units of $Mbar$) with hydrostatic pressure in SiC (a) and Si (b) at $0K$, r and r_0 denote lattice parameters at current and zero pressure respectively. Small circles denote the triggering instability for hydrostatic compression and tension.
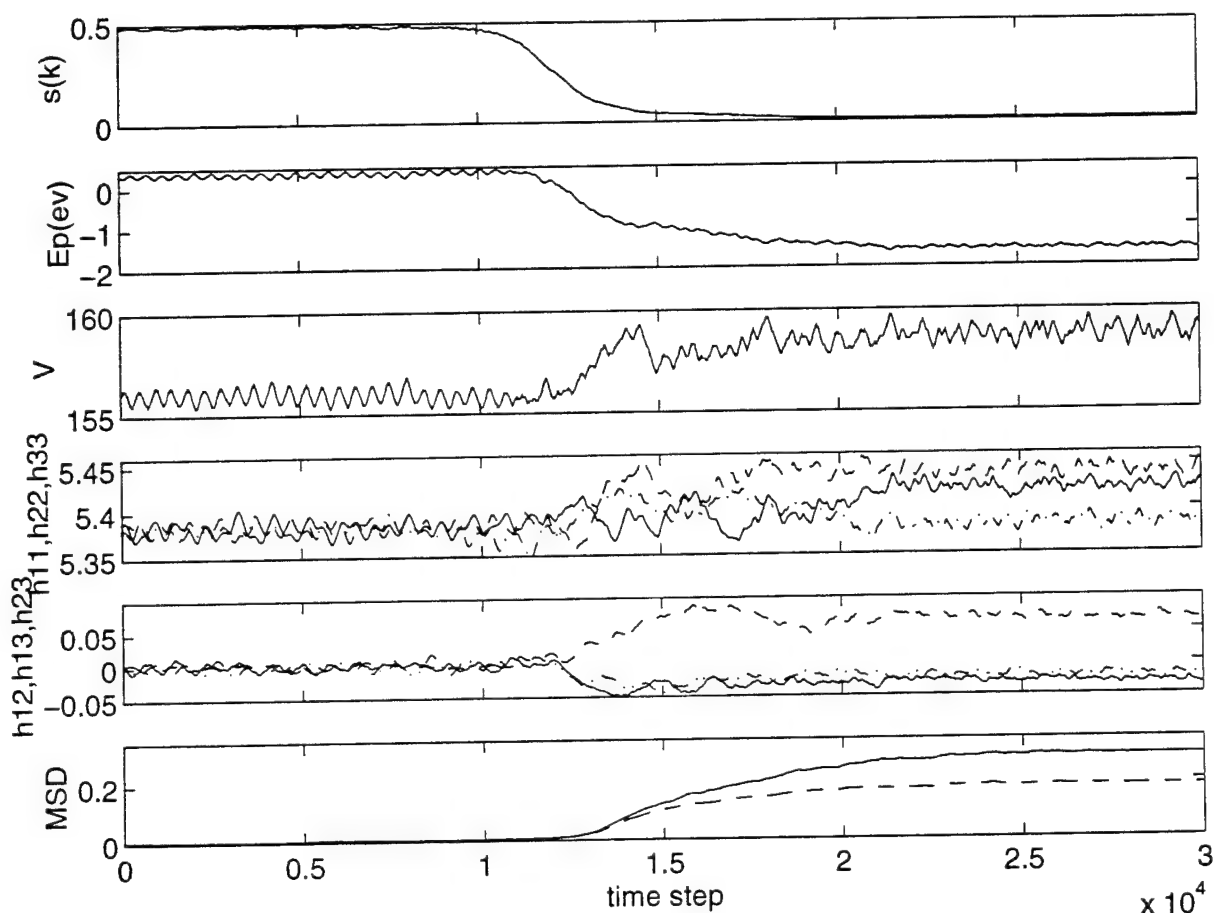
Fig. 2.13 Time-dependent system responses at the critical transition pressure. From top to bottom, (a) structure factor $s(k)$; (b) internal energy per atom Ep (ev); (c) volume in units of 6.538 Å^3; (d) diagonal elements of cell matrix h; (e) off-diagonal elements of matrix h; and (f) mean square displacements of Si (dashed line) and C (solid line) atoms. All lengths are in unit of 1.87 Å.

Appendix B: fluctuation formula of elastic constants

Here we present the fluctuation formula of elastic constants C_{11}, C_{12} and C_{44} using the Tersoff potential.

For cubic system, it is easy to obtain the general form for any potential functions

$$
\begin{aligned}
C_{\alpha\beta\gamma\epsilon} = \frac{l_0}{l} \cdot [&-\frac{V}{k_B T} \cdot \delta(\sigma_{\alpha\beta}\sigma_{\gamma\epsilon}) + \frac{2Nk_B T}{V} \cdot (\delta_{\alpha\epsilon}\delta_{\beta\gamma} + \delta_{\alpha\gamma}\delta_{\beta\epsilon}) \\
&+ < \frac{1}{V} \sum_{i<j}\sum_{k<l} [\frac{\partial^2 U}{\partial r_{ij}\partial r_{kl}} - \frac{\partial U}{\partial r_{ij}} \cdot \frac{\delta_{ik}\delta_{jl}}{r_{ij}}] \frac{r_{ij\alpha}r_{ij\beta}r_{kl\gamma}r_{kl\epsilon}}{r_{ij}r_{kl}} >] \\
= \frac{l_0}{l} \cdot [&C^k_{\alpha\beta\gamma\epsilon} + C^f_{\alpha\beta\gamma\epsilon} + C^B_{\alpha\beta\gamma\epsilon}]
\end{aligned} \tag{B1}
$$

where bracket $<>$ represents the ensemble average; $\delta_{\alpha\epsilon}$'s are the Kronecker functions and $\delta(AB) = <AB> - <A><B>$. The notations used are the following: i,j,k,l label the atoms; $\alpha,\beta,\gamma,\epsilon$ stands for x,y,z; $r_{ij\alpha} = r_{j\alpha} - r_{i\alpha}$, $x_{ij} = x_j - x_i$. The calculation of the kinetic term $C^k_{\alpha\beta\gamma\epsilon}$ and the fluctuation term $C^f_{\alpha\beta\gamma\epsilon}$ are straightforward. For the Tersoff potential, the Born term $C^B_{\alpha\beta\gamma\epsilon}$ is non-trivial and we present the formula here. Only major intermediate results during the derivation are given. More detailed derivation is given in the thesis.

From Eqn. (B1), we obtain

$$
\begin{aligned}
C^B_{\alpha\beta\gamma\epsilon} &= < \frac{1}{V} \sum_{i<j}\sum_{k<l} [\frac{\partial^2 U}{\partial r_{ij}\partial r_{kl}} - \frac{\partial U}{\partial r_{ij}} \cdot \frac{\delta_{ik}\delta_{jl}}{r_{ij}}] \frac{r_{ij\alpha}r_{ij\beta}r_{kl\gamma}r_{kl\epsilon}}{r_{ij}r_{kl}} > \\
&= < \frac{1}{V} \cdot \frac{1}{2} \sum_{i\neq j} [\frac{1}{2}\sum_{k\neq l} \frac{\partial^2 U}{\partial r_{ij}\partial r_{kl}} \cdot \frac{r_{ij\alpha}r_{ij\beta}r_{kl\gamma}r_{kl\epsilon}}{r_{ij}r_{kl}} - \frac{\partial U}{\partial r_{ij}} \cdot \frac{r_{ij\alpha}r_{ij\beta}r_{ij\gamma}r_{ij\epsilon}}{r_{ij}^3}] >
\end{aligned} \tag{B2}
$$

Since $U = \sum_{i\neq j} V_{ij}$, where V_{ij} is a function of r_{ij}, r_{ik} and r_{jk}, we work out the first and second derivatives $\frac{\partial U}{\partial r_{ij}}$ and $\frac{\partial^2 U}{\partial r_{ij}\partial r_{kl}}$ and obtain the following results

$$
\begin{aligned}
C^B_{\alpha\beta\gamma\epsilon} = \frac{1}{2} \sum_{i\neq j} \{ &\frac{\partial^2 V_{ij}}{\partial r_{ij}^2} \cdot \frac{r_{ij\alpha}r_{ij\beta}r_{ij\gamma}r_{ij\epsilon}}{r_{ij}^2} + \frac{\partial U}{\partial r_{ij}} \cdot \frac{r_{ij\alpha}r_{ij\beta}r_{ij\gamma}r_{ij\epsilon}}{r_{ij}^3} \\
&+ \sum_{k(\neq i,j)} [\frac{\partial^2 V_{ij}}{\partial r_{ik}^2} \cdot \frac{r_{ik\alpha}r_{ik\beta}r_{ik\gamma}r_{ik\epsilon}}{r_{ik}^2} + \frac{\partial^2 V_{ij}}{\partial r_{jk}^2} \cdot \frac{r_{jk\alpha}r_{jk\beta}r_{jk\gamma}r_{jk\epsilon}}{r_{jk}^2} \\
&+ \frac{\partial V_{ij}}{\partial r_{ik}} \cdot \frac{r_{ik\alpha}r_{ik\beta}r_{ik\gamma}r_{ik\epsilon}}{r_{ik}^3} + \frac{\partial V_{ij}}{\partial r_{jk}} \cdot \frac{r_{jk\alpha}r_{jk\beta}r_{jk\gamma}r_{jk\epsilon}}{r_{jk}^3}
\end{aligned}
$$

$$+\frac{\partial^2 V_{ij}}{\partial r_{ij}\partial r_{ik}}\cdot\frac{r_{ij\alpha}r_{ij\beta}r_{ik\gamma}r_{ik\epsilon}+r_{ik\alpha}r_{ik\beta}r_{ij\gamma}r_{ij\epsilon}}{r_{ij}r_{ik}}+\frac{\partial^2 V_{ij}}{\partial r_{ij}r_{jk}}\cdot\frac{r_{ij\alpha}r_{ij\beta}r_{jk\gamma}r_{jk\epsilon}+r_{jk\alpha}r_{jk\beta}r_{ij\gamma}r_{ij\epsilon}}{r_{ij}r_{jk}}$$

$$+\frac{\partial^2 V_{ij}}{\partial r_{ik}\partial r_{jk}}\cdot\frac{r_{ik\alpha}r_{ik\beta}r_{jk\gamma}r_{jk\epsilon}+r_{jk\alpha}r_{jk\beta}r_{ik\gamma}r_{ik\epsilon}}{r_{ik}r_{jk}}+\sum_{l\neq i,j,k}(\frac{\partial^2 V_{ij}}{\partial r_{ik}\partial r_{il}}\cdot\frac{r_{ik\alpha}r_{ik\beta}r_{il\gamma}r_{il\epsilon}}{r_{ik}r_{il}}$$

$$+\frac{\partial^2 V_{ij}}{\partial r_{jk}\partial r_{jl}}\cdot\frac{r_{jk\alpha}r_{jk\beta}r_{jl\gamma}r_{jl\epsilon}}{r_{jk}r_{jl}}+\frac{\partial^2 V_{ij}}{\partial r_{ik}\partial r_{jl}}\cdot\frac{r_{ik\alpha}r_{ik\beta}r_{jl\gamma}r_{jl\epsilon}+r_{jl\alpha}r_{jl\beta}r_{ik\gamma}r_{ik\epsilon}}{r_{ik}r_{jl}})]\}\qquad(B3)$$

If we use Voigt's notation, the elastic constants become

$$C_{11}=\frac{l_0}{l}\cdot[-\frac{V}{k_BT}\cdot\delta(\sigma_{xx}\sigma_{xx})+\frac{4Nk_BT}{V}+<\frac{1}{V}C_{11}^B>]\qquad(B4)$$

$$C_{12}=\frac{l_0}{l}\cdot[-\frac{V}{k_BT}\cdot\delta(\sigma_{xx}\sigma_{yy})+<\frac{1}{V}C_{12}^B>]\qquad(B5)$$

$$C_{44}=\frac{l_0}{l}\cdot[-\frac{V}{k_BT}\cdot\delta(\sigma_{yz}\sigma_{yz})+\frac{2Nk_BT}{V}+<\frac{1}{V}C_{44}^B>]\qquad(B6)$$

where

$$C_{11}^B=\frac{1}{2}\sum_{i\neq j}\{(\frac{\partial^2 V_{ij}}{\partial r_{ij}^2}-\frac{\partial V_{ij}}{\partial r_{ij}}\cdot\frac{1}{r_{ij}})\frac{x_{ij}^4}{r_{ij}^2}$$

$$+\sum_{k(\neq i,j)}[(\frac{\partial^2 V_{ij}}{\partial r_{ik}^2}-\frac{\partial V_{ij}}{\partial r_{ik}}\cdot\frac{1}{r_{ik}})\frac{x_{ik}^4}{r_{ik}^2}+(\frac{\partial^2 V_{ij}}{\partial r_{jk}^2}-\frac{\partial V_{ij}}{\partial r_{jk}}\cdot\frac{1}{r_{jk}})\frac{x_{jk}^4}{r_{jk}^2}+\frac{\partial^2 V_{ij}}{\partial r_{ij}\partial r_{ik}}\cdot\frac{x_{ij}^2 x_{ik}^2}{r_{ij}r_{ik}}$$

$$+\frac{\partial^2 V_{ij}}{\partial r_{ij}r_{jk}}\cdot\frac{x_{ij}^2 x_{jk}^2}{r_{ij}r_{jk}}+\frac{\partial^2 V_{ij}}{\partial r_{ik}\partial r_{jk}}\cdot\frac{2x_{ik}^2 x_{jk}^2}{r_{ik}r_{jk}}+\sum_{l\neq i,j,k}(\frac{\partial^2 V_{ij}}{\partial r_{ik}\partial r_{il}}\cdot\frac{x_{ik}^2 x_{il}^2}{r_{ik}r_{il}}$$

$$+\frac{\partial^2 V_{ij}}{\partial r_{jk}\partial r_{jl}}\cdot\frac{x_{jk}^2 x_{jl}^2}{r_{jk}r_{jl}}+\frac{\partial^2 V_{ij}}{\partial r_{ik}\partial r_{jl}}\cdot\frac{2x_{ik}^2 x_{jl}^2}{r_{ik}r_{jl}})]\}\qquad(B7)$$

$$C_{12}^B=\frac{1}{2}\sum_{i\neq j}\{(\frac{\partial^2 V_{ij}}{\partial r_{ij}^2}-\frac{\partial V_{ij}}{\partial r_{ij}}\cdot\frac{1}{r_{ij}})\frac{x_{ij}^2 y_{ij}^2}{r_{ij}^2}$$

$$+\sum_{k(\neq i,j)}[(\frac{\partial^2 V_{ij}}{\partial r_{ik}^2}-\frac{\partial V_{ij}}{\partial r_{ik}}\cdot\frac{1}{r_{ik}})\frac{x_{ik}^2 y_{ik}^2}{r_{ik}^2}+(\frac{\partial^2 V_{ij}}{\partial r_{jk}^2}-\frac{\partial V_{ij}}{\partial r_{jk}}\cdot\frac{1}{r_{jk}})\frac{x_{jk}^2 y_{jk}^2}{r_{jk}^2}+\frac{\partial^2 V_{ij}}{\partial r_{ij}\partial r_{ik}}\cdot\frac{x_{ij}^2 y_{ik}^2}{r_{ij}r_{ik}}$$

$$+\frac{\partial^2 V_{ij}}{\partial r_{ij}r_{jk}}\cdot\frac{x_{ij}^2 y_{jk}^2}{r_{ij}r_{jk}}+\frac{\partial^2 V_{ij}}{\partial r_{ik}\partial r_{jk}}\cdot\frac{(x_{ik}^2 y_{jk}^2+x_{jk}^2 y_{ik}^2)}{r_{ik}r_{jk}}+\sum_{l(\neq i,j,k)}(\frac{\partial^2 V_{ij}}{\partial r_{ik}\partial r_{il}}\cdot\frac{x_{ik}^2 y_{il}^2}{r_{ik}r_{il}}$$

$$+\frac{\partial^2 V_{ij}}{\partial r_{jk}\partial r_{jl}}\cdot\frac{x_{jk}^2 y_{jl}^2}{r_{jk}r_{jl}}+\frac{\partial^2 V_{ij}}{\partial r_{ik}\partial r_{jl}}\cdot\frac{x_{ik}^2 y_{jl}^2+x_{jl}^2 y_{ik}^2}{r_{ik}r_{jl}})]\}\qquad(B8)$$

$$C_{44}^B=\frac{1}{2}\sum_{i\neq j}\{(\frac{\partial^2 V_{ij}}{\partial r_{ij}^2}-\frac{\partial V_{ij}}{\partial r_{ij}}\cdot\frac{1}{r_{ij}})\frac{x_{ij}^2 y_{ij}^2}{r_{ij}^2}$$

$$+\sum_{k(\neq i,j)}[(\frac{\partial^2 V_{ij}}{\partial r_{ik}^2}-\frac{\partial V_{ij}}{\partial r_{ik}}\cdot\frac{1}{r_{ik}})\frac{x_{ik}^2 y_{ik}^2}{r_{ik}^2}+(\frac{\partial^2 V_{ij}}{\partial r_{jk}^2}-\frac{\partial V_{ij}}{\partial r_{jk}}\cdot\frac{1}{r_{jk}})\frac{x_{jk}^2 y_{jk}^2}{r_{jk}^2}+\frac{\partial^2 V_{ij}}{\partial r_{ij}\partial r_{ik}}\cdot\frac{x_{ij}y_{ij}x_{ik}y_{ik}}{r_{ij}r_{ik}}$$

$$+ \frac{\partial^2 V_{ij}}{\partial r_{ij} r_{jk}} \cdot \frac{x_{ij} y_{ij} x_{jk} y_{jk}}{r_{ij} r_{jk}} + \frac{\partial^2 V_{ij}}{\partial r_{ik} \partial r_{jk}} \cdot \frac{2 x_{ik} y_{ik} x_{jk} y_{jk}}{r_{ik} r_{jk}} + \sum_{l(\neq i,j,k)} \left(\frac{\partial^2 V_{ij}}{\partial r_{ik} \partial r_{il}} \cdot \frac{x_{ik} y_{ik} x_{il} y_{il}}{r_{ik} r_{il}} \right.$$

$$+ \frac{\partial^2 V_{ij}}{\partial r_{jk} \partial r_{jl}} \cdot \frac{x_{jk} y_{jk} x_{jl} y_{jl}}{r_{jk} r_{jl}} + \frac{\partial^2 V_{ij}}{\partial r_{ik} \partial r_{jl}} \cdot \frac{2 x_{ik} y_{ik} x_{jl} y_{jl}}{r_{ik} r_{jl}} \Big)]\} \qquad (B9)$$

Chapter 3. Experimental Study of Interface Strength[*]

3.1 Summary

The fracture toughness of fiber reinforced composites may be optimized without unwarranted loss of transverse strength through control of interface strength between reinforcing material and matrix. These design considerations, including limits on the permissible interface strengths, have been delineated by others. This present work examines the effect of carbon interlayers on the tensile strength of flat interface couples representing the interface between fiber and its coating. Polished single crystal sapphire wafers, 1.0 inch in dameter and 0.5 mm thick, were substituted for the fiber; relatively thick, 2 μm, SiC coatings are substituted for the thin coatings used in composite materials; and 200 nm carbon layers, being the weakest material present, act as mechanical fuses to control the overall strength of the entire system.

As the SiC coatings had to be relatively thick, homogeneous, and nearly stress-free, a study of the deposition of SiC by plasma enhanced chemical vapor deposition (PECVD) was conducted. Coatings with a nearly zero residual stress were deposited at 275 C, 50 μm pressure and 30 watts applied power with the lower electrode self-biased at +3 volts. Uniform deposition was insured through the use of hydrogen as a dilution gas.

The carbon interlayers processed by PECVD at 400 C deposited on sapphire were found by high resolution TEM to be amorphous or microcrystalline depending on the applied rf power. Carbon deposited on microcrystalline SiC by low pressure CVD between 1100 and 1500 C were determined by x-ray diffraction to be highly oriented in structure with the degree of preferred orientation increasing from a Bacon Anisotropy Factor of 4.5 for material deposited on SiC at 1100 C to 6.8 for material deposited at 1500 C.

Strength of the SiC/C/sapphire couples was determined through a technique called

laser spallation whereby a laser is pulsed onto a thin absorbing layer on the reverse side of the substrate; the laser impact creates a shock wave which propagates through the substrate, gets reflected from the front surface where it is converted into a tension wave, and, if of sufficient intensity, causes delamination of the film. This phenomena itself is investigated using a high speed digitizer to examine shock wave propagation through piezo-electric quartz and is also modeled with finite element techniques.

The tensile strength of the sapphire/SiC interface was found to be 14.7 MPa for LPCVD SiC and 10.0 MPa for PECVD SiC. Couples with amorphous carbon interlayers had a strength of 2.0 MPa. The strength of interface couples with highly oriented carbon interlayers scaled with the carbon processing temperature.

3.2 The Design of Interfaces

It has become quite apparent that success in controling the strength and toughness of inorganic composites rest upon the control of the interfaces in these materials. The most desired result of interface control is to achieve composite toughnening through the deflection of cracks propagating through the matrix. If these cracks can be deflected at the fiber/matrix or fiber/coating interface, the fibers may still carry longitudinal loads, the crack energy may be consumed through delamination and fiber pull-out, and complete failure may be delayed. This has been described as toughening through interface delamination, crack bridging, and frictional pull-out [1]. This phenomenon has been successfully demonstrated in ceramic composite systems [2-4].

Material requirements for crack deflection at a composite interface while maintaining maximum transverse strength have been mathematically delineated, and the maximum interface strengths for SiC coatings on carbon pitch fibers and on sapphire fibers have been calculated [5,6]. The results are presented in Table 3.1.

The purpose of the present work was to process the model interfaces and to test their transverse strength. The results on interface strength are compared with the theoretical predictions. Carbon coatings have been used as interlayers in flat model test

couples (shown schematically in Fig. 3.1) in order to achieve interface strengths for actual fiber/coating systems predicted by the design considerations.

3.3 Processing of Silicon Carbide

Silicon carbide coatings have been prepared by using plasma enhanced CVD reactor system which was designed and constructed at MIT [8]. The processing parameters are shown in Table 3.2. Typical deposition rates ranged from 10 to 30 nm per minute.

3.3.1 SiC Process Development

The SiC process development included uniformity of deposition, suppression of particle formation during deposition and residual stresses in coatings.

Uniform deposition for parallel plate PECVD reactor was achieved by balancing several factors which determine reaction rates including residence time, reactant concentration, and electron density.

A seroius problem was solved in the course of this work involving the formation of sub-micron size particles in the plasma. These particles would embed themselves in the growing film and act as stress concentrators during laser spallation so that fracture would take place within the coating rather than at the coating/substrate interface. It has been demonstrated that suppression of particle growth required the use of hydrogen as a carrier gas with the silane gas concentration not more than 10 percent. In addition, the supplied power must be below 100 watts with the pressure below 50 µm. At the same time, this low gas pressure and power insured thickness uniformity better than 5 percent across the electrode surface.

Stresses in SiC films produced by PECVD were found to vary over a great range from highly compressive to highly tensile, depending on processing parameters. Sources of stress in coatings are a mismatch in the CTD between the substrate and the coating, pinning effect and incorporation of hydrogen in the growing film. Substrate temperature during processing is one of the most important parameters affecting stress in coatings, compressive at lower temperatures, becoming linearly more tensile with increasing substrate temperature with a crossover temperature at which stress in

the coating changes from compressive to tensile. The substrate temperature mainly affects the stress due to incorporation of hydrogen into the growing film. The desorption rate of hydrogen from the surface is influenced by the temperature and also by ion bombardment. The stress in coatings has been also manipulated through post-deposition anneals, by supplying energy to release hydrogen from the film. Stress may change from highly compressive to highly tensile and has been contributed to a diffusion controlled volume change in material.

3.3.2 Residual Stress Measurement

Stress states in coatings have been determined by measuring the deflection of substrate material due to presence of a deposited coatings. Silicon wafers were typically used as a substrate. Using a profilometer in conjunction with an interferometer was found to be the optimum method in determining deflections of coated and uncoated wafers. Wafers were first sorted with the interferometer; only those of nearly uniform convex or concave shape were chosen for profilometry. The dependence of stress on substrate temperature and electrode voltage is shown in Fig. 3.2. The as-deposited stress as a function of substrate temperature becomes more tensile for films deposited on floating electrode and becomes more compressive for films deposited on a grounded electrode. The only difference between these two processes is that floating electrode self-biases to +2 volts, while the grounded electrode is a 0 volts. It can be seen in Fig. 3.2 that amorphous SiC coatings can be processed by PECVD to a thickness of 2 μm with a stress that is less than 13 MPa at 275 C on a positively biased electrode.

The effect of annealing is shown in Fig. 3.3 and can be explained in terms of hydrogen diffusion out of the film followed by thermally activated rearrangement of the structure. In all cases the stresses become highly tensile upon annealing at the lowest of the anneal temperatures, 650 C. This temperature allowed complete diffusion of hydrogen out of the submicron film in one hour. In subsequent anneals at higher temperatures the coatings relaxed. Thus annealing process is composed of two steps: a diffusion controlled process whereby the film stretched due to hydrogen escape followed by a thermally activated relaxation of the structure. As shown in Fig. 3.3, it

was not possible to prodoce the relatively thick, low stress coatings through a deposition/annealing process as the diffusion of hydrogen out of the coatings before relaxationalways produced sufficient tensile stress to cause film delamination.

3.4 Processing of Carbon

Carbon interlayers for model test couples have been processed by using plasma enhanced chemical vapor deposition (PECVD) and low pressure chemical vapor deposition (LPCVD).

3.4.1 PECVD of Carbon

The PECVD carbon processing parameters are shown in Table 3.3. Two sets of processing parameters were chosen such that amorphous and graphitic carbon might be produced. The only difference between the "grounded" and "powered" carbon is the power supplied to the plasma. For the first type, the lower electrode is grounded during deposition while for the second type the lower electrode is powered creating approx. -100 V bias. The objective in choosing the above parameters was to create sufficient bombardment during deposition for the powered carbon so that it would be graphitized, while the grounded would be amorphous and diamond-like. Instead of expected amorphous and graphitized carbon films, amorphous and microcrystalline films were produced by PECVD, to be used as interlayers for interface test couples. It is for this reason that processing of carbon by LPCVD was initiated.

3.4.2 LPCVD of Carbon

The LPCVD apparatus was designed and constructed in the present work to attach to the PECVD reactor in such a way as to share gas flow controllers and pumping system. This is shown schematically in Fig. 3.4. Carbon coatings were deposited between 1100 and 1400 C at 200 mtorr pressure.

The carbon coatings deposited on SiC were studied by X-ray diffraction and their density was measured by a sink-float technique. Table 3.4 lists Bacon Anisotropy Factor, crystallite size, peak position and density for carbon deposited at 1100, 1200, 1300 and 1400 C. It was determined that the degree of preferred orientation in the

coating, average crystallite size, and coating density all increased with deposition temperature while the lattice parameter remained constant. The increased deposition temperature produced a more oriented, denser deposite. The results obtained in the present work show opposite trends when compared to the data reported in the literature [9]. This is shown in Fig. 3.5 where anysotropy factor, average crystallite size and density decrease with increasing deposition temperature. The difference between the results in the present work and that of previous workers may be explained by a difference in rates of nucleation at the surface. At the lower temperatures deposition in the past work has been controlled by the kinetics of radical attachment at the film surface while at the higher temperatures radical attachment to existing nuclei is overhelmed by the creation of new crystallites. As the nucleation rate increases with temperature the average crystallite size decreases and the decrease in density is associated with the increase in porosity. In the present work the reduced processing pressure suppresses nucleation events favoring radical attachement to existing crystallites. As the process temperature is increased, radicals have evenmore surface mobility allowing formation of larger and more dense crystallites.

3.5 Mechanical Evaluation of Couples by Laser Spallation

3.5.1 Laser Spallation Technique

With this technique a short laser pulse induces an elastic shock wave in a substrate which propagates as a relatively short stress pulse. If this stress pulse is of sufficient intensity, a solid film may be spalled from the opposite surface of the substrate when the compression wave turns into a tension wave upon reflection from the free surface. Knowledge of the threshold stress pulse intensity at which coating delamination occures allows determination of the bimaterial interface strength. This type of interface test is particularly valuable as shock wave loading provides stresses propagating with the speed of sound in the substrate material and can theoretically produce fracture by the collective separation of atomic bonds rather than through crack initiation and propagation as during fracture caused by any other, relatively slow,

loading.

The development of the laser spallation experiment consists of two parts. The first step requires measurement of the induced shock wave peak intensity as a function of laser fluence used to generate the shock wave. The typical spatial and temporal profiles of the generated stress pulse are also determined. The second part concerns the mathematical calculation of the propagation and reflection of the experimentally determined shock wave. The functional dependence of the stress probing the bimaterial interface upon the laser fluence is calculated. Therefore, the results from the first part of development, coupled with performed calculations, have led to a relation between the threshold laser fluence for delamination and the stresses which were developed at the bimaterial interface.

3.5.2 Experimental Details

The set-up is shown schematically in Fig. 3.6. The test specimen consists of a substrate coated with a test material on one side and a laser absorbing film on its side facing laser. In this work the absorbing film is 1.0 μm thick tin deposited by rf sputtering, the substrate was either sapphire or quartz, and the coating was SiC deposited as discussed previously. The coated substrate is pressed against a polished, fused quartz disc that is transparent to light and is used to confine the expansion of the laser absorbing film. A pulse of light is emmited from the laser and is focused onto the absorbing film on the reverse of the substrate. The film is rapidly heated upon absorbing the flux of laser energy, melts, and even evaporates, causing a compressive, elastic wave to propagate forward into the substrate bearing the coating and also backwards into the confining focused quartz disk. The focused quartz disc confines the expansion of the melting and evaporating layer leading to a sharper stress pulse. The compressive pulse travels through the substrate, bimaterial substate-coating interface, and then the coating. This compressive pressure pulse reflects from the coating free surface, becomes a tensile pressure pulse, and then loads the bimaterial interface in tension. It is necessary that both materials of the substrate and the coating are non-dissipative, and brittle, with their strength in tension being much lower than their strength in compression. The same must be also

true of their interface. It is assumed that the interface is of lower strength than either individual material. The interface strength is determined by relating the threshold laser fluence that causes film delamination to the shock wave intensity at the interface. Fig.3. 7 contains two micrographs of the delamination of 2.0 μm thick SiC coatings from a polished sapphire substrate. The secondary delamination in Fig. 3.7 is due to residual stress in the coating.

The laser was set to a pulse mode at 10 Hz and the energy was measured on the full beam diameter with Scientech[FM] 365 power meter with a Scientech[TM] 3800101 silicon head calibrated at 1.06 μm wavelength. These instruments measured the average energy over 10 shots, or over a one second time interval. The energy was recorded and the laser control was switched to the individual pulse mode. The power was removed from the beam path and a pulse of energy was released into the specimen. The specimen was examined to see if spallation had occured. The process was repeated until the lowest energy at which delamination occured was determined. This concluded the test of the interface strength.

3.5.3 Results on Sapphire/Carbon/SiC Couples

The test couple is shown schematically in Fig. 3.1. The SiC was processed as described in Section 3.3, and carbon layers, if present, were processed as described in Section 3.4. Tensile strengths for various couples with and without carbon interlayers are presented in a bar graph form in Fig. 3.8.

It is clear that carbon interlayers reduce the strength of the interface couple by an order of magnitude from roughly 10 to 15 MPa to 0.5 to 2.0 MPa. It should also be noted that the SiC deposited by low pressure CVD had an interface strength 50 percent greater than the SiC deposited by plasma enhanced CVD. The material deposited at low pressure by thermal deposition would not contain hydrogen and, therefore, would make more covalent bonds with the surface.

Of the couples with carbon interlayers those containing "powered" or amorphous carbon were the strongest at 2.0 MPa and those containing pyrolytic carbon interlayers were the weakest approaching 0.5 MPa. The couples containing "grounded", or

microcrystalline, carbon interlayers had a strength of 1.25 MPa and were weaker than those containing pyrolytic carbon.

Tensile strengths of model couples versus deposition temperature during processing of the carbon interlayer are shown in Fig. 3.9. Couple tensile strength decreases linearly with increasing deposition temperature, that is, with increasing anysotropy factor, crystallite size and density of carbon.

Fig. 3.10 shows the strength of the couples versus the structure data obtained with the same processing data, but with SiC substrates instead of sapphire substrates. The couple strengths are plotted versus Bacon Anisotropy Factor, crystallite size, and density. The couple tensile strength would then increase with increasing anysotropy factor, crystallite size, and density. However, the relationship between strength and orientation seems to be proportional. It is interesting that strength might increase with density. This implies that the decrease in strength is not due to an increase in porosity, that less porous films lead to weaker couples. That couple strength would decrease with an increase in average crystallite size implies that strength decreases with a decrease in grain boundary area. It is therefore suggested that the separation between the planes inside each crystallite consumes a very small amount of fracture energy and that most of the energy is consumed between crystallites during the rupture of the nearly amorphous grain boundaries and in changing crack direction between one crystallite and the next. Therefore, if the deposition of carbon on sapphire and SiC are similar, it seems that the strength of the couples most reasonably scales with orientation over a broad, intermediate range of Bacon Anisotropy Factors.

Comparison of couple tensile strengths shown in Fig. 3.8 and the maximum allowable interface strengths for interface delamination (see Table 3.1) allowed the conclusion that all test couples produced had tensile strengths significantly less than those prescribed by the theory to maximize composite transverse strength while maintaining composite toughening through controlled interface delamination.

3.6 Conclusions and Recommendation

94

A method to test the strength of an interface between a coating and a substrate by way of laser induced shock waves has been developed.

This technique has been applied to evaluate model couples in inorganic matrix composites and to compare the results with those prescribed by the theory to maximize composite transverse strength while maintaining composite toughening through controlled interface delamination. Test couples consisted of silicon carbide and sapphire, with or without carbon interlayers.

Processing of silicon carbide by PECVD has been optimized to prepare relatively thick, homogeneous and uniform coatings which were nearly stress-free.

Pyrolytic carbon films were prepared by LPCVD to be used as interlayers for interface test couples. Carbon films with different structure parameters (i.e., anysotropy factor and crystallite size) and density have been produced by varying deposition temperature.

It has been demonstrated that interfaces with strengths ranging over an order of magnitude may be synthesized through thin film processing. However, all of the test couples produced had tensile strengths significantly less than those prescribed by theory.

It is suggested that, in the future work, two directions may be fruitful to the attainment of optimized interfaces desired for composite materials. First, other materials with strengths greater than those of microcrystalline carbon should be considered and studied as interlayers for composites. Boron nitride is a possibility, and it has been shown to vary in degree of preferred orientation depending on processing. Another approach to optimized interfaces would be to deposit small elemental layers of an embrittling substance which would then alter fracture toughness rather than tensile strength. Precipitates grown by overaging in aluminum matrix composites have been shown to enhance fracture toughness this way [10].

3.7 References

[1] A.S. Argon, V. Gupta, H.S. Landis, and J.A.Cornie: Materials Science and Engineering, 1989, vol. A107, pp. 41-47.

[2] J.A.Cornie, A.S. Argon, and V.Gupta: MRS Bulletin, 1991, vol.16, pp.32-38.

[3] D.H. Grande, J.F. Mandell, and K.C.C. Hong: Journal Materials Science, 1988, vol.23,, pp.311-328.

[4] C. Pothieu, M. Lancin, and J. Thibault-Desseaux: Philosophical Magazine A, 1990, vol.62, pp.605-615.

[5] V. Gupta, A.S. Argon, and Z. Suo: Journal of Applied Mechanics, 1992, vol.59, pp.S79-S86.

[6] V. Gupta, J. Yuan, and D. Martinez: Journal of American Ceramic Society, 1993, vol.76, pp.305-315.

[7] Engineering Property Data on Selected Ceramics, Battelle, Columbus Laboratories, July,1981, MCIC-HB-07.

[8] H. Landis, Ph.D. Thesis, MIT, Dept. Mater. Sci. & Eng., 1988.

[9] J.C. Bokros: in Chemistry and Physics of Carbon, P.L.J. Walker, eds., Marcel Dekker, Inc., New York, 1969, pp.1-118.

[10] J.A. Cornie, M. Seleznev, M. Ralph, and F. Armatis: Materials Science and Engineering A, 1993, vol.162,pp.135-142.

Appendix: tables and figures

Table 3.1 Maximum Allowable Interface Strengths for Interface Delamination.

Fiber	Fiber Modulus (GPa)	Fiber Strength (GPa)	Coating	Coating Modulus (GPa)	Maximum Allowable Strength (MPa)
Carbon Pitch-55 [5]	E_{11}, 380 E_{22}, 13	2.12	SiC	448	95
Sapphire [7]	400	2.5	SiC	448	825

Table 3.2 PECVD Processing Parameters for the Deposition of SiC.

Parameters	Cleaning	Deposition
Time	15 min	3 hours
Temperature	300 C	275 C
Pressure	100 µm	50 µm
Gas Flow: SiH_4 CH_4 Ar H_2	20.0 sccm 20.0 sccm	1.8 sccm 2.9 sccm
Upper Electrode: Incident Power DC Voltage RF Voltage	100 watts -450 -560	25 watts -350 -240
Lower Electrode: Incident Power DC Voltage RF Voltage	floating +8 -22	floating +3 -12

Table 3.3 PECVD Processing Parameters for the Deposition of Carbon.

Processing Parameters	"Grounded" Carbon	"Powered" Carbon
Substrate Temperature	400 C	400 C
Pressure	50 μm	50 μm
Methane Flow Rate	5.0 sccm	5.0 sccm
Upper Electrode	30 watts	100 watts
Lower Electrode	grounded	30 watts

Table 3.4 Properties of Pyrolytic Carbon Deposited by the LPCVD Process.

Deposition Temperature (C)	Anisotropy Factor	Crystallite Size (nm)	Lattice Parameter (nm)	Density (gm/cm^3)
1100	4.5	4.6	0.3514	1.70
1200	5.5	4.8	0.3514	1.68
1300	6.2	5.3	0/3520	1.85
1400	6.6	7.9	0.3514	1.90
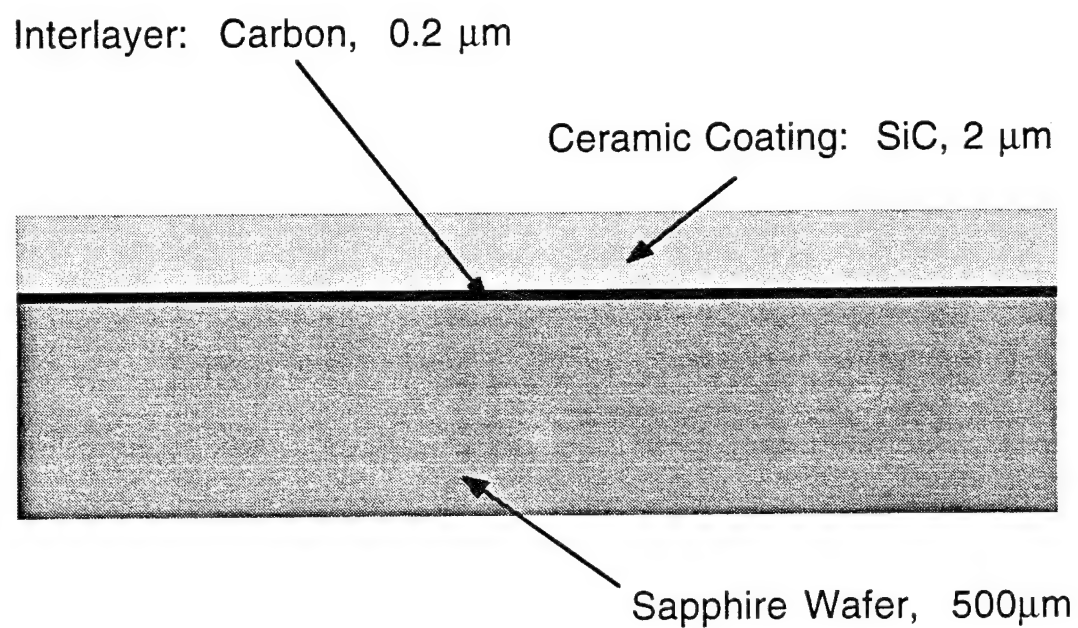
Fig. 3.1 Schematic representation of the model interface test specimens.

Coating Stress as a Function of Deposition Temperature
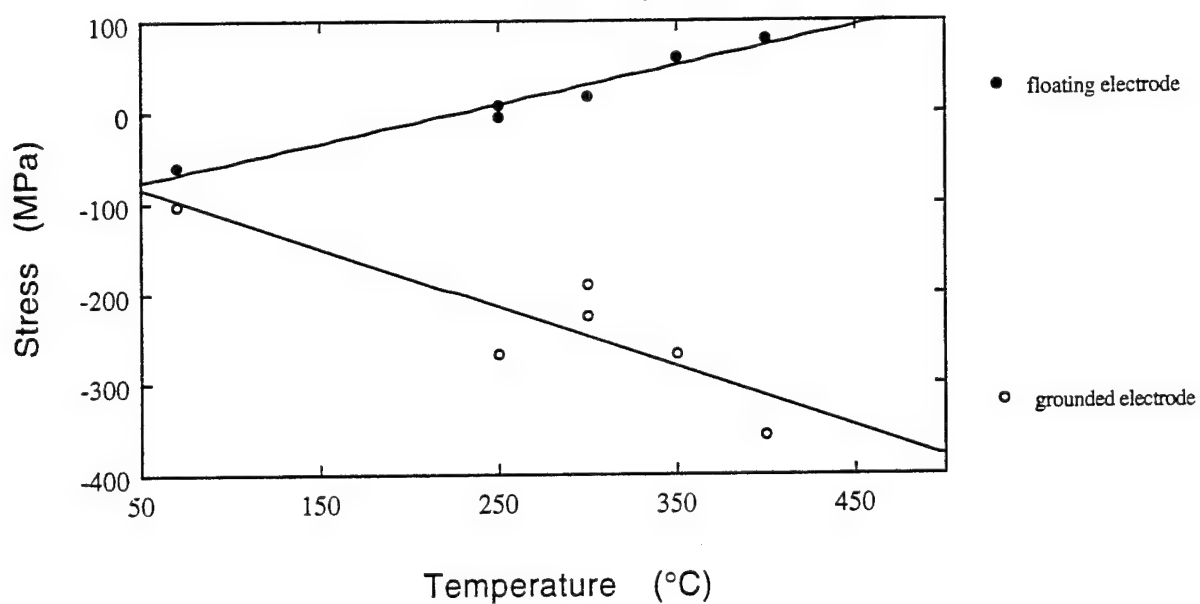
Fig. 3.2 As-deposited stress as a function of substrate temperature for grounded and floating lower electrodes.

Stress vs. Anneal Temperature for a Grounded Electrode
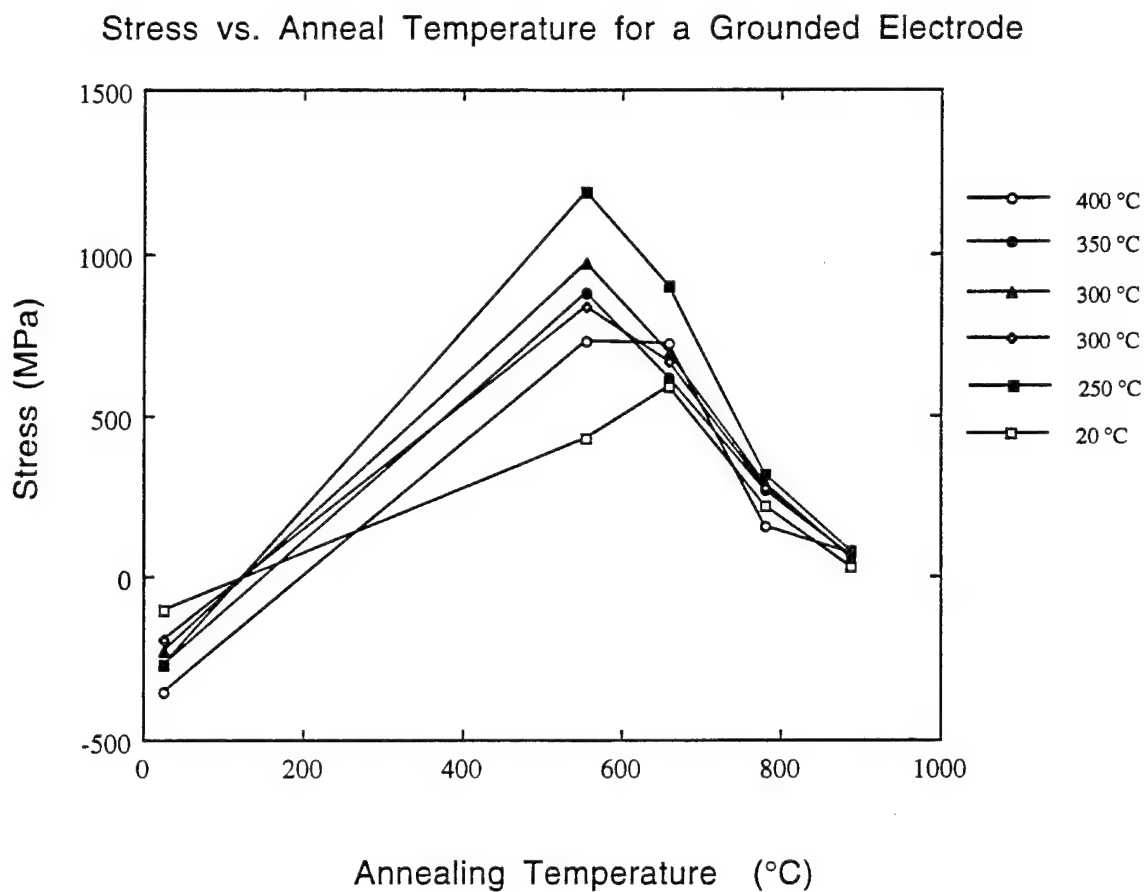
Fig. 3.3 Stress in the coatings deposited on a grounded electrode at 20, 250, 300, 350, and 400 °C as a function of annealing temperature for consecutive one hour anneals.
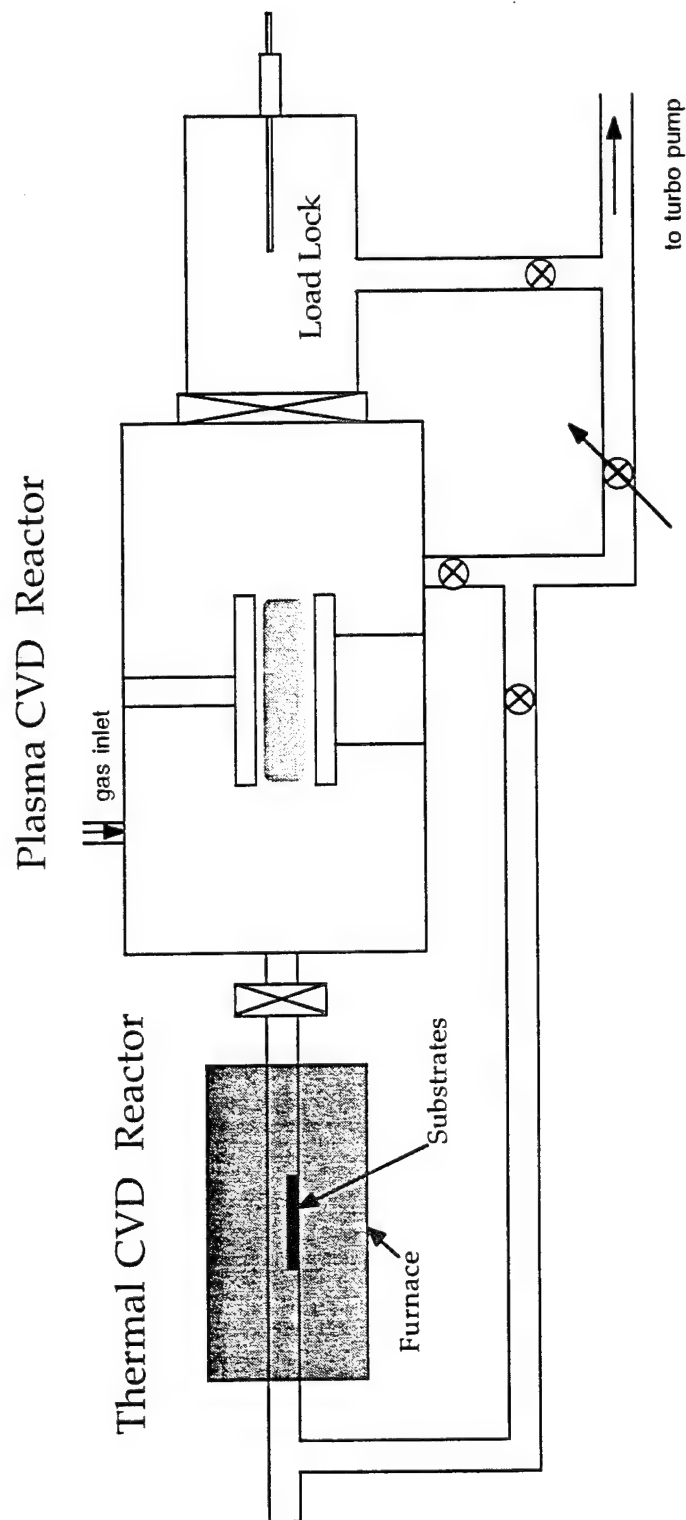
Main Chamber

Plasma CVD Reactor

Thermal CVD Reactor

gas inlet

Load Lock

to turbo pump

Substrates

Furnace

Fig. 3.4 Schematic of lower pressure CVD reactor connected to the plasma enhanced CVD reactor. The two reactors share gas delivery and pumping systems.
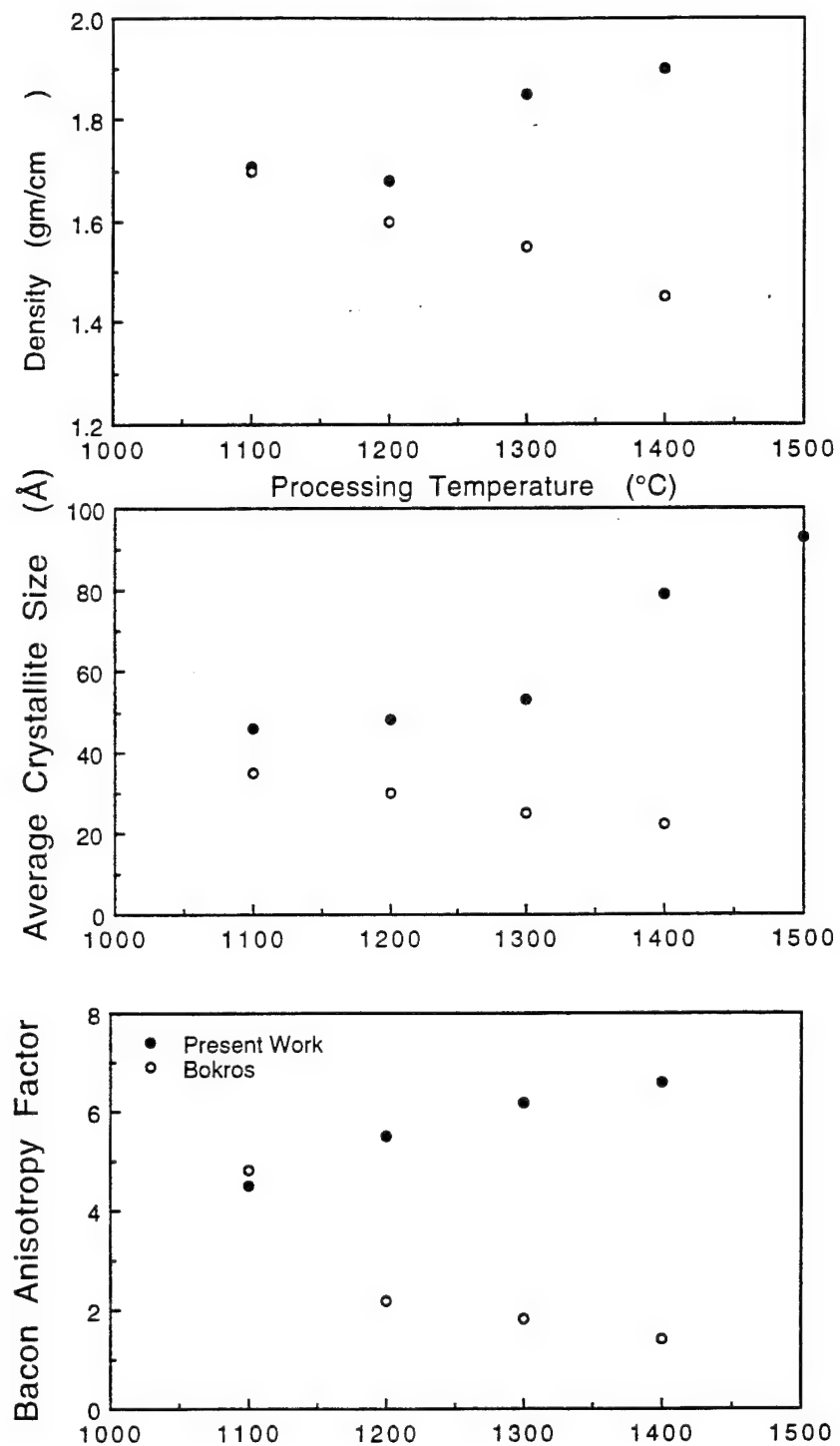
Fig. 3.5 Bacon Anisotropy Factor, average crystallite size, and coating density versus deposition temperature from the present work and also from the review of Bokros [9].
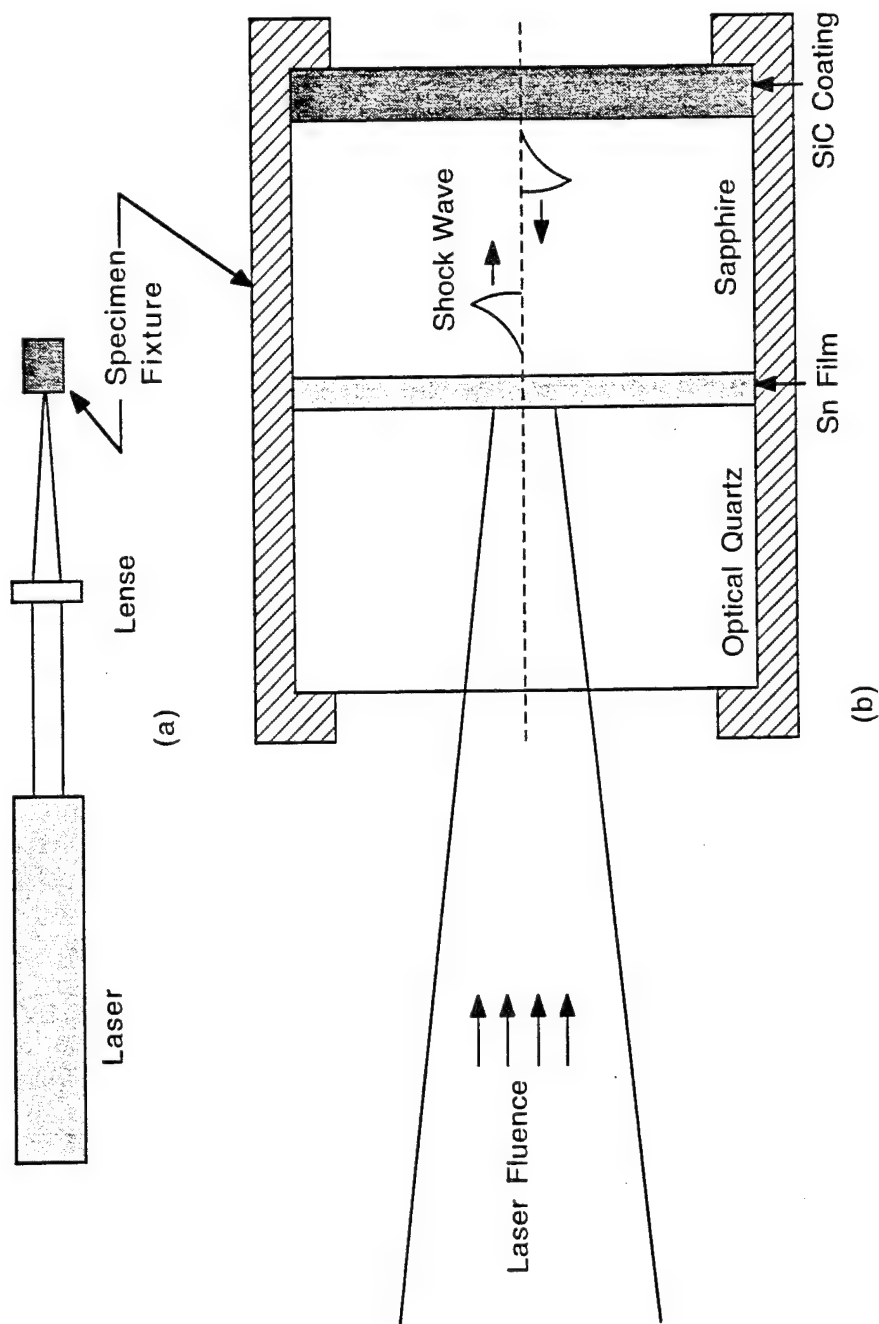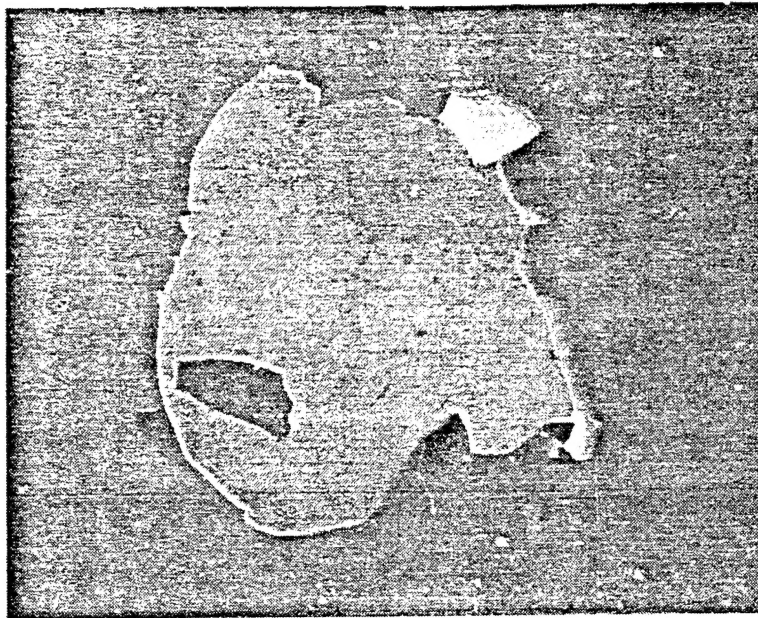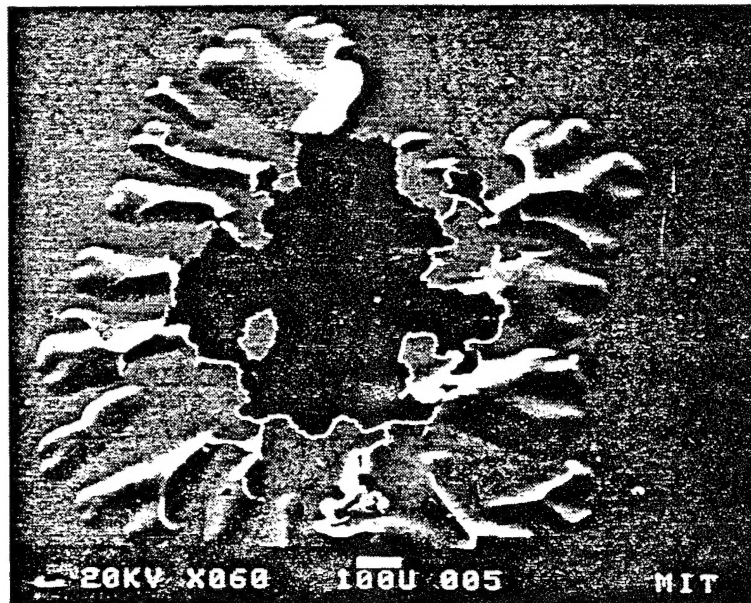
Fig. 3.6 Schematic of experimental set-up of the laser spallation experiment; (a) shows the laser, lens, and specimen on the lab bench, and (b) is an enlargement of the specimen in its holder.

104

(a)

20KV X060   100U 005   MIT

(b)

Fig. 3.7 Photomicrographs of SiC spalled from polished sapphire without and with substantial residual stress in the SiC coating.

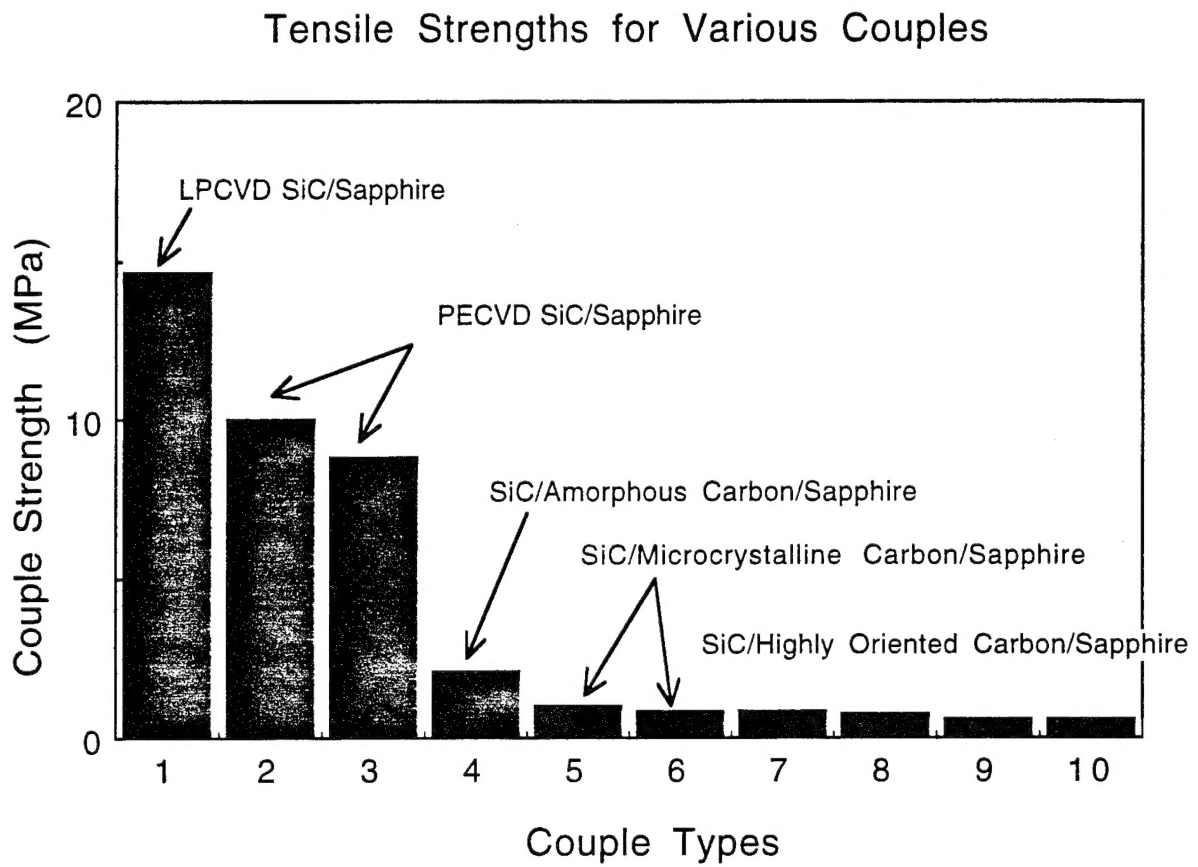Fig. 3.8 Tensile strength for the various couples with and without carbon interlayers.

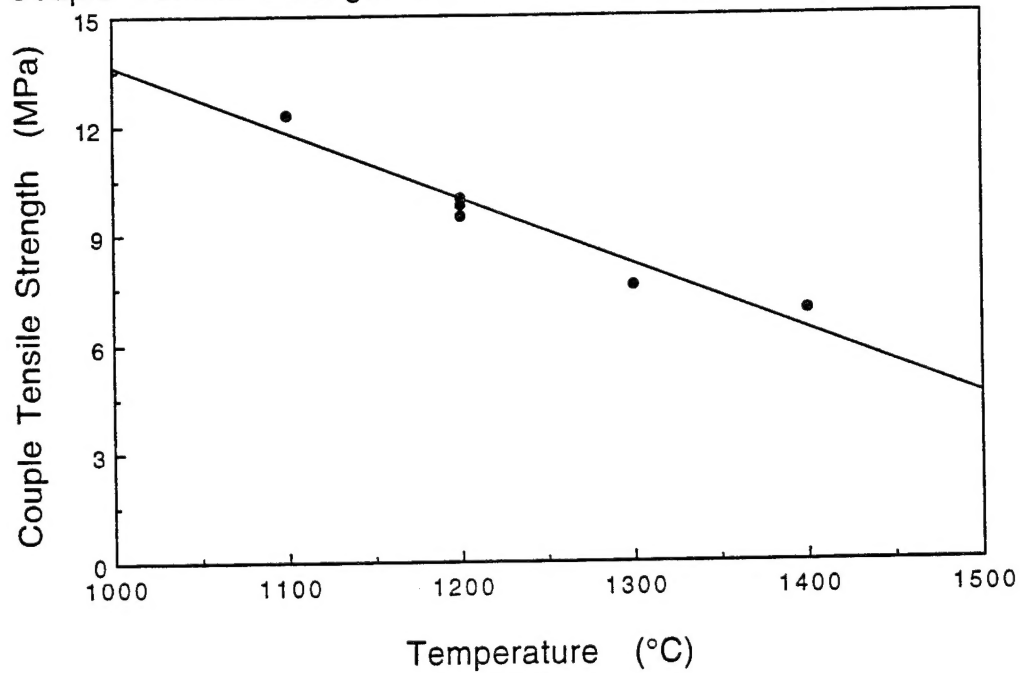Couple Tensile Strength Versus Carbon Processing Temperature

Fig. 3.9 Tensile strength of the model couples versus deposition temperature during processing of the carbon interlayer.
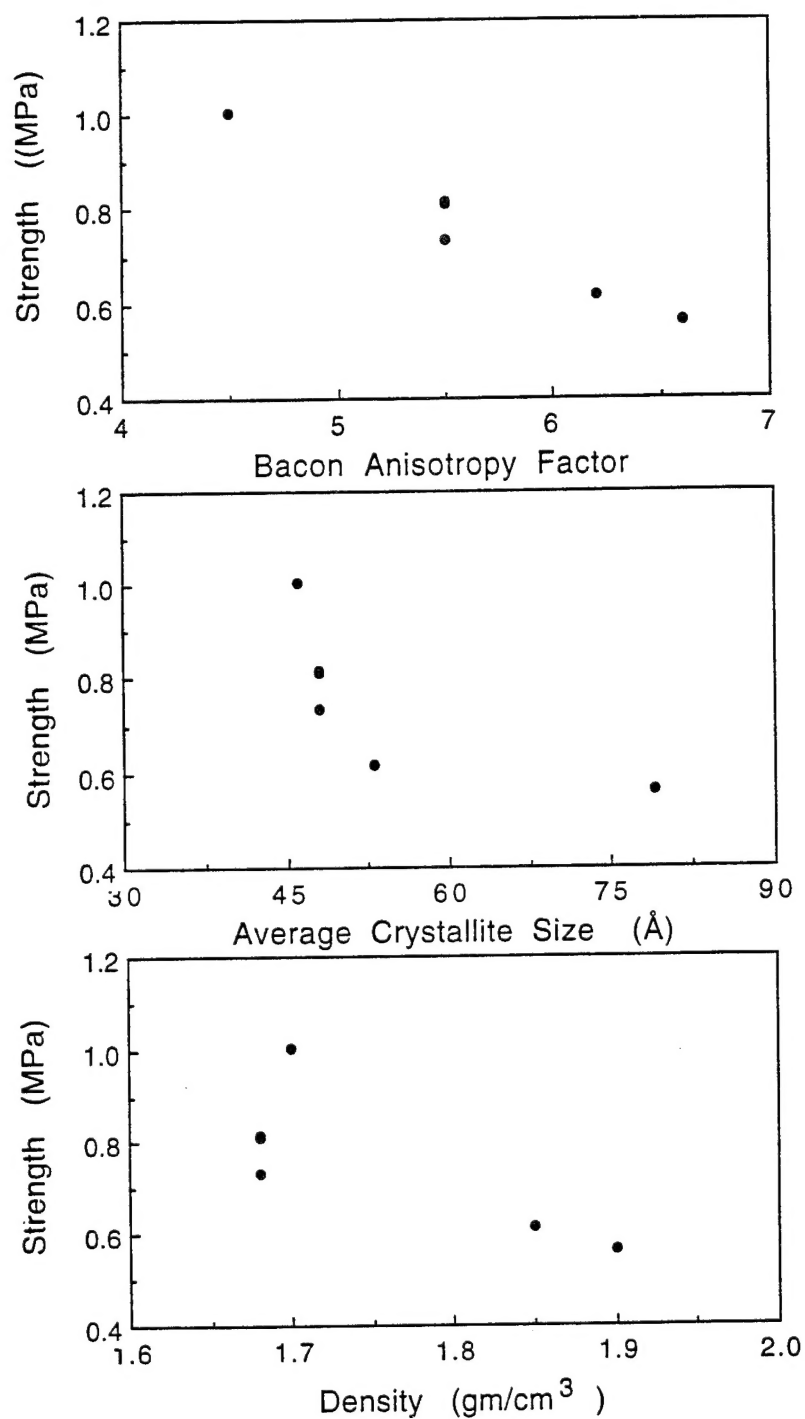
Fig. 3.10 Couple tensile strength versus orientation (BAF), average crystallite size, and density of the LPCVD carbon material deposited on SiC.